Modeling of heat release and emissions from droplet combustion of multi component fuels in compression ignition engines

Ivarsson, Anders; Schramm, Jesper

Publication date:
2010

Document Version
Publisher's PDF, also known as Version of record

Link back to DTU Orbit

Citation (APA):
Ivarsson, A., & Schramm, J. (2010). Modeling of heat release and emissions from droplet combustion of multi component fuels in compression ignition engines. Kgs. Lyngby, Denmark: Technical University of Denmark (DTU).

Modeling of heat release and emissions from droplet combustion of multi component fuels in compression ignition engines

by
Anders Ivarsson

Ph. D. thesis

Department of Mechanical Engineering
Technical University of Denmark
DK-2800 Kgs. Lyngby
Denmark

Kgs. Lyngby 2009

Table of Contents

Summary

This PhD dissertation was carried out at the Technical University of Denmark in Department of Mechanical Engineering and supervised by Associate Professor Jesper Schramm. The PhD project was funded by the Technical University of Denmark.

Demands on reducing the fuel consumption and harmful emissions from the compression ignition engines (CI engines or diesel engines) are continuously increased. To comply with this, better modeling tools for the diesel combustion process are desired from the engine developers.

The complex combustion process of a compression ignition engine may be divided into three separate combustion phases; a pre-mixed homogeneous combustion phase, a non-homogeneous pre-mixed combustion phase and a diffusion controlled combustion phase.

This PhD thesis comprises a study of the non-homogeneous pre-mixed combustion process. Experimental work was performed with a pre-mixed flat flame burner at atmospheric pressure. The fundamental mechanisms of this laboratory flame are identical with those of an IC engine. The high control of the laboratory flame and the easy access to it makes it valuable for model validation. Modeling of the pre-mixed flat flame was performed with computational fluid dynamics (CFD) including combustion chemistry, soot formation and thermal radiation.

First main topic of the project was to deal with the post flame instability, also known as flame flicker, of a premixed flat flame. A nonintrusive method to stabilize the flame, called helium stabilization, was developed. The basis of the method is to ensure almost equal gas densities inside and outside the flame by diluting the surrounding gas with helium. This newly stabilized flame offers some features which are important in combustion research. The flame is very uniform and may be highly lifted, thus it is well suited for optical line of sight diagnostics in both pre and post combustion regions. The work also includes some preliminary studies of radiant emissions from helium stabilized ethylene/air and methane/oxygen flames. It is demonstrated that nano particles below the sooting threshold actually are weakly luminous.

Second main topic of the project was to enable valid temperature measurements of sooting flames. A thermometry method based on IR emission and absorption by CO_2 between 2100 and 2400 cm^{-1} was developed specifically for pre-mixed flat flames. Detection was performed with a commercial FT-IR spectrometer.

An investigation of the method's precision and accuracy was performed separately. The investigation shows that an important strength of the method is its reliability with regard to variations in the experimental setup. Even with non-optimized installation and operation of the method, the average line of sight temperature is determined with a precision of +/- 2 %. With a thorough installation and operation the method detects the temperature of the flame core within +/- 1 %, in spite of the line of sight principle.

Temperature measurements from the literature performed with different thermometry techniques were reproduced and compared. Some of the methods from literature were valid only for a limited range of flame conditions. Thus the consistency of the most established flame thermometry techniques was evaluated, with the IR emission absorption method used as a link.

An optical method was also used to measure the soot content in terms of soot volume fraction. The measurement was based on absorption of light with wavelength between 500 and 520 nm.

The third main topic of the project was to develop a CFD model of a pre-mixed flat flame. The commercial CFD software CFX 11.0 was used. Three cases of ethylene/air flames well known from the experimental work, was used for the model validation. Two cases were helium stabilized flames with φ = 1 and 2.14. The third case was an unstable flame with φ = 2.14. The unstable case was used to test whether a transient model would be able to predict the frequency and shape of the unstable sooting flame. The stable cases were easier to treat both experimentally and numerically, and were used for more detailed validation.

The model was developed stepwise from the simplest possible starting point. The first part of the development was made on a model of thermal fluid flow only. The model was incrementally extended with; temperature dependent thermal conductivity, temperature dependent viscosity, temperature dependent mass diffusion, thermal gas radiation, water gas shift reaction and soot radiation. In the second part combustion was introduced. A simple reaction model well known from the literature did not predict the features of the real flame, thus another simple reaction model was developed specifically for this purpose. A simple soot formation model developed for acetylene diffusion flames was validated against the soot measurements. The model parameters were fitted to predict the measured soot volume fractions in the pre-mixed ethylene flame. The provided results offer insight to the sensitive of the predictions to the model variations.

Resumé (Summary in Danish)

Denne Ph.d. afhandling blev udført på Danmarks Tekniske Universitets Institut for Mekanisk Teknologi med Lektor Jesper Schramm som vejleder. Ph.d. projektet blev finansieret af Danmarks Tekniske Universitets Institut.

Krav til reduktion af brændstofforbrug og skadelige emissioner fra diesel motorer øges konstant. For at leve op til disse krav er der behov for bedre model værktøjer til beskrivelse af Diesel forbrændings processen.

Den komplicerede forbrændingsproces I en Diesel motor kan deles op i tre faser; en homogen forblandet forbrændingsfase, en inhomogen forblandet forbrændingsfase og en diffusions kontrolleret forbrændingsfase.

Denne Ph.d. afhandling indeholder et studie af den inhomogene forbrændingsfase. Eksperimentelt arbejde blev udført med en flad forblandet flamme ved atmosfærisk tryk. De fundamentale mekanismer der foregår i denne laboratorieflamme er identiske med dem der foregår i en Diesel motor. God kontrol over laboratorieflammen og nem adgang til den, gør den værdifuld til model validering. Modellering af flade forblandede flammer blev udført med numerisk fluid dynamik (CFD) med forbrændings kemi, soddannelse og termisk stråling inkluderet.

Det første hovedemne i projektet var at håndtere post flamme ustabilitet af en forblandet flad flamme. En metode uden nogen forstyrrende indtrængning i flammen, kaldet helium stabilisering, blev udviklet. Princippet i metoden er at sikre næsten ens gas densiteter indeni og udenfor flammen ved at fortynde den omgivende gas med helium. Denne nyligt stabiliserede flamme udviser egenskaber som er betydningsfulde i forbrændings forskning. Flammen er meget uniform og et højt flamme løft kan opnås. Dette gør flammen særdeles anvendelig til optisk *line of sight* diagnostik i regioner både før og efter flamme fronten. Arbejdet inkluderer også nogle indledende studier af stråling fra helium stabiliserede ethylen/luft og metan/ilt flammer. De viser at nano partikler af sod er svagt glødende selv under sod grænsen.

Det andet hovedemne i projektet var at muliggøre valide temperaturmålinger af sodende flammer. En termometrisk metode baseret på IR emission og absorption af CO_2 mellem 2100 og 2400 cm^{-1} blev udviklet specifikt til forblandede flade flammer. Detekteringen blev udført med et kommercielt FT-IR spektrometer.

Undersøgelse af metodens præcision og nøjagtighed blev foretaget separat. Undersøgelsen viser at en vigtig styrke ved metoden er dens pålidelighed med hensyn til variation af den eksperimentelle opsætning. Selv uden en optimal installation og betjening af metoden kan den gennemsnitlige *line of sight* temperatur bestemmes til en præcision på +/- 2 %. Med grundig installation og betjening af metoden detekteres temperaturen af flamme kernen indenfor +/- 1 % på trods af *line of sight* princippet.

Temperaturmålinger fra litteraturen der er udført med forskellige termometriske teknikker blev reproduceret og sammenlignet. Nogle af metoderne fra litteraturen var kun gyldige indenfor et afgrænset område af flamme betingelser. Således kunne overensstemmelsen mellem de mest veletablerede termometriske metoder evalueres med IR emission absorptionsmetoden anvendt som forbindelsesled.

En optisk metode blev også anvendt til bestemmelse af flammens sod indhold i form af volumenandel. Målingerne var baseret på absorption af lys med bølgelængde mellem 500 og 520 nm.

Det tredje hovedemne i projektet var udvikling af en CFD model for forblandede flade flammer. Det kommercielle CFD program CFX 11.0 var anvendt til formålet. Tre ethylene/luft flammer der var velkendt fra det eksperimentelle arbejde blev brugt til modelvalidering. To af flammerne var helium stabiliserede med φ = 1 og 2.14. Den tredje var ustabil med φ = 2.14. Den ustabile flamme blev anvendt til at undersøge om en transient model ville være i stand til at forudsige frekvensen og formen af den ustabile soddende flamme. Den stabile flamme var nemmere at behandle både eksperimentelt og numerisk, og blev anvendt til mere detaljeret validering.

Modellen blev udviklet trinvis fra det simplest mulige udgangspunkt. Den første del af udviklingen blev foretaget på en model kun bestående af den termiske fluidstrøm. Modellen blev trinvis udvidet til at indeholde; temperaturafhængig varme ledning, temperaturafhængig viskositet, temperaturafhængig massediffusion, termisk stråling fra gas, vandgas reaktion og termisk stråling fra sod. I anden del af modeludviklingen blev forbrændings reaktioner inkluderet. En simpel reaktionsmodel velkendt fra litteraturen kunne ikke forudsige flammens egenskaber, så en anden simple reaktionsmodel blev udviklet specifikt til formålet. En simpel sooddannelses model udviklet til acetylen diffusionsflammer valideret med sodmålinger. Modelparametrene blev tilpasset så modellen kunne forudsige de målte sodvolumenandele i den forblandede ethylen flamme. De frembragte resultater yder indsigt i forudsigelsernes følsomhed overfor modelvariationer.

Introduction

In basic research projects, it is often not clear exactly what the focus of the investigation will be at the time the project was formulated. When new steps are taken to explore a topic of research it is also difficult to predict the challenges that will be met. When dealing with a topic of research that have been practiced for almost a century, it may be necessary not to walk into others footsteps to access new information and discoveries, regardless of the consequences it may have to the actual project.

This introduction serves to guide the reader through the decisions that shaped this project.

The general aim of this project

The major part of the world transportation is powered by Compression Ignition (CI) Engines. Particularly if it is not measured in terms of transportation units but in terms of energy consumed, CI engines are dominating spark ignition (SI) engines. This is due to the large units in the ship transport sector. The CI engine in general but particularly the marine diesel engine is one of the most efficient power machines and relatively cheap fuels may be used for it. In the cleaner alternatives are still not developed enough and are too expensive to take over the CI engine for the next many years.

Thus with tightened emission regulations the demand for improving the CI engines is continuously increased.

The main concern with the CI engine is the emission of soot and NO_X, which are harmful to the human being and the local environment. But with the forecast of higher oil prices and penalties for CO_2 emission, the efficiency persists to be a concern for engine manufacturers.

Ever since the invention if the CI engine but particularly the last decades, great improvements have been made to it. Most of these improvements are attributed to small incremental changes to the engine design based on costly and time consuming experiments.

Therefore the demand for modeling tools to investigate the potential of design changes before trying them in reality is large. In many technical universities and companies around the globe, great efforts are put into the development of these tools. But particularly the combustion processes in a CI engine are complex and basic understanding needs to be resolved to develop valid models.

The general aim with this project is to achieve a better understanding of the basic underlying processes in the IC engine combustion, which may contribute to the development of the needed modeling tools.

Combustion processes in the compression ignition engine

During the pre investigation phase of the project, the work by Dec and Flynn [1] was found to be the most trusted conceptual illustration of the stepwise CI engine combustion process.

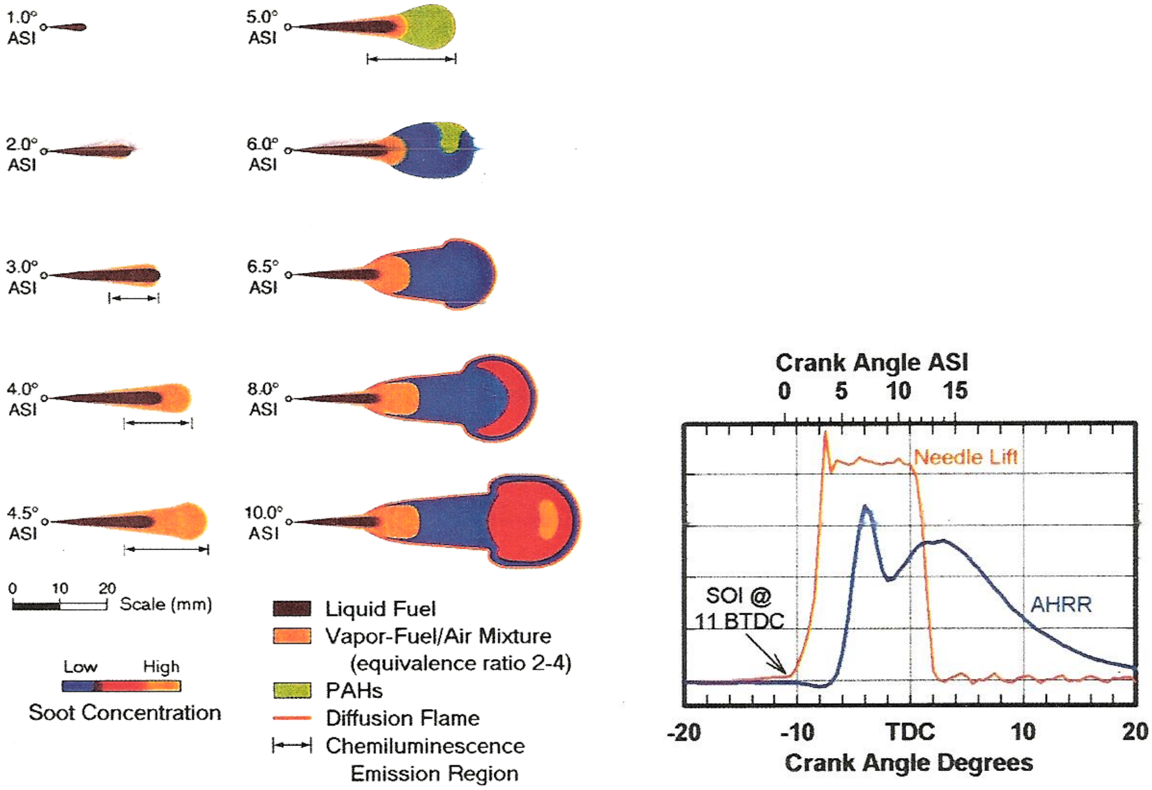

Figure 1: Schematics of early flame images from laser measurements by Dec and Flynn [1]. AHHR means apparent heat release rate, ASI means after start of injection, SOI means start of injection and BTDC means before top dead center.

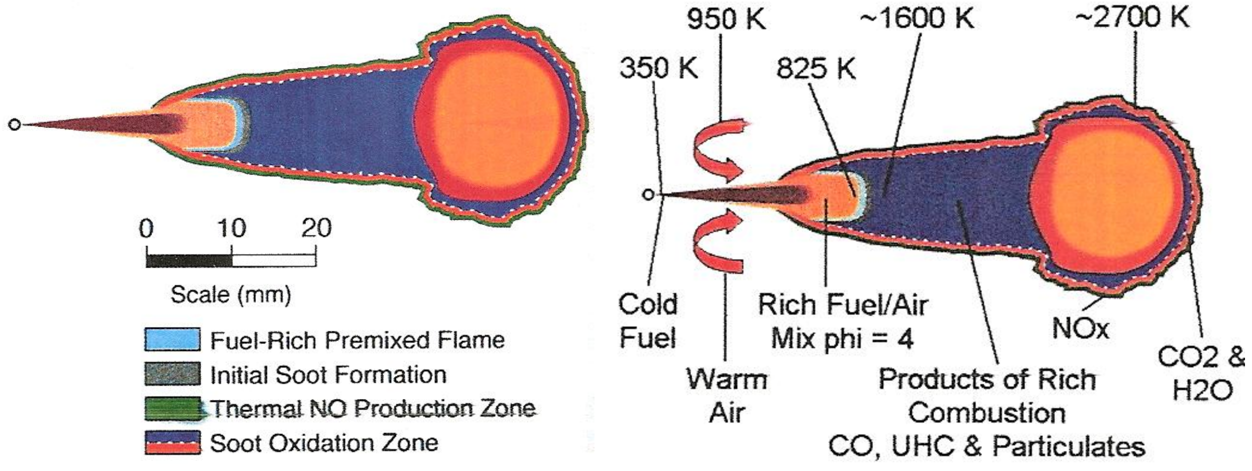

Figure 2: Schematic of quasi steady burning fuel jet from laser measurements by Dec and Flynn [1].

This was due to the large number of measurements in an optical engine which it was based upon.

The illustrations in Figure 1 show the transient steps during the development of a quasi steady burning fuel jet in Figure 2. The reason for using the term quasi is that the burning fuel jet changes size but the general features are preserved.

In words the combustion sequence may be described as follows:

1. The first 5 crank angle degrees after the injection start, the liquid jet breaks up, evaporates and mixes with air.
2. A pocket of rich premixed fuel vapor and air is build up at the end of the jet.
3. Around 5 degrees after the injection start the fuel in the premixed pocket decomposes.
4. Around 6 degrees the decomposed fuel and air ignites. The homogeneous combustion of the pocket is the reason for the rapid increase of the heat release rate.
5. The heat released by the homogeneous combustion ignites two succeeding combustion processes:
    - A diffusion flame surrounding the pocket of excess fuel, cracked fuel and soot from the rich homogeneous combustion.
    - A rich premixed flame formed inside the pocket, on the interface between incoming rich premixed fuel vapors and air, and the hot combustion products (Figure 2). The combustion products from the premixed flame contain sufficient excess fuel, cracked fuel and soot to feed the diffusion flame.

   From the area under the heat release curve it is evident that the major part of the heat is released in this step.

6. The premixed flame persists as long fuel is injected, then the pocket will be closed and burn up by the diffusion flame.

Soot is formed inside the gas pocket, first as product from the homogeneous combustion and then from the premixed combustion. The diffusion flame heats up the inside gas and more soot is formed.

NO_X is formed just outside the diffusion flame where temperatures are high and oxygen is present, and in the diffusion flame some of the soot is oxidized. This is the reason for the NO_X vs. soot conflict [2]. If the temperature in the diffusion flame is increased, more NO_X but less soot will be emitted from the engine, and opposite if the temperature is decreased.

These illustrations of the CI engine combustion shows that it actually consists of three different combustion processes. On top of this the cylinder flow is swirling and is highly turbulent, which strongly influences the heat and mass transfer. Thermal radiation plays an important role in the heat transfer too. Thus the total combustion process in a CI engine is really complex.

If a future CI engine model should be able to predict the effect of small design changes like the number of nozzle holes, the injection direction or the fuel composition etc., then there is no good alternative to a full 3D CFD package with transient, two phase flow, turbulence model, radiation model and reaction kinetics.

Several commercial and open source CFD software packages are able to cope with these demands and offer a wide choice of models for the individual processes. The challenge is to choose the right models and model parameters suited for the conditions in the CI engine. To overcome this, it is necessary to break the CI engine processes into pieces and validate them separately with simpler experiments at conditions as close as possible to those in the engine. For example a turbulence model may be validated against measurements of air flow in a cylinder like geometry without any fuel injection and combustion. Or a spray model may be validated against measurements of sprays in a closed vessel with still gas, without combustion.

The focus of this project

During the pre-investigation for this project it was found that most attention in the research has been paid to the swirl inside an engine, the spray evaporation and the diffusion flame, while the premixed flame and the soot formation inside the flame pocket was less investigated.

The pre-mixed flame is important for entire combustion process in CI engines because it links the evaporation process of the fuel spray and the diffusion flame:

The product gas of the pre-mixed flame is the fuel for the diffusion flame. The flame temperature of the pre-mixed flame will influence the temperature of the diffusion flame via the temperature of the intermediate fuel. The flame temperature of the pre-mixed flame will also influence the decomposition of the intermediate fuel to soot and H_2.

The location of the premixed flame is determined by the burning velocity balanced against the premixed jet velocity. The burning velocity depends on the vaporized fuel composition, the equivalence ratio and the flame temperature. The flame temperature is determined by the heat release balanced against heat transfer to the spray evaporation.

The focus of this project is to get a better understanding of rich premixed flames and their soot formation, and to validate simple models that may be applicable in large transient 3D CFD models.

The choice of investigation case

Intentionally this work was supposed to be purely theoretical. The model development should be validated against experimental results available in the literature. The main reason for that was that no experimental facilities suitable for investigating the reaction kinetics and soot formation in flames were available.

But in the literature study it became evident that this would not be a successful approach. Numerous experimental investigations about reaction kinetics and soot formation in flames were found. But usually they focused on one thing and did not provide the complete picture of all the processes that was going on. For some reason the different investigations were often made at different flame conditions so that the individual results could not be combined to build the complete picture. In the rare cases where identical conditions were used the results did not agree. This was particularly the case for measurements of flame temperatures. On the other hand many theoretical investigations were found. The general impression of these investigations was that they were scarcely validated against experimental results. Usually theoretical models were validated against other theoretical models and often with poor agreement. Thus if the present work also should be purely theoretical, there would be a big risk that it would just bring yet another model nobody would use because it was not well validated.

Furthermore it was felt that practical work with the real flames was needed to develop an intuition and a deeper understanding of how they behave and respond on different variations.

Thus it was decided to turn the project into an experimental project and to try to get as far as possible with a model. Consequently the experimental facility should be build from scratch. The bad thing about that was of cause that it would be time consuming, costly, and that many unexpected challenges would show up. The good thing about it was the freedom to choose the right experimental setup for this purpose.

The first choice that had to be made was to determine what kind of flame or reactor system that would be best suited for validating combustion and soot models for compression ignition engines. Some of the most important criteria's for that was as follows:

1. It should be possible to model the flame or reactor system in one dimension because this would enable the use of full chemistry models in effective modeling tools like Chemkin.
2. The flow should be laminar to simplify the modeling.

3. The flame or reactor system should enable good access for various measurement techniques. This implies one dimensionality, steadiness and a large size of the reaction domain with low spatial reaction gradients.
4. The thermodynamic condition of the flame or reactor system should be as close as possible to those in a compression ignition engine.

Most flame experiments in the literature are made with diffusion flames. This is because most flames used in real applications are diffusion flames. A disadvantage of experiments with diffusion flames is that it is very difficult to produce a flame that may be modeled as one dimensional. Furthermore measurements on the fuel rich side of the flame are difficult because it often is enclosed by the hot diffusion flame.

Experiments with plug flow reactors have really nice properties of being one dimensional, good temperature control is enabled, and with proper adjustment of the setup the reactions may be stretched to enable a good resolution of gas composition measurements. The work by Skjøth [3] is an excellent example of investigating soot formation with a laboratory plug flow reactor. A disadvantage of experiments with plug flow reactors is that an upper limit for temperatures is determined by the materials of the reactor wall. Typically temperatures higher than 1300 K are not achievable. It is also discussed to what extend the reactivity of the walls may influence the reactions. Furthermore the plug flow reactor offers no optical access to the reaction zone.

Inspired by experiments with plug flow reactors a solution was sought that was similar to a plug flow reactor but without reactor walls. It was believed that a flat flame burner (Figure 3) could make this possible if it was used in an untraditional way. The idea was to have the burner located in a long chamber flushed with N_2 to omit soot oxidation. The outer porous disk (Figure 3) could then be used as a burner for a shielding flame to thermally shield the inner flame. This setup was believed to make up a quasi one dimensional plug flow reactor without intrusive and temperature limiting walls.

With this arrangement it will be possible to establish rich premixed flame almost like the one inside the diesel flame (Figure 2). If a high pressure chamber was made it would even be possible to simulate the pressure in the engine. A setup like that has been made by Böhm [35], and their results show that soot formation increases linearly with the pressure. In this work a chamber was made for atmospheric pressure only.

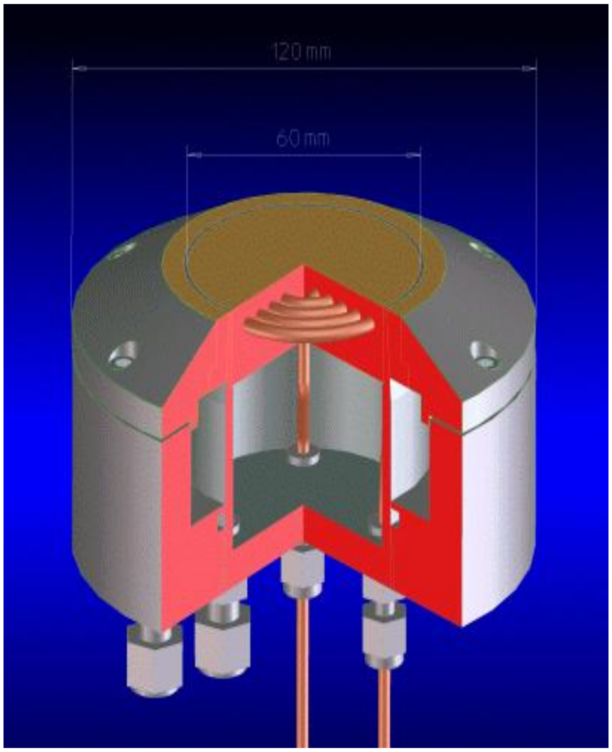

Figure 3. Illustration of a standard McKenna flat flame burner. The bronze colored outlets are made of sintered bronze with a cobber spiral inside for water cooling. The pressure drop over the porous outlet combined with water cooling ensures a uniform velocity distribution of the reactant gases at known temperature. The outer disc of sintered bronze is for co flow of inert gas to protect the flame from oxygen entrainment.

A flat flame burner of this kind is not suited for liquid fuels, thus real diesel cannot be used. But Figure 2 shows that the temperature of the rich fuel and air mixture is about 825 K when it arrives to the premixed flame front, thus the diesel is not necessarily diesel anymore. The long chained alkanes are unstable at these temperatures and will be cracked to lighter hydrocarbons. It is believed that the mixture of these lighter hydrocarbons could be made and used in the flat flame burner. Determination of the composition should be made in a separate experiment with a plug flow reactor i.e. In this work ethylene C_2H_4 is used as a simple substitution to the cracked diesel. It is believed to be a proper choice because the C/H ratio of 0.5 is close to the ratio for diesel (C/H = 0.54). Other fuels like heavy fuel oil (C/H = 0.6) and rape seed oil (C/H = 0.55) have almost the same C/H ratio. Exactly the same C/H ratio as the liquid fuel could be obtained by mixing acethylene C_2H_2 (C/H = 1) with ethylene to the right ratio. Soot inception experiments with various fuels show that the sooting propensity is more dependent on the C/H ratio than on the molecular structure. The sum of these arguments qualifies the premixed burner experiment as a good approximation of the premixed flame inside the diesel flame of a CI engine.

Establishment of a stable premixed flat flame

A premixed flame with the flame front stabilized on a flat flame burner has a unique property compared to other laboratory flames in that it is stationary and close to being one-dimensional (1D) or quasi-1D. This means that the distribution of temperature, velocity and chemical composition within the flame is nearly uniform perpendicular to the flow direction.

This quasi-1D property is a big advantage in combustion research because it enables the use of many measuring techniques which can’t cope with the demands of high spatial resolution in axisymmetrical 2D flames and/or the high temporal resolution in homogeneous combustion. Furthermore, the quasi-1D flame is much easier to treat numerically than axisymmetrical 2D flames. This makes it very useful for validation of combustion models.

Particularly in investigation of soot formation, growth and agglomeration, the larger number of applicable measuring techniques with this flame is of high importance. Due to the size of the soot particles, they scatter and absorb visible light and make it difficult to use the well established laser methods with their high spatial and temporal resolution [4]. The use of thermocouples in sooting flames is also difficult due to soot deposits building up on the solder joint. This makes it difficult to account for the radiative loss [5].

Unfortunately, the stationary and quasi-1D condition of a premixed flat flame is difficult to obtain. Even though the flame front is easily stabilized above the burner disc the combustion products usually take the shape of ripples moving along the flow. A premixed flat flame with fuel/air ratio at 1 or less will seem very stable, but close observation of CH bands above the flame front or Schlieren photography reveal the instability [6, 7]. With a rich, sooting flame the instability becomes very apparent [Movie1.avi].

The usual way to cope with this instability is to insert a thick metal plate, a so called stabilizer plate, about 20 mm above the burner disc [8, 9, 10, 11]. For some reason the flame is stabilized but the intrusion to the flame causes information about further downstream soot growth and agglomeration to become lost. Nor is the flame quasi-1D anymore.

This work deals with the understanding of the post flame instability of premixed flat flames and reveals a method for stabilizing the flame which, to the authors’ knowledge, has never been used before.

Instability of flames

In the physics of flames there are many different stability issues. The most common is the stabilization of the flame front. On the flat flame burner the flame front is stabilized above the porous disk by heat transfer to the disk and thereby the burning velocity adjusts itself to be the same as the gas velocity.

The instability dealt with in this work is the instability occurring in the combustion products downstream the stabilized of flame front. This is also called flame flicker and is best known from a burning candle. If the candle wick becomes too long, the flame often begins to flicker in a very systematic oscillating way.

Most studies of flame instability have been done with diffusion flames. In some of the earliest studies [8, 12, 13, 14, 15] it was observed that the oscillation frequency was insensitive to the size of the chamber surrounding the flame and the length of the gas tubes leading to the burner. This eliminates the possibility that the oscillation is driven by some sort of standing wave determined by geometries. The oscillation frequency is also relatively insensitive to changes in flow rate, burner size, type of fuel and fuel/air equivalence ratio. Experiments with porous hemispheres fed with ethanol (liquid) or propane (gaseous) to simulate a candle show identical instability behavior. This eliminates the possibility that the instability has its origin in the coupling between heat and mass transfer. Stability analysis with perturbation methods have been used on simplified analytical 2D parallel flows without combustion. They predict the instability and the oscillation frequencies reasonably close to experimental observations in spite of all the simplifications. This is supports the theory that this instability phenomena solely is caused by fluid dynamics and not the combustion process.

In more recent studies of diffusion flame instability [16, 17, 18, 19, 20, 21, 22, 23, 24] improvements have been made in visualization techniques in experiments, and detailed numerical models have been developed. A visualization technique based on reactive Mie scattering has yielded some high quality pictures showing that also inside the flame there is a vortex train due to shear layer instability. Numerical models reproduce the instability well if the heat release is reduced by 20 %. The necessity of heat release reduction is due to radiative losses which are not accounted for in the numerical models. Transient modeling with no gravitation produces a stable flame, which is also validated with parabolic flights.

Extensive studies of partially premixed flames have been performed both experimentally and by numerical simulation [25, 26, 27]. Two categories of partially premixed flames established on a Wolfhard-Parker burner were investigated: 1) A “double flame” with a fuel rich premixed flame surrounded by a non-premixed flame and 2) a “triple flame” with a fuel rich premixed flame surrounded by a fuel lean premixed flame and a non premixed flame in between. Experiments were performed in a 2.2 s drop tower to investigate the gravitational influence on the flame stability and shape. Experiments show that the “triple flame” is more prone to buoyancy induced instability than the “double flame” even though it is independent of oxygen supply from the surrounding air. Two types of instabilities were observed for the “triple flame”. At 1 g (normal gravity) and with a flow from the lean burner below a certain level, instability developed at the same height as the flame. This instability is believed to be buoyancy induced, since it disappeared when gravity was reduced to zero. But at 0 g (no gravity) when the flow from the lean burner was above a certain level, an instability developed at the flame tip. This is believed to be a shear induced instability.

Only few stability studies of premixed flames have been performed [6, 7, 28]. With Schlieren photography it has been shown that lean premixed flames are unstable at 1g but stable at 0 g. The experiments were performed in a 2.2 s drop tower.

In these investigations there is a consensus that the outer vortex structures causing the low frequency flame instability are induced by buoyancy driven shear layer instability of the Kelvin-Helmholtz type. Similar conclusions have been drawn in the research of rising plumes [29, 30]. An interesting analogy study between these two research topics has been made by Yuan *et al.* [31]. Experimentally, he simulated the gravitational effect on a flame with a rising helium jet surrounded by air, both at ambient temperature. The observed instabilities are very similar to those with flames.

Different attempts have been made to stabilize a flame at 1g in order to investigate soot formation and growth mechanisms. A commonly used method for premixed flat flame burners is to place a thick stainless steel plate with the same diameter as the burner 20 – 40 mm above the burner [8, 9, 10, 11]. This forces the flame to flow around the stabilizer plate and stabilizes the flame between the burner and the stabilizer plate. Variants of this method have been used where a hole in the stabilizer plate allow a soot column to pass through the stabilizer plate without too much intrusion [32]. Also, a stainless steel grid with a 45 mm hole has been used as replacement for the solid plate [33]. Stable flames have also been established within a glass or ceramic tube with wire grids on the top [34, 35]. To reduce heat loss and soot deposition to the tube from the object flame, a non sooting flame shielded the object flame from the tube wall. For diffusion flames on a rectangular Wolfhard-Parker burner, stabilization has been established with screens shaped like the flame in order to avoid vortex buildup [36, 37].

Experimental setup

The flat flame burner used in this work is the widely described [35, 36] standard bronze Holthuis & Associates burner also known as a McKenna burner. The outer ring of the burner is normally used to create an N_2 co-flow around the flame. In this work it has shown to be more useful to use it as an outer burner with a stoichiometric hydrogen flame to thermally isolate and improve the uniformity of the center flame. To enable a co-flow of inert gas around the two flames, a homemade outer ring of quartz filter kept in place by a perforated steel sheet has been added to the standard burner (Figure 4). The quartz filter, which was originally made for aerosol sampling purposes, causes a pressure drop large enough to ensure a uniform flow out of the ring.

Figure 4. Top view of the standard bronze Holthuis & Associates burner surrounded by a homemade co flow screen.

The burner is located in a steel chamber with W/L/H = 200/200/800 mm (Figure 5).The door to the inside of the chamber is made of temperature resistant ceramic glass. The burner is mounted on an arrangement that enables traversing it up and down inside the chamber. At the highest location there is a distance of 500 mm above the burner to the roof of the chamber. The combustion products are exhausted through a cone, followed by an iris valve seen at the top of the burner in Figure 5. The iris valve is adjusted to ensure there is no reverse flow entering the burner chamber. The rest of the chamber must be absolutely sealed as the slightest leakage will make the flame unstable. This makes the flame insensitive to variations of room pressure and air movements caused by the laboratory ventilation system etc. Furthermore, helium consumption is reduced to a minimum when it is used as coflow.

Figure 5. View of the experimental setup. The flame chamber is aligned with a Nicolet 6700 FT-IR (left) and a black body (right) to investigate radiation and absorption of the flame. A Hovagas G6 gasmixer (bottom) is used control the gas flows to the burner.

The gas flows led to the burners and the co-flow ring are controlled with a Hovagas G6 gas mixer. It is equipped with two 0.25-5 standard liters pr. minute (SLM), two 0.5-10 SLM, one 1.5-30 SLM and one 3-60 SLM channels, referring to SLM of air. The mixer is calibrated with air to control the channels within +/- 1 % of the reading. The flow is converted for other gases than air with standard flow conversion factors used for mass flow controllers.

The fuel gasses used for this work are methane and ethylene both certified to 99.5 % purity. The compressed air is dried to a dew point of 3 ˚C. The helium is standard balloon helium.

The camera used for all the pictures including high speed pictures is a Casio EX-F1 mounted with a B+W #468 UV-IR filter. For all still photos the following camera settings were used: ISO 100, dynamic range = +2, white balance = daylight fluorescence, aperture = 2.9. In each case the exposure time was set just short enough to avoid saturation. For the high speed captures the frame rate was set to 1200 frames per second (fps) and all other settings were automatic. No editing of the photos has been performed except for the high speed captures were averaging of several pictures has been used to remove noise.

To determine the flame oscillation frequency, a Matlab code was made to load and analyze the JPEG files from the high speed captures. The procedure used is to choose a picture at a reference time and compare it with pictures at all others times to see how identical they are. As a measure of how identical they are, the root mean square (RMS) deviation (DEV) of the red, green and blue (RGB) data is used, as defined in equation 7.

$$DEV(t) = \frac{1}{I\,J\,K}\left(\sum_{i=1}^{I}\sum_{j=1}^{J}\sum_{k=1}^{K}\left(RGB(t_{ref})_{i,j,k} - RGB(t)_{i,j,k}\right)^2\right)^{\frac{1}{2}} \qquad 1$$

The time history vector of the RMS deviations is multiplied with a Hamming window and a fast Fourier transform (FFT) is performed. These are standard components in Matlab. The FFT is made with sufficient trailing zeros to get about 0.01 Hz resolution in frequency spectrum. The frequency at maximum amplitude is found for frequencies higher than 1 Hz and is considered to be the flame oscillation frequency. The procedure is repeated for different choices of reference pictures (typically every 100) and the standard deviation of the found frequencies is calculated. This is done to make sure that the reference pictures are representative and that the captured flame oscillation is systematic. Usually the standard deviation is within the accuracy of the FFT resolution.

Analysis of flame instability

Previously reported flame oscillation frequencies of premixed flames are limited to burners with a relatively small diameter (d < 26 mm). In this work the instability of a rich premixed ethylene flame on the d = 60 mm flat flame burner has been analyzed. The burner was supplied with 20 SLM of air, 3 SLM of C2H4 (ϕ = 2.14) to the center burner and no co-flow or shielding flame was used. In Figure 6 pictures of a flame oscillation period are shown.

The flame oscillation was found to be very systematic and reproducible. The top series in Figure 6 is captured with 1200 fps. Only the most luminous part of the flame is visible on the high speed captures due to the short exposure time, and the random noise is pronounced due to high signal gain. But due to the high reproducibility of the oscillation, pictures at the same time in the oscillation period could be averaged to remove noise completely without losing too much sharpness. Each high speed capture presented in the top series of Figure 6 is actually an average of 17 pictures, but the average represents the 17 individual pictures well, just without the noise. The bottom series in Figure 6 is captured with 60 fps. With frame speeds at and below 60 fps the camera is able to capture a burst of 60 pictures with 6 mega pixel resolution and a higher degree of freedom to the settings of the camera. The bottom series in Figure 6 is captured with the same basic settings as the still pictures except for the ISO value of 1600. With this ISO setting the sensibility of the camera is just sufficient to fully use the dynamic range of the camera at a 1/640 s exposure time, which is fast enough to get unblurred snap shots. The bottom series in Figure 6 shows true snap shots and no averaging is performed.

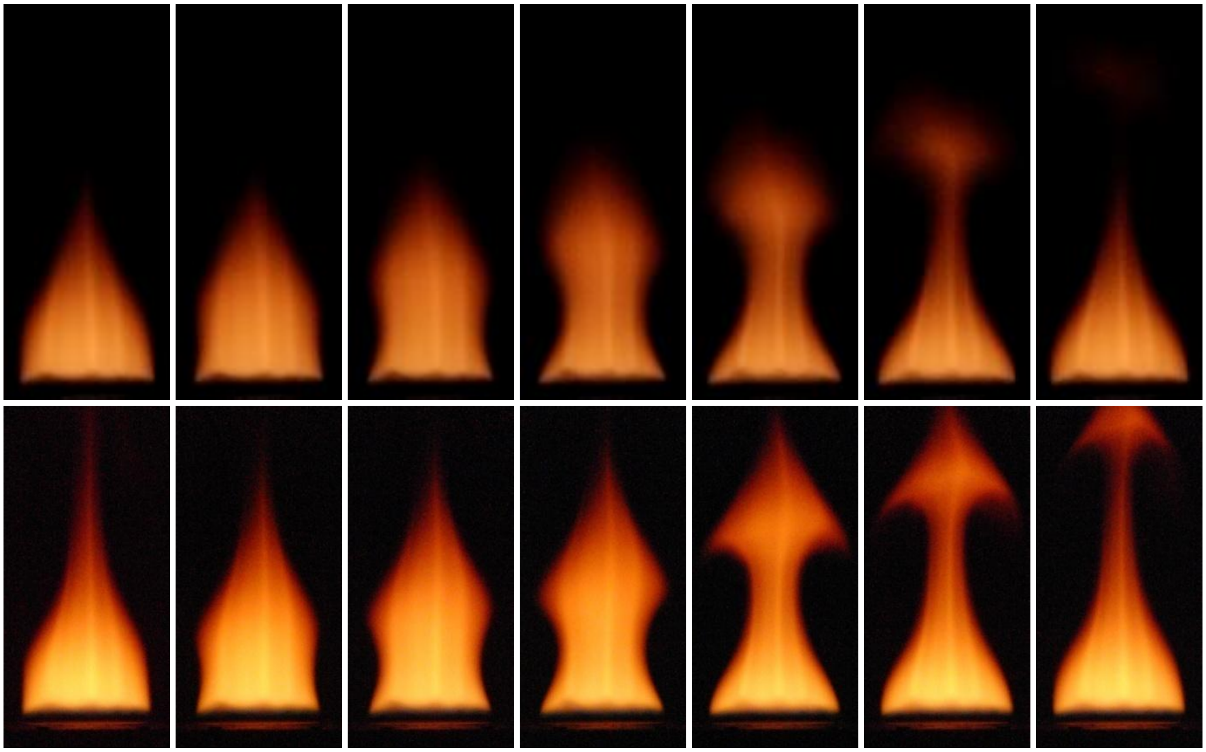

Figure 6. High Speed captures of one oscillation period of the flame instability. The time duration between each frame is 20.1 ms. The top series is captured with 1200 fps to get highest possible accuracy in the frequency analysis. The bottom series is captured with 60 fps and a shutter speed of 1/640 s to improve colors and details of the flame structure.

In Figure 7 a time history plot of the RMS deviations during 2.5 s is shown and the frequency spectrum is shown in Figure 8. The flame oscillation frequency is found to be 6.98 Hz, which is nearly the half of previous findings. Kostiuk found the frequency to vary within 10-16 Hz dependent on the flow conditions [6, 7]. The reason for this is believed to be the large difference in burner diameters. Experiments with diffusion flames on tube burners ranging from d = 4 to d = 15 mm show that frequency is proportional to -0.2d [40]. If this is used to extrapolate 13 Hz at d = 25 mm (typical findings from Kostiuk [6, 7]) to 60 mm a frequency of 6 Hz found which is slightly lower than the measured value. Also the difference in heat transfer to the water cooled porous burner used here and the burner with glass beads used by Kostiuk [6, 7] may influence the oscillation frequency.

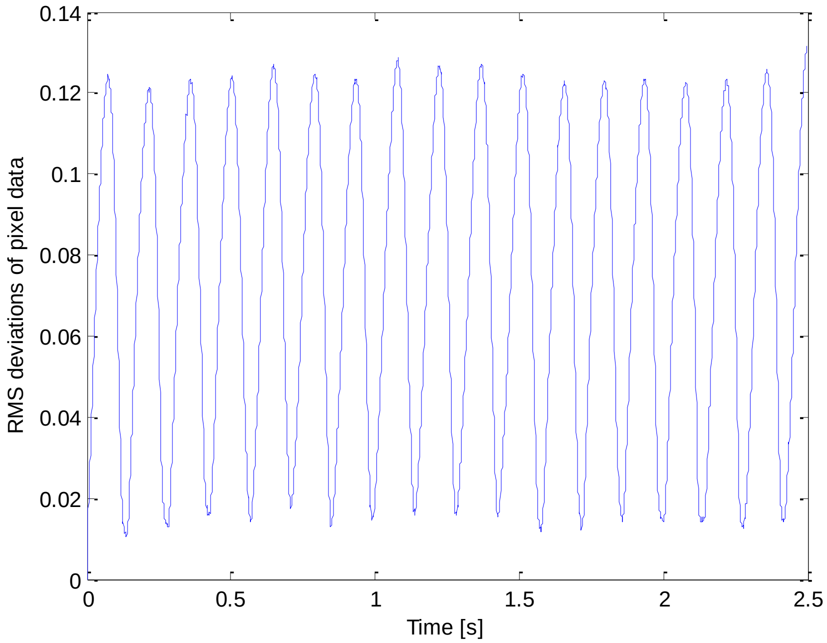

Figure 7. A time history plot of the RMS deviations between RGB data at t = 0 and RGB data at all other times.

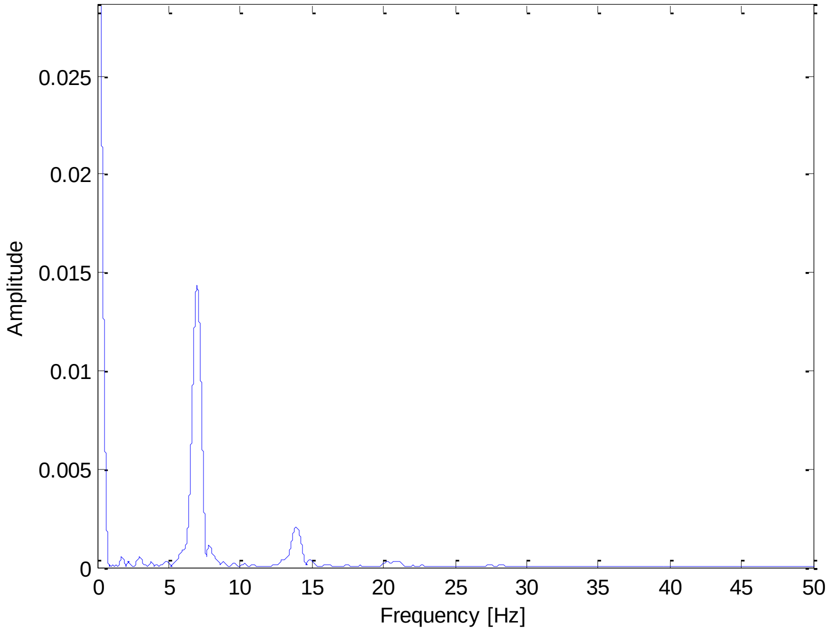

Figure 8. Frequency spectrum of the time history data used in Figure 7.

Flame stabilization

In this work a method has been developed to stabilize a premixed flat flame. It is a general perception that the instability is buoyancy driven. An experimentally proved method to stabilize the flame is to remove gravity, which is not a very practical solution. But the same effect should be achievable by reducing the density difference between the flame products and the surrounding gas. This was tried in this experiment by creating a co-flow of helium around the flame and it worked very well. The density of Helium ($\rho = 0.16$ kg/m^3 at $T = 300$ K) is nearly the same as the density of the hot combustion products from typical flames, while the density of nitrogen is more than 7 times higher. Thus the buoyancy effects are minimized in spite of the presence of gravity.

In order to make this a practical solution, it was necessary to reduce the helium consumption by proper design of the flame chamber and exhaust outlet. With the final camber design, stability was obtained with a helium flow of 30 SLM in most cases. The helium enters through the homemade co-flow arrangement, but doesn't act as a co-flow due to the low velocity. It just continuously dilutes the gases surrounding the flame. A movie [Movie2.avi] shows the unstable flame becoming stabilized by turning on the co-flow of helium halfway through the movie. In the movie some random flicker persists after the helium flow has been turned on, but after some minutes when all temperatures and gas concentrations have stabilized the flame become completely stable.

The helium stabilization has been achieved on many different flames without any adjustments. But in case of very rich flames it may be necessary with a H2/air shielding flame for best stability and uniformity. At high flow rates of the premixed fuel gas it may be necessary to increase the co-flow of helium to about 60 SLM.

When helium stabilization is used, the only stability issues that seem to be left are related to the stabilization of the flame front above the burner disk. Some interesting stability issues have been observed with premixed methane flames, which are not related to buoyancy induced shear layer instability. A rich methane/air flame blows off due to the low burning velocity but a rich methane/oxygen flame is easily stabilized. At lean conditions and low flow rates the methane/air flame generates a pure acoustic tone similar to the observations done of Lee [41], but visually it seems completely stable. The frequency of the tone varies with flow rate and equivalence ratio. At 6 SLM of oxygen the gas velocity is high enough to avoid the acoustic oscillations over the entire ignitable regime of methane/oxygen equivalence ratio. But at a certain condition a new instability occurs, which to authors' knowledge has not been reported previously. At 6 SLM of oxygen and 8 SLM of methane corresponding to ϕ = 2.33 a rotating instability occurs which is not visible to the eyes, but is captured by the camera (Figure 9 and Movie3.avi]). It is believed to be rotating because the flame is shaped like a long spiral and not like multiple rings on top of each other. This may be seen from the slight inclination of the ripples which is most evident in the movie.

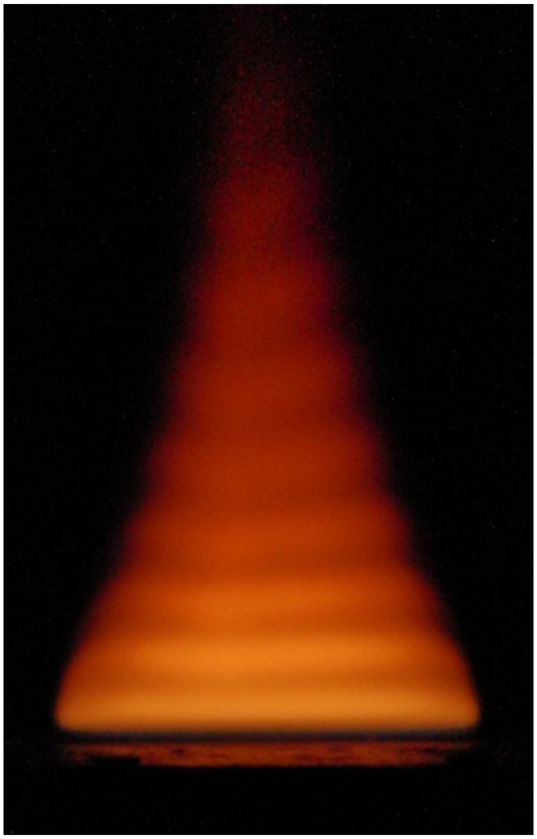

Figure 9. Image of rotating flame instability at O_2 = 6 SLM, CH_4 = 8 SLM, ϕ = 2.33 and camera shutter speed = 1/640 s.

The frequency of the instability is 105 Hz (Figure 10). If the assumption of rotating instability is true, the rotation frequency is also 105 Hz. Then the velocity of the instability in the periphery of the flame waist is around 20 m/s. It seems unrealistic that the gasses should be rotating this fast. When observing the movements of the soot suspended in the gas surrounding flame, it seems to move around slowly. Thus the instability is believed to be combustion related and not fluid dynamical. The phenomenon has not been observed at any other conditions during the experiments and it has not been investigated further during this work.

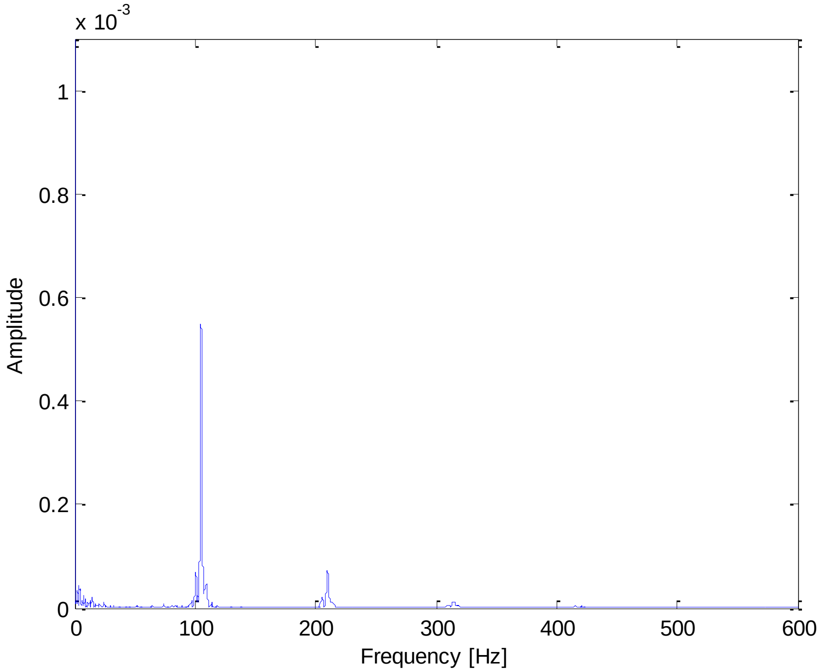

Figure 10. Frequency spectra of rotation flame instability in Figure 9.

Features of a stable, premixed flat flame

This newly established stability of premixed flat flames offers some features which are useful in combustion research and particularly in soot formation research.

The combination of uniformity and a large size of the flame yield strong emissions from molecular and Planck radiation. Line of sight based optical methods may be used to access information about the reaction processes. Illustrations of molecular radiation in the visible regime are shown in Figure 11. Due to the steadiness of the flame a long exposure time may be used without image blurring. This makes the molecular radiation bands appear even clearer than they seem to the eye. This illustrates well the opportunities to archive good spectral data from the radiant emissions. The red emission bands in Figure 11-2 are believed to be H_2O bands [42] appearing due to the high temperature and H_2O concentration, but this has not been validated further so far.

The Planck radiation emitted from flames supplied with pure fuels comes from incandescence of soot. A measure of fuels' sooting property is the critical carbon to oxygen ratio C/O_C. It is defined as the C/O ratio at which the soot inception occurs. It is usually found by adjusting the fuel to oxidizer ratio to the point where the flame turns yellow when visually observed in a dark room.

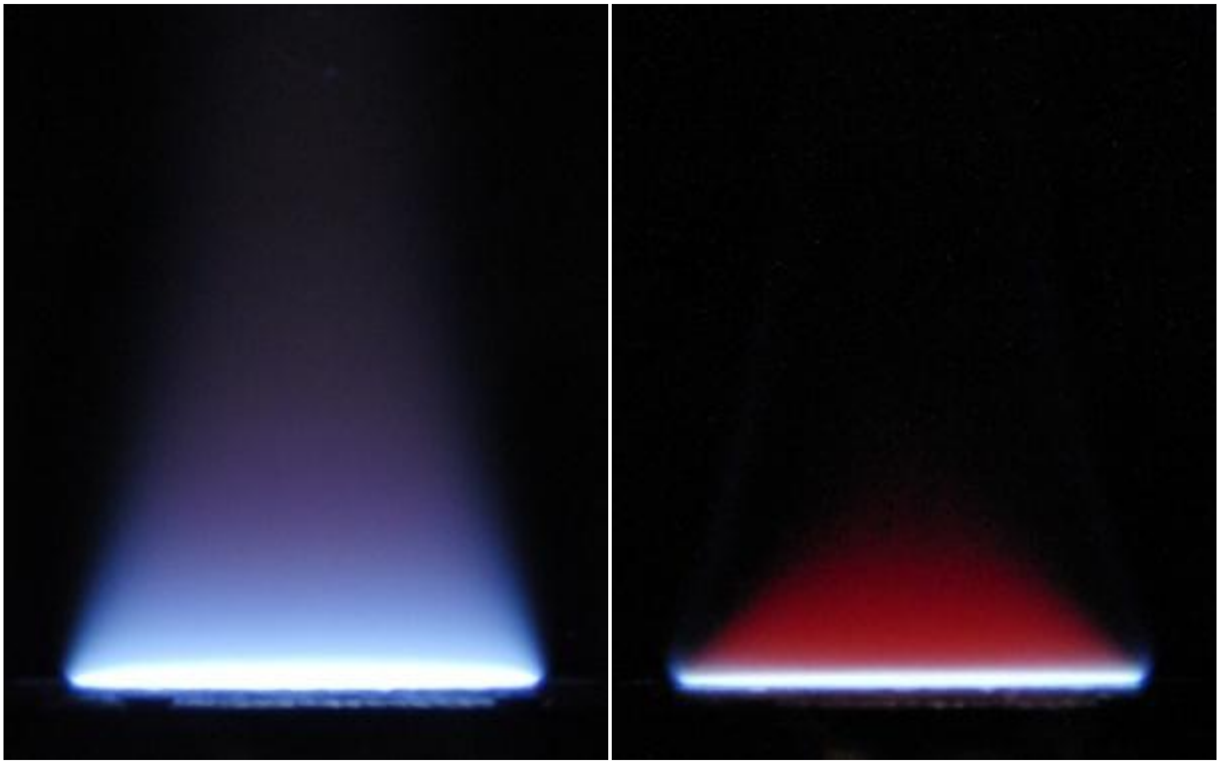

Figure 11. Left: CH radiation at the flame condition C_2H_4 = 2.1 SLM, air = 30 SLM, ϕ = 1 and camera shutter speed = 1 s. Right: H_2O radiation at the flame condition CH_4 = 4 SLM, O_2 = 6 SLM, ϕ =1.3, C/O = 0.33 and camera shutter speed = 1 s.

For ethylene/air flames the C/O_C ratios found by this method range from 0.6 to 0.66 [34, 43] dependent on the flame temperature [35]. But with methods like LIF (Laser Induced Fluorescence) and UV absorption, the presence of high molecular mass structures have been detected in ethylene/air flames below the soot threshold down to C/O = 0.48 [9, 44]. There is support to believe that the high molecular mass structures in this soot preinception regime ranging from C/O_C = 0.48 to C/O_C = 0.60 are nano particles of the size 1.5-3.5 nm [44, 45]. They act as precursors to the formation of what is considered to be the real soot. The size of the precursors is almost constant during the pre-inception regime as C/O is increased, but the number of precursors increases rapidly. At C/O_C between 0.60 and 0.70 the particle growth increases rapidly which makes the particles much more visible [44, 46, 47]. In this work the visually observed C/O_C ratio was found to be 0.62 for the ethylene/air flame. But surprisingly, luminosity is observed on the flame pictures for C/O_C ratios down to 0.5 due to the long exposure (Figure 12).

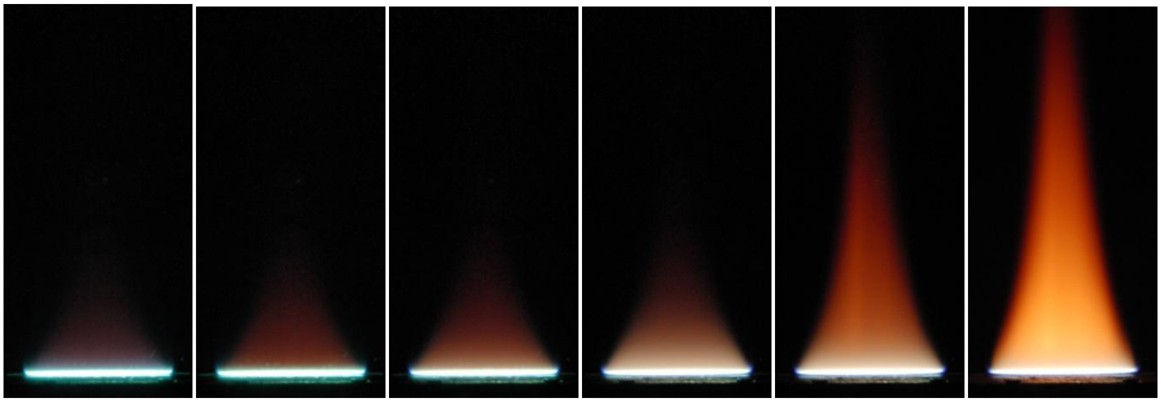

Figure 12. Picture series of ethylene/air flame at different fuel/air ratios to identify the soot inception. Air flow in all cases is 20 SLM. From left to right the flame conditions are C_2H_4 = 2.0, 2.1, 2.3, 2.5, 2.6 and 2.7 SLM, ϕ = 1.43, 1.5, 1.64, 1.79, 1.86 and 1.93 and C/O = 0.48, 0.5, 0.55, 0.6, 0.62 and 0.64. All pictures are shot with 1 s of exposure.

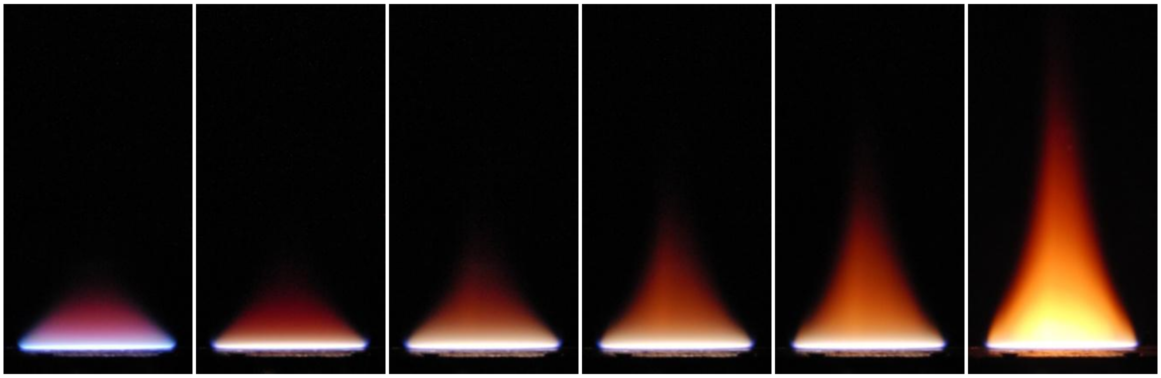

Figure 13. Picture series of methane/oxygen flame at different fuel/air ratios to identify the soot inception. Oxygen flow in all cases is 6 SLM. From left to right the flame conditions are CH4 = 3, 5, 5.5, 5.6, 5.7 and 6 SLM, ϕ = 1, 1.67, 1.83, 1.87, 1.9 and 2 and C/O = 0.25, 0.42, 0.46, 0.47, 0.48 and 0.5. All pictures are shot with 1 s of exposure.

This further supports the findings that nano particles which can emit Planck radiation are present down to C/O_C = 0.48. It should be noted that no efforts have been made so far to obtain a spectrum of the emission to verify if it is a continuous or a band spectra. But it is certainly in the visible regime due to the UV-IR filter, which only allows radiation between 380 nm and 700 nm to pass [48]. Similar observations have been made of methane/oxygen flames, but the start of the pre-inception regime is harder to identify due to the deep red emission from H_2O (Figure 13). The gradual transition from red to orange between C/O = 0.33 (Figure 11-2) and C/O = 0.42 (Figure 13-2) is consistent with findings performed with LIF and UV absorption [49]. At C/O = 0.46 the soot becomes visible to the eye which is also consistent with other findings [50].

Figure 14. Pictures of stable, lifted flames. Left: Approx. 7 mm flame lift at the condition CH_4 = 8 SLM, O_2 = 5 SLM, ϕ =3.2 and camera shutter speed = 1/640 s. Right: Approx. 34 mm flame lift at the flame condition C_2H_4 = 6.3 SLM, air = 30 SLM, ϕ = 3 and camera shutter speed = 1/20 s.

Another feature of the helium stabilized flame is the capability of stabilizing a highly lifted flame (Figure 14). This enables good access to investigate the pre flame region with methods of limited spatial resolution. In the extreme case of Figure 14-2 it was necessary to increase the helium flow to 60 SLM to reduce soot accumulation in the surrounding gas, which is still pronounced as may be seen on the scattering in Figure 14-2. A shielding flame of H2/air flame was also necessary to achieve a flat flame and to remove a remaining instability in the flame front periphery.

Thermometry of the flame

In combustion processes the chemical reaction rates are strongly dependent on the local temperature. The temperature is influenced by the heat transfer processes where the driving force is the temperature differences. Thus a strong coupling exists between heat release from the reactions and heat loss from the heat transfer processes. This is further complicated by including radiative heat transfer, which contributes significantly to the total heat transfer in most flames.

In the attempts to develop valid combustion and heat transfer models, it is of highest importance to know the flame temperatures in laboratory flames suited for model validation.

Measurement of the temperature in a flame is not a trivial task. Different thermometry techniques have been developed typically just suited for a range of flame equivalence ratios. Qualitatively these methods show good agreement but quantitatively inconsistencies of several hundred Kelvin are not unusual. Some of the methods and their limitations are shortly described in the paper.

The method of IR emission and absorption by CO_2 is the method dealt with in this work. An experimental setup for this technique is developed for thermometry in pre-mixed flat flames. A robust method to interpret the derived temperature spectra has been developed. The method was validated with regard to precision and accuracy separately. The accuracy validation was based on comparison with results from identical flames but obtained with different thermometry techniques. A wide range of equivalence ratios and flow rates was used for the flames in the investigation, to reveal if the method had any limitations with regard to the flame condition.

Flame thermometry methods

Intrusive methods like the insertion of thermocouples, suffer from the disadvantage of measuring the temperature of the bead and not of the gas. The bead constantly losses heat by radiation to the cold surroundings and by conduction through the leads. The heat loss from the bead is balanced with the heat transfer in the flame, and is, therefore, influenced by the composition and velocity of the combustion gas. Corrections to these effects may be applied and validated by using different thermocouple bead diameters [51]. The uncertainty of thermocouple measurement is increased in rich and particularly in sooting flames. The soot deposition on the bead influences the heat transfer processes to the bead and makes it difficult to perform the heat loss correction. In rich flames the thermocouple tends to promote exothermic reactions of the non-equilibrium reaction products by catalytic reactions on the bead surface, resulting in too high temperatures. Different surface treatments of the thermocouple have shown to reduce the catalytic reactivity [52].

The reversal technique is an optical line of sight method that is often used in flame thermometry. That the technique is called reversal means that the radiance from an adjustable light source is measured through the flame. The radiance from the light source is adjusted to the point where it is not detectable whether the flame is present or not. At that point, the temperature of the flame equals the temperature of the source if the source is a blackbody. If it is not black, the spectral emissivity needs to be known. The tungsten strip lamp is often used as source because it is commercially available with emissivity calibrations. But measurements with the tungsten strip lamp are limited to visible and near IR light due to transparency of the glass. Reasonable absorption in the flame must be present for the method to work. The Kurlbaum method is a reversal technique for sooting flames where the soot is the absorbent. With the sodium line reversal method, small amounts of sodium are added to the flame. The sodium absorbs strongly in two spectral lines, which are used to determine the reversal point. This makes the sodium line reversal technique useful for non-sooting flames. Because the reversal methods are usually limited to visible light, the scattering by soot reduces the accuracy [52].

Two or multicolor methods are optical line of sight methods. The methods are based on a qualitative determination of the spectral shape of the gray body emission from sooting flames, and correlate it with the Planck radiation law. Two emission measurements at different wavelengths are all that are needed to determine the temperature, but it relies on the assumption that the absorption coefficient is constant. Actually the absorption coefficient for soot weakly depends on wavelength and the size of the particles, making color method less accurate [52].

The Rayleigh scattering of laser light is a point measurement. The Rayleigh scattering of a laser beam is measured in a point along the beam. The intensity of the scattered light depends on the molecular density and the Rayleigh cross section of the molecules. If the composition and the pressure are known, the temperature may be calculated. As a reference, the scattering of pure N_2 at a known temperature is measured with the same experimental setup. Because Mie scattering by particles drowns out the Rayleigh signal, the method is limited to non-sooting flames. The flame composition may be determined from equilibrium calculations [53]. This is a good approximation for lean and stoichiometric flames, but for rich flames the gas composition departs from equilibrium which may cause the method to be less accurate.

Coherent Anti Stokes Raman Shift (CARS) spectroscopy is a sophisticated but also costly point measurement technique performed with multiple laser beams. Different variants of the method exist. In general, the method measures the Stokes Raman scattering, which is different from Rayleigh and Mie scattering by being spectrally shifted relative to the incident light. Due to this shift, the Stokes Raman scattering by one kind of molecule may be separated from scattering by soot and even the Stokes Raman scattering by other kinds of molecules. From the Stokes Raman spectra of flames, a lot of information may be extracted about temperature and composition. One challenge to overcome is that the signal from spontaneous Stokes Raman scattering is weak. With CARS the interference of two laser beams is used to drive the Stokes Raman oscillation and the signal is probed with a third laser making the signal orders of magnitude stronger and reducing the background luminosity from soot [54].

The method of IR emission and absorption by CO_2 is the method dealt with in this work. The development of the method is mainly attributed to work of Tourin [55]. In later work the method has been extended by Solomon [56] also to determine concentrations of soot and some gas concentrations in flames. It has been further extended with tomographic reconstruction by Best [57] to derive point measurements from traversed line of sight measurements. The impressive work by Solomon and Best was performed on a diffusion flames while the present work is performed on pre-mixed flat flames. This makes a substantial difference when a line of sight method is applied to measure the flames.

The IR emission absorption method is based on the principle that the CO_2 transition lines in the IR between 2100 and 2400 cm^{-1} are close and broadened enough to be considered as gray bands. The grayness of the bands may be found by measuring the absorption by the flame. Then the CO_2 temperature may be derived from measurements of the flame emissions, based on a black body calibration of the IR spectrometer.

The advantages of the method are that it is non-intrusive in every sense, it is not influenced by scattering from soot, due the large wavelength used for detection compared to the size of the soot particles, and no prior knowledge of the flame is required, such as gas composition, velocity, conductivity, soot concentrations etc. This makes the method applicable to the entire range of flame stoichiometries and fuels as long as sufficient CO_2 is produced. From economic and practical points of view, the method is competitive to the laser methods due to a reasonable price, robustness and the flexibility of modern Fourier Transform Infra Red (FT-IR) spectrometers, which may be used for a large variety of measurements and not only flame thermometry.

Disadvantages of the method are that it is a line of sight method and the temperature and CO_2 concentration along the line need to approach uniformity to minimize self-absorption. The flame thickness should also be constant during the measurements for best precision, thus steadiness of the flame is preferred to reduce the required amount of averaging.

These properties of the IR emission absorption method make it well suited for helium stabilized pre-mixed flat flames. Flat flames usually flicker due to buoyancy driven shear layer instability. This instability is completely removed by having the flame surrounded by helium to equalize the gas densities [58].

In this work, thermometry by the IR emission absorption method was developed specifically for helium stabilized flat flames. A commercial FT-IR spectrometer was used to measure the 400 to 4000 cm^{-1} range of the IR spectrum. A large number of measurements were performed on propane and ethylene flames of various flame stoichiometries and gas velocities. Different strategies for interpreting the obtained temperature spectra have been evaluated. Experiments with different thermometry techniques, reported in the literature, have been reproduced and the results compared.

The IR thermometry experimental setup

Details about the burner setup and helium stabilization are described in a previous work [58] and will only be described briefly in the following.

The flat flame burner is the widely described [59,60] standard bronze 60 mm diameter Holthuis & Associates burner also known as a McKenna burner. The outer ring of the burner is normally used to create an N_2 co-flow around the flame. In this work it was used as an outer burner with a stoichiometric hydrogen flame to thermally shield the center flame and improve uniformity. Since the shielding flame only had a limited effect, it was just used for some experiments in the method development and not in the final setup. To enable a co-flow of helium around the two flames, an outer screen was added to the standard burner. The burner was located in a steel chamber with W/L/H = 200/200/800 mm and mounted on an arrangement that enabled traversing it up and down inside the chamber.

The gas flows led to the burners and the co-flow ring was controlled with a Hovagas G6 gas mixer. It was equipped with two 0.25-5 standard liters pr. minute (SLM), two 0.5-10 SLM, one 1.5-30 SLM and one 3-60 SLM channels, referring to SLM of air. The mixer was calibrated with air to control the channels within +/- 1 % of the reading. The flow was converted for other gases than air with standard flow conversion factors used for mass flow controllers.

The fuel gasses used for this work were propane and ethylene, both certified to 99.5 % purity. The compressed air was dried to a dew point of 276 K. The helium was standard balloon helium.

To prevent the flame from flicker the burner chamber was purged with 10-30 SLM of helium through the added screen. The helium flow required to stabilize the flame depended on the flame size and was kept as low as possible to minimize the helium consumption.

In Figure 15 is a sketch of the optical path in the experimental setup. The FT-IR spectrometer used in the work was a Nicolet 6700 from Thermo Fisher Scientific. It is a multipurpose instrument that enables different configurations of internal components and it is possible to use the spectrometer in many different applications via the sample compartment and the external source port. The instrument used was equipped with a Deuterated Triglycine Sulfate (DTGS) detector, a liquid nitrogen cooled Mercury Cadmium Telluride (MCT) detector and a Potassium Bromide (KBr) beam splitter. Throughout this work the DTGS detector was used because the MCT detector easily became saturated and the higher sensitivity did not seem to offer any advantages in this application. Due to the linearity of the DTGS detector, calibrations performed to correct for non-linearity could also be omitted.

The spectrometer was also equipped with a flipping mirror that enabled switching between the internal source and an external source seen through the external source port. The OMNIC software package from Thermo Fisher Scientific was used to control instrument and acquire the data. Many different settings of the instrument were tried, but all the presented results were made with a resolution of 4 cm^{-1}, a mirror velocity of 0.1581 cm/s and 10 (in few cases 32) scans per sample. This offered a good compromise between sampling time (Δt = 39 s) and precision. The indoor environment in the laboratory was stable enough to make N_2 purging of the instrument unnecessary in this application.

Aperture 1 (Figure 15) was located in the sample compartment to prevent the rays that were not parallel in the interferometer from reaching the detector. These non-ideal rays reduce the spectral resolution, a phenomenon called self-apodization [61]. An aperture size of 2 mm was found appropriate for this work and was used in all the presented results. Experiments with an aperture size of 1 mm, a spectral resolution of 2 cm^{-1} and 32 scans per sample did not show any changes to the measurements and confirmed that our basic settings were sufficient.

The IR beam reaching the spectrometer was shielded from the surroundings to maintain constant temperature and concentrations of CO_2 and H_2O in the air crossed by the beam and to prevent radiation from hot surfaces to reach the spectrometer. A 50 mm diameter plano convex KBr lens with 1 m focal length was used to focus the IR beam to facilitate alignment of the black body. This also made it easier to ensure that the field of view did not strike the walls but only the bottom of the black body cavity where the temperature was known. The lens was located inside the shielding tube and was followed by aperture 2 (Figure 15). Aperture 2 was used to restrict the line of sight diameter to improve the spatial resolution. An aperture size and thus line of sight diameter of 6 mm was found appropriate for this work and was used in all the presented results.

The IR path crossed the flame chamber through two silicon windows. The transmittance of silicon is approximately 50 % in the IR spectrum of interest and the rest is reflected. To avoid reflections between the two windows, they were tilted at 30˚ relative to the detection path. Between the windows and the flame chamber the IR path was shielded from combustion products by purging the tubes with helium. An adjustable purge tube extension with 21 mm inner diameter was used to shield the IR path from combustion products between the chamber wall and the flame. The distance from the purge tube extensions to the flame and the purging flow rate of helium had great influence on the quality of the measurements. The best results were achieved if the end of the purge tube extensions were located 1-2 mm from the hot flame products and if a helium purge flow of 3 SLM was used for each purge tube.

In this setup the black body both served as a source for the absorption measurements and as a temperature reference for emission measurements. When it was used as temperature reference the window between the flame and the black body was exchanged with a helium purged tube, connecting the black body with the flame chamber.

The black body was made from a modified hardening oven containing a cavity made of high temperature nickel alloy. The internal diameter of the cavity was 21 mm, thus proper alignment with the detection path pointing on the bottom of the cavity could easily be achieved. The power supply to the hardening oven was controlled by a PID temperature controller receiving the temperature from a thermocouple in the bottom of the cavity. The black body temperature was 1073 K in all the measurements and was constant within +/- 3 degree.

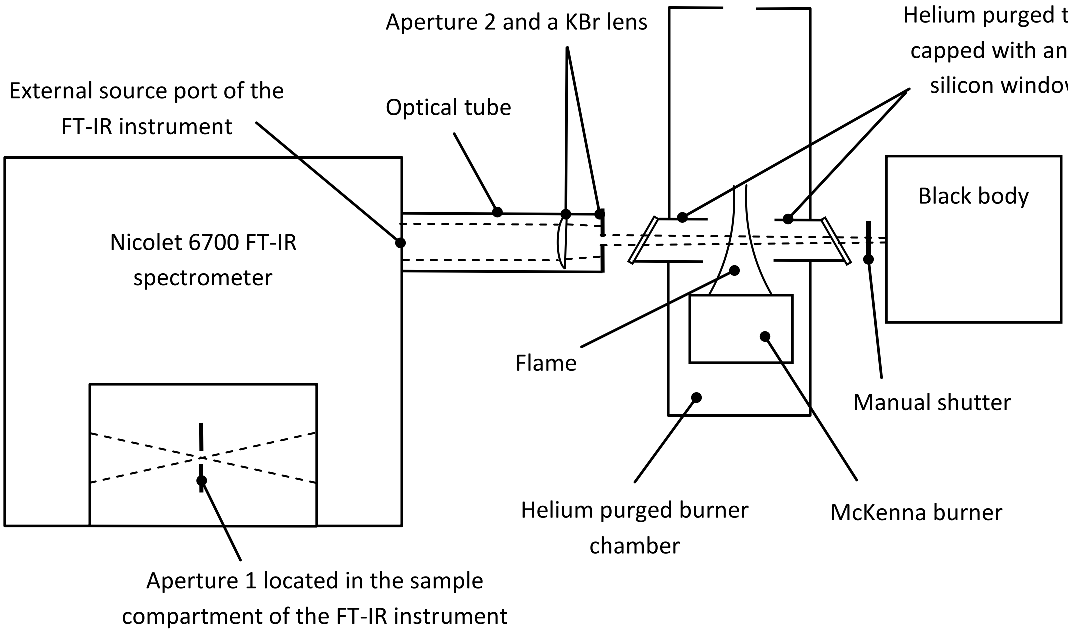

Figure 15: Sketch of the experimental setup and the optical path used for flame thermometry.

A manual shutter was located between the burner chamber and the black body. The shutter was water cooled and coated with black rubber to minimize back reflection and thermal radiation from it.

Four spectra were needed to derive the temperature with the described setup:

- A reference spectrum of the black body (BBREF spectrum) without the flame and with helium purging of the burner chamber, connection tube and black body. BBREF spectra were acquired before and after the series of flame measurements.
- A source spectrum of the black body (BB spectrum) with the second window in place, without the flame and with helium purging of the burner chamber. BB spectra were acquired between the BBREF spectra and the flame measurements.
- A spectrum of the black body seen through the flame (FBB spectrum).
- A spectrum of the flame only (F spectrum).

When the BBREF and the BB spectra were first acquired, the FBB and flame spectra could be acquired within a couple of minutes by opening and closing the shutter (Figure 15). Thus about hundred temperature measurements at different flame conditions and heights, including warm up of the black body could be achieved during a day. There was no need for maintenance or cleaning of the experimental setup during the entire work done, except for an automatic alignment of the fixed mirror in the FT-IR spectrometer which was done routinely every morning.

Mathematical treatment of the spectra was performed in Matlab and the combustion equilibrium calculations used in the method validation were performed with Gaseq 0.79 software [62].

Theory of the IR emission absorption method

The method of IR emission and absorption by CO_2 is based on the principle that the CO_2 transition lines in the IR around 2300 cm^{-1} are so close together and broadened enough by Doppler and pressure effects that they may be considered as gray bands. Then the grayness of a band may be found by measuring the absorption by the flame and the emission, and the CO2 temperature may be derived from the measured flame emission, based on a black body calibration of the spectrometer.

If the observed path through the flame is considered homogeneous and scattering is ignored, the radiation transfer equation (Eq. 7) may be used to determine the absorption α (Eq.3) at a wavelength λ from the measured radiance I. The wavenumber $\tilde{\nu}$ is the inverse of the wavelength λ.

$$I_{FBB}(\lambda) = I_F(\lambda) + \left(1 - \alpha_F(\lambda)\right) I_{BB}(\lambda) \tag{2}$$

$$\alpha_F(\lambda) = 1 + \frac{I_F(\lambda) - I_{FBB}(\lambda)}{I_{BB}(\lambda)} \tag{3}$$

According to Kirchhoff's law, absorption equals emission $\alpha_F(\lambda, T_F) = \varepsilon_F(\lambda, T_F)$. The flame radiance may then be related to the Planck radiation with Eq. 4 and Eq. 5. Here *h* is the Planck constant, *c* is the speed of light and *k* is the Boltzmann constant.

$$I_F(\lambda) = \varepsilon_F(\lambda, T_F) I_{Planck}(\lambda, T_F) \tag{4}$$

$$I_{Planck}(\lambda, T) = \frac{1hc^2}{\lambda^5} \frac{1}{e^{hc/(\lambda kT)} - 1} \tag{5}$$

The true radiance I and the measured radiance I^* are not directly comparable due the wavelength dependent detector sensitivity. It is convenient to relate the Planck radiance with the BBREF radiance as in Eq. 6 because the detector correction factor $c_{det}(\lambda)$ cancels out by the use of Eq. 4.

$$\frac{I_{Planck}(\lambda, T_F)}{I_{BBREF}(\lambda, T_{BBREF})} = \frac{c_{det}(\lambda) I_F^*(\lambda, T_F)}{\varepsilon_F(\lambda, T_F) c_{det}(\lambda) I_{BBREF}^*(\lambda, T_{BBREF})} = \frac{e^{hc/(\lambda k T_{BBREF})} - 1}{e^{hc/(\lambda k T_F)} - 1} \tag{6}$$

By isolating the flame temperature in Eq. 6 an expression for the temperature, dependent on wavelength is derived (Eq. 6). According to the homogeneousity assumption introduced in Eq. 2, the temperature should be constant. Thus, if the observed path through the flame really is homogeneous the wavelength dependence may be left out ($T_F(\lambda) = T_F$).

$$T_F(\lambda) = \left(\frac{\lambda k}{hc} ln \left(\frac{\varepsilon_F(\lambda, T_F) I^*_{BBREF}(\lambda, T_{BBREF}) \left(e^{hc/(\lambda k T_{BBREF})} - 1 \right)}{I^*_F(\lambda, T_F)} + 1 \right) \right)^{-1} \qquad 7$$

Since the observed path through the flame is not homogeneous in reality, the temperature will depend on wavelength. This dependency is determined by a number of physical factors and some interpretation of the temperature spectrum is necessary to determine the flame temperature.

Interpretation of the temperature spectra

A large amount of data is provided with the acquired spectra. But it is a challenge to convert the data into useful information, particular at high temperatures where the spectral models are not fully developed. This work aims at formulating a simple strategy to interpret the spectra without the use of any pre-knowledge.

An example of the spectra recorded from a stoichiometric propane/air flame (Figure 16) shows emission bands from H_2O at 1200 to 2000 cm^{-1}, CO_2 at 2100 to 2400 cm^{-1} and CO_2 together with H_2O at 3200 to 4000 cm^{-1}. In rich flames CO emission bands also appear around 2100 cm^{-1}. A combination of high absorption (Figure 17) and good detector sensitivity (Figure 18) makes the CO_2 band between 2100 and 2400 cm^{-1} the best choice to derive the flame temperature. This becomes evident by observing the noise on the full temperature spectrum in Figure 19.

The temperature spectrum between 2100 and 2300 cm^{-1} in Figure 19 is not a plateau with constant temperature. This was also realized by Silverman [63], and may be explained with the right wing broadening (low wave number) of the CO_2 band as temperature increases. Due to the strong temperature dependence of wing intensity it will not be absorbed by the colder flame periphery to the same extent as the center of the band. Silverman found for a CO/O_2 flame that the temperature spectrum increased with decreasing wave number until 2200 cm^{-1} where it became flat at 2160 K which was assumed to be the core temperature of the flame. The wave number at which the plateau is reached will depend inversely on the temperature. In this work the plateau never became evident due to the presence of H_2O lines which obscure the weak absorption from the wing tip. These features of the CO_2 band are actually the strength of the IR emission absorption method, because it makes it possible to determine the core temperature of a flame with a line of sight method going through colder regions.

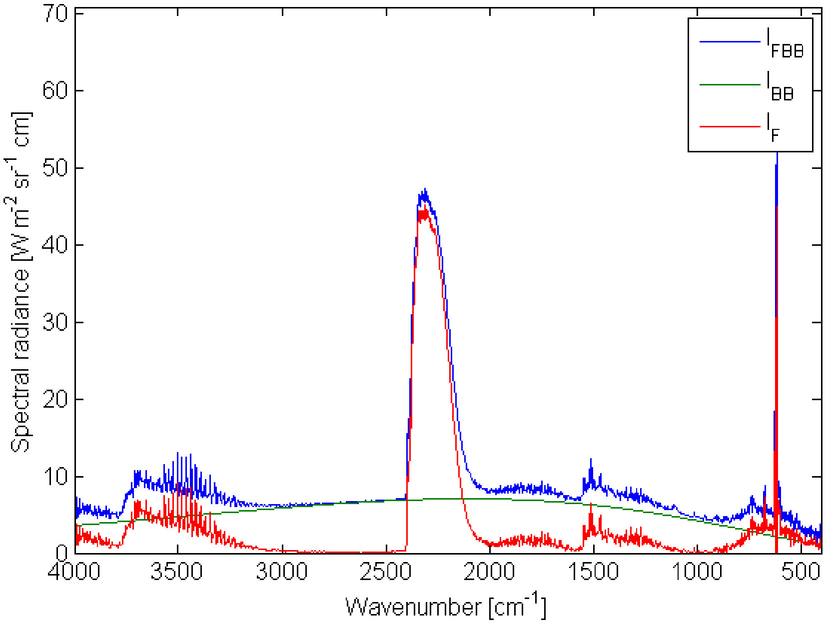

Figure 16. A collection of spectra measured on a stoichiometric propane/air flame with 30 SLM air flow.

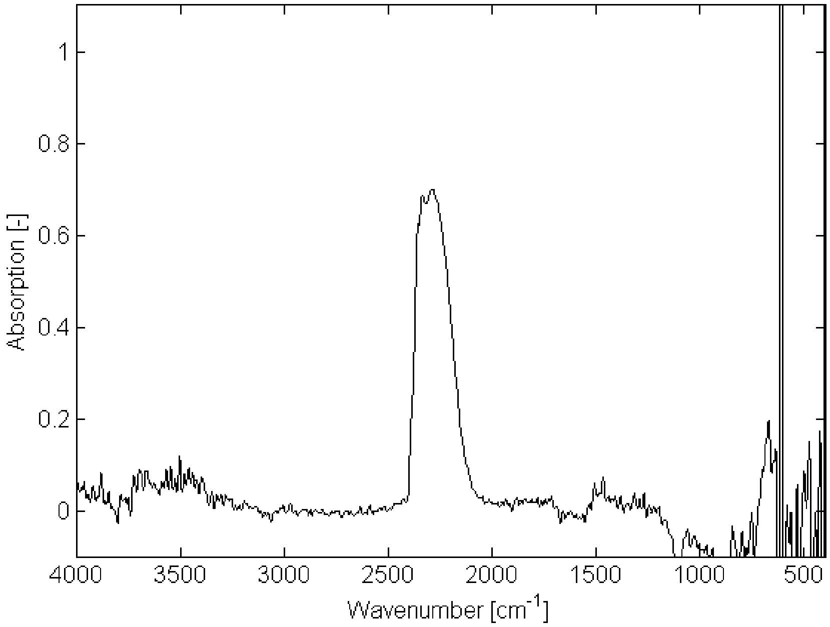

Figure 17. The absorption spectrum derived with Eq. 2 from the spectra in Figure 16.

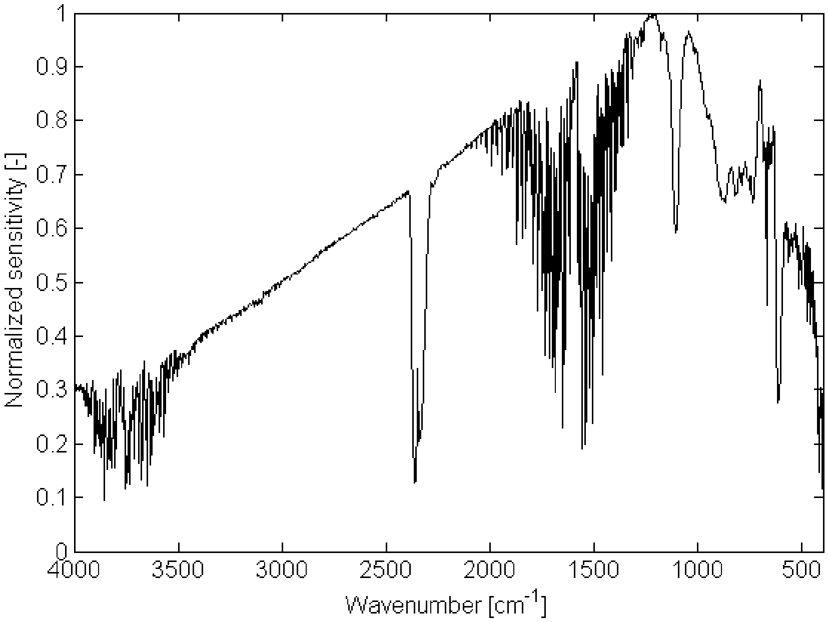

Figure 18. A spectrum of the detector sensitivity derived from the measured and the calculated black body spectrum. The curve is not smooth due to absorption from atmospheric CO_2 and H_2O in the unpurged FT-IR spectrometer.

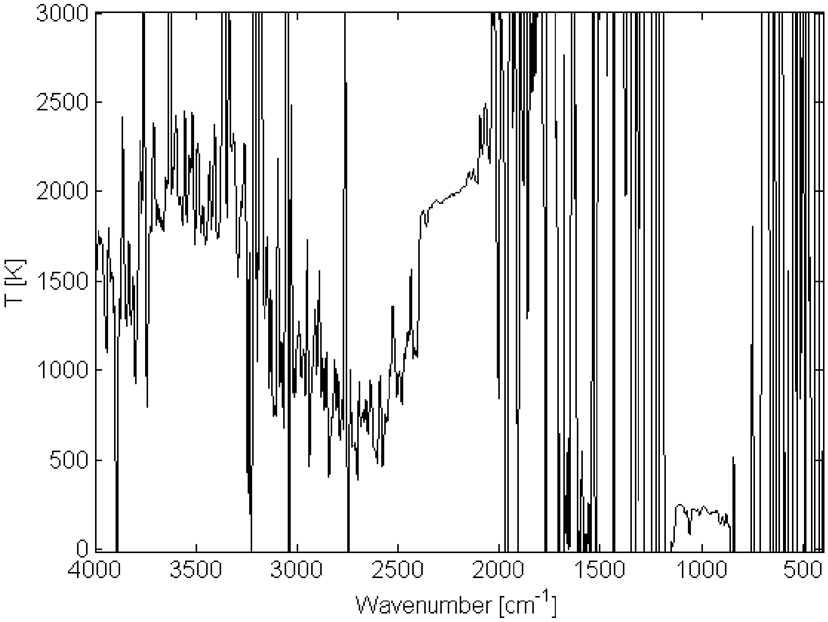

Figure 19. The full temperature spectrum derived with Eq. 6 from the spectra in Figure 16.

This is clearly illustrated in Figure 20 and Figure 21 where temperature spectra are compared from experiments with and without protecting the IR path from cold combustion products with Helium purged tubes. Without the tubes the IR path passes through 70 mm of cold combustion gasses on both sides of the flame. These figures reveal a spectral window in which reasonable temperatures may be measured even under very bad experimental conditions. The large dip on the right side of the window is caused by cold CO, which is more pronounced for the rich flame in Figure 21 than in Figure 20. The figures illustrate how a quick examination of the temperature spectra will reveal the state of the experimental condition, and thus the quality of the measurement.

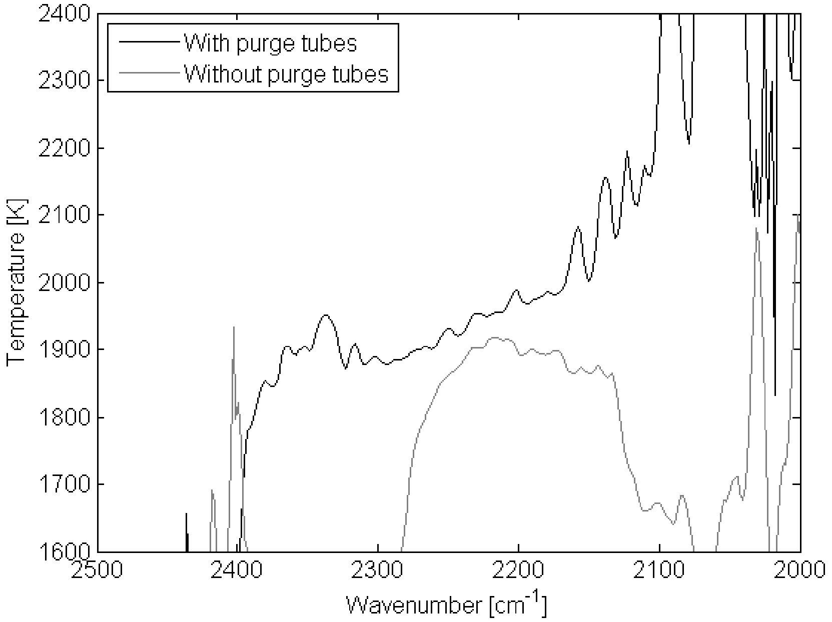

Figure 20. Two measured temperature spectra for a stoichiometric propane/air flame 30 SLM cold flow of air. One spectrum is measured with properly purged tube extensions leading to the flame and the other is measured without purge tube extensions.

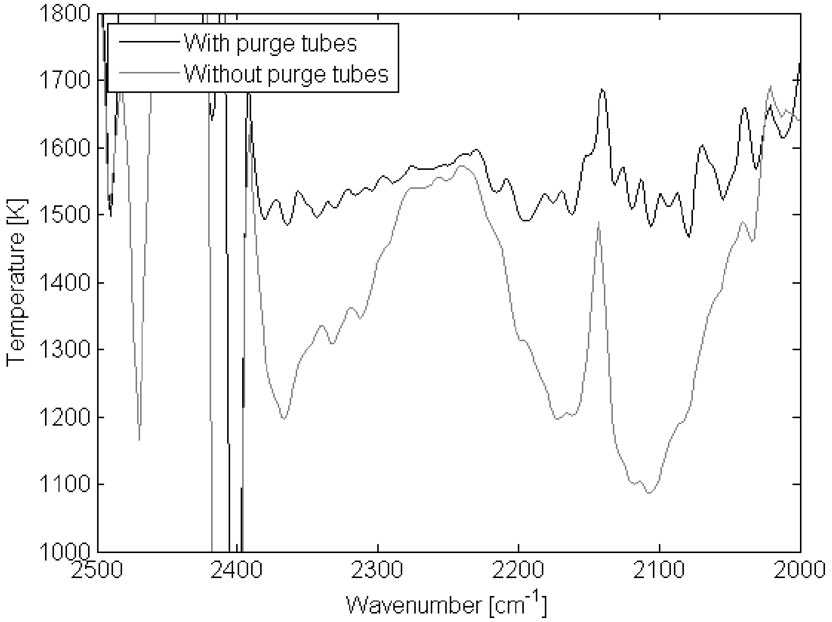

Figure 21. Two measured temperature spectra for an ethylene/air flame with φ = 2.3 and 10 SLM cold flow of air. One spectrum is measured with properly purged tube extensions leading to the flame and the other is measured without purge tube extensions.

Figure 20 and Figure 21 also illustrates that the interval from 2220 to 2250 cm^{-1} would be the most conservative choice to determine the temperature. This is also the interval chosen by Marran [64] for measuring the exhaust temperature from a turbine engine with the IR emission absorption method.

In attempts to retrieve the core temperature of the flame, two dynamic methods for choosing the interval were tested along with the fixed interval from 2220 to 2250 cm^{-1}. One is based on recommendations from Tourin [55] that absorption of minimum 0.2 is preferred to achieve precise temperature measurements. Thus, the wave number is found where the high temperature wing of the absorption spectra crosses 0.2. This wave number is used as the lower limit in an interval of 30 cm^{-1} used to calculate the average temperature. The second dynamic method is identical but with an absorption of 0.3 as criteria.

Method validation

In this method validation the precision and the accuracy of the method are treaded separately. Precision refers to the reproducibility of measurement results, while accuracy refers to the absolute validity of the measurement result.

During the development of the method presented in this work, more than 250 temperature measurements have been performed on a large variety of flames and experimental setups. It has not been possible to carry out a large number of measurements with the final experimental setup to determine the precision of the method. Thus, the approach used in this method validation is to use all the data acquired during the method development to perform an error analysis. Consequently the error analysis more reflects the methods sensibility to variations in the experimental setup than the precision that may be achieved with an optimal setup. This approach is believed to be appropriate for the development stage of the method and is useful to validate the sensitivity of the temperature spectra interpretation strategies to varied experimental conditions.

An error analysis of the influence from differences of BB and BBREF spectra is shown in Table 1. The 16 BB and BBREF spectra vary by being acquired on different days, before, during or after the flame measurement series, with good or bad FT-IR alignment and with or without purging the flame chamber and black body.

The temperature and absorption spectra obtained with different BB and BBREF spectra are shown in Figure 22 and Figure 23. The two spectra that deviate a substantially from the rest were made without purging the flame chamber and the black body. The rest deviate slightly in magnitude which is mainly caused by the cyclic variations of the black body temperature with +/- 3 K. As Table 1 illustrates, the influence of variations in the actual black body temperature on the flame temperature is stronger for the BB spectra than for the BBREF spectra. This is due to the faulty absorption spectra obtained if the actual black body temperature is low when the BB spectrum is acquired and high when the FBB spectrum is acquired.

	Values of interval $[min(\tilde{\nu}_{\alpha=0.2}), min(\tilde{\nu}_{\alpha=0.2})+30]$			Values of interval $[min(\tilde{\nu}_{\alpha=0.3}), min(\tilde{\nu}_{\alpha=0.3})+30]$			Values of interval [2220, 2250] cm^-1		
	T_{min} $\boldsymbol{T_{mean}}$ T_{max} [K]	σ [K]	**σ [%]**	T_{min} $\boldsymbol{T_{mean}}$ T_{max} [K]	σ [K]	**σ [%]**	T_{min} $\boldsymbol{T_{mean}}$ T_{max} [K]	σ [K]	**σ [%]**
16 different BB spectra	1975 **2005** 2035	17	**0.87**	1961 **1978** 1996	10	**0.50**	1938 **1947** 1958	7	**0.35**
16 different BBREF spectra	1974 **1982** 1988	5	**0.23**	1962 **1970** 1980	6	**0.29**	1937 **1944** 1955	6	**0.32**
16 different BB and BBREF spectra	1975 **2011** 2075	20	**0.99**	1964 **1983** 2009	15	**0.73**	1938 **1954** 1975	12	**0.63**

Table 1. Error analysis of the influence from using different BB and BBREF spectra with unchanged FBB and flame spectra. The spectra are obtained from a stoichiometric propane/air flame at 20 mm height with a cold gas velocity of 18.4 cm/s

.

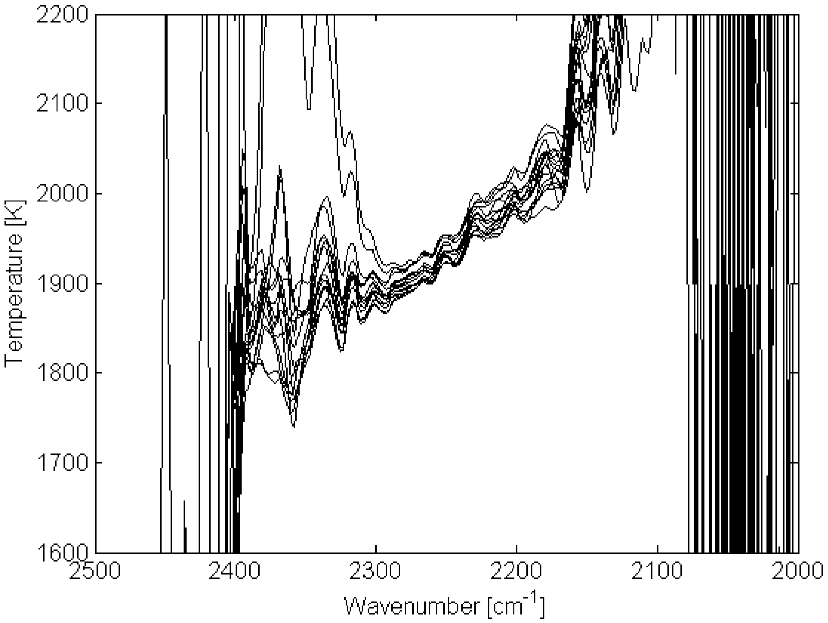

Figure 22. Collection of temperature spectra used in Table 1 obtained with different BB and BBREF spectra.

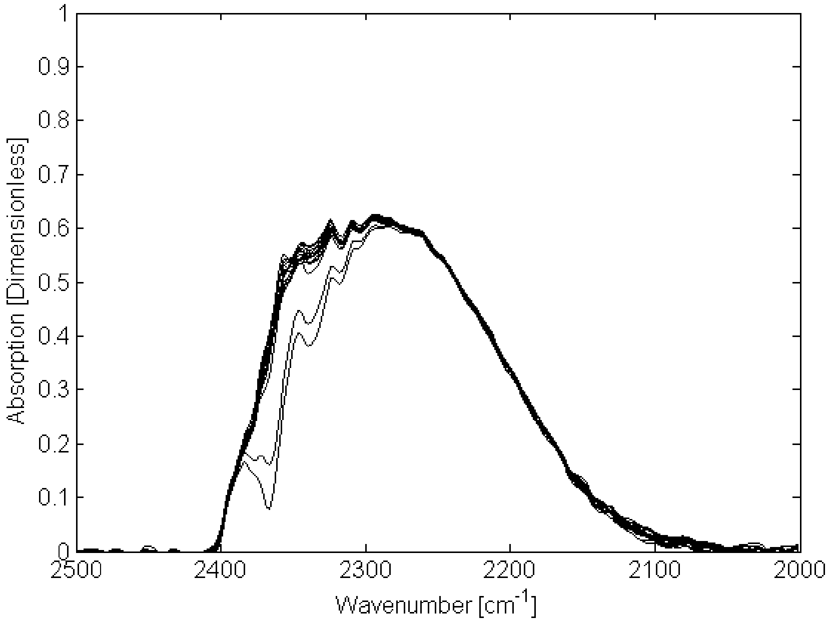

Figure 23. Collection of absorptiom spectra used in Table 1 obtained with different BB and BBREF spectra.

The precision of the IR emission absorption method was evaluated for different flames and experimental conditions, and the results are collected in Table 2. The BB and BBREF spectra used for the individual temperature calculations were those made on the same day as the actual flame measurement to minimize day by day variations. Whenever a flame temperature for a particular flame at a particular height was measured more than once, the standard deviation σ was calculated and tabulated. Measurements have been performed with a wide variety of experimental conditions, which made it reasonable to classify the data sets in class 1, 2 and 3.

- Class 1 data sets only contain measurements made under nearly optimal experimental conditions with Helium stabilized flames. These conditions are achieved with an experimental setup as described in the experimental setup section.
- Class 2 data sets contain measurements made under varied experimental conditions with Helium stabilized flames. This includes different purge flows in the optical path, the use of H_2/air shielding flames, the use of He co-flow through the annular shroud ring, and different positions of the purge tube extensions.
- Class 3 data sets contain all measurements performed on a particular flame including those made under very poor experimental conditions. This includes measurements made with unstable flames in air (only for $\varphi \leq 1$) with an open flame chamber or with nitrogen as coflow in a closed flame chamber. It also includes helium stabilized flames with nitrogen used as purge gas in the optical

path and measurements made without the purge tube extensions between the flame and the chamber wall.

To validate the three considered methods for interpreting the temperature spectra, the errors for each method are also presented in Table 2. The table clearly shows that the fixed interval method is least sensitive to the experimental conditions, closely followed by the $\alpha = 0.3$ method, while the $\alpha = 0.2$ method may fail completely if measurements are made under poor experimental conditions. Under good experimental conditions the $\alpha = 0.2$ method is slightly less precise than the other two strategies which are equal. But for stoichiometric flames the α strategies result in higher temperatures than the fixed interval method. The $\alpha = 0.2$ method measure slightly higher temperatures than the $\alpha = 0.3$ method. As discussed earlier the higher temperature from the α methods are believed to represent the core temperature of the flame more accurately than the fixed interval method, because the temperature is retrieved further toward the high temperature wing of the CO_2 absorption band.

To illustrate how diverse the experimental conditions were for some data sets of Table 2, temperature and absorption spectra for the entire case 1 data set is shown in Figure 24 and Figure 25. The absorption happened to be above 1 when no purge tube extensions were used (Figure 25). The large optical thickness of the cold CO_2 did not allow any background radiation from the black body to pass in the range from 2300 to 2400 cm^{-1}. Thus even the slightest change in the flame thickness between the acquisition of the FBB spectrum and the flame spectrum caused the calculated absorption to deviate from one.

The different layers of absorption spectra were caused by different locations of the purge extension tube and different purge flow rate. This forced the thickness of the flame to vary from one series to another.

In spite of these large variations, the temperature spectra are densely located around the same temperature (Figure 24) between 2200 and 2250 cm^{-1}. A reasonable precision of less than +/- 2 % was also found with an appropriate interpretation of the temperature spectra.

Based on this analysis it was decided to use a strategy with the $\alpha = 0.3$ method for flames with $\varphi \leq 1.5$ and the fixed interval method for $\varphi > 1.5$. With this strategy and proper experimental conditions it is reasonable to believe that a precision of +/- 1 % may be achieved for a wide range of flames produced on a flat flame burner.

Case	Flame description	Values of interval $[min(\tilde{\nu}_{\alpha=0.2}), min(\tilde{\nu}_{\alpha=0.2}) + 30]$			Values of interval $[min(\tilde{\nu}_{\alpha=0.3}), min(\tilde{\nu}_{\alpha=0.3}) + 30]$			Values of interval [2220, 2250] cm^-1	
		$\tilde{\nu}_{\mathrm{lower,mean}}$ $\tilde{\nu}_{\mathrm{upper,mean}}$ [cm^{-1}]	$T_{\min}$ $\boldsymbol{T_{\mathrm{mean}}}$ $T_{\max}$ [K]	σ [K] **σ [%]**	$\tilde{\nu}_{\mathrm{lower,mean}}$ $\tilde{\nu}_{\mathrm{upper,mean}}$ [cm^{-1}]	$T_{\min}$ $\boldsymbol{T_{\mathrm{mean}}}$ $T_{\max}$ [K]	σ [K] **σ [%]**	$T_{\min}$ $\boldsymbol{T_{\mathrm{mean}}}$ $T_{\max}$ [K]	σ [K] **σ [%]**
1	C_3H_8/air, φ = 1, 30 SLM air, v_{cf} = 18.4 cm/s, H = 20 mm, **Class 3**, Samples = 31	2169 2199	1866 **1980** 2072	44 **2.23**	2192 2222	1852 **1968** 2052	37 **1.89**	1843 **1948** 2035	37 **1.88**
2	C_3H_8/air, φ = 1, 30 SLM air, v_{cf} = 18.4 cm/s, H = 20 mm, **Class 2**, Samples = 16	2162 2192	1958 **1988** 2024	19 **0.97**	2184 2214	1964 **1979** 2006	14 **0.70**	1938 **1955** 1987	17 **0.87**
3	C_3H_8/air, φ = 1, 30 SLM air, v_{cf} = 18.4 cm/s, H = 20 mm, **Class 1**, Samples = 10	2165 2195	1966 **1982** 2007	13 **0.65**	2187 2217	1964 **1970** 1984	7 **0.34**	1938 **1945** 1970	10 **0.50**
4	C_3H_8/air, φ = 1.5, 30 SLM air, v_{cf} = 18.8 cm/s, H = 20 mm, **Class 3**, Samples = 9	2178 2208	1794 **1847** 1896	36 **1.92**	2209 2239	1812 **1847** 1885	21 **1.16**	1810 **1845** 1883	21 **1.16**
5	C_3H_8/air, φ = 1.5, 30 SLM air, v_{cf} = 18.8 cm/s, H = 20 mm, **Class 2**, Samples = 5	2179 2209	1794 **1821** 1849	24 **1.29**	2212 2242	1812 **1833** 1859	17 **0.95**	1810 **1833** 1861	19 **1.01**
6	C_3H_8/air, φ = 1.5, 30 SLM air, v_{cf} = 18.8 cm/s, H = 20 mm, **Class 1**, Samples = 3	2181 2211	1828 **1837** 1849	11 **0.58**	2215 2245	1825 **1839** 1859	18 **0.97**	1827 **1842** 1861	18 **0.98**
7	C_3H_8/air, φ = 1.49, 20.5 SLM air, v_{cf} = 12.7 cm/s, H = 15 mm, **Class 3**, Samples = 41	2184 2214	1520 **1827** 1920	90 **4.93**	2217 2247	1799 **1849** 1922	26 **1.40**	1800 **1849** 1924	28 **1.49**
8	C_3H_8/air, φ = 1.49, 20.5 SLM air, v_{cf} = 12.7 cm/s, H = 15 mm, **Class 2**, Samples = 26	2186 2216	1810 **1853** 1920	30 **1.60**	2215 2245	1824 **1854** 1922	26 **1.42**	1822 **1853** 1924	27 **1.48**
9	C_3H_8/air, φ = 1.49, 20.5 SLM air, v_{cf} = 12.7 cm/s, H = 15 mm, **Class 1**, Samples = 17	2185 2215	1810 **1838** 1892	19 **1.02**	2216 2246	1824 **1839** 1861	11 **0.57**	1822 **1837** 1860	11 **0.62**
10	C_3H_8/air, φ = 1.43, 60 SLM air, v_{cf} = 37.1 cm/s, H = 20 mm, **Class 2**, Samples = 11	2170 2200	1909 **1940** 1974	22 **1.12**	2201 2231	1915 **1935** 1960	14 **0.74**	1917 **1932** 1959	14 **0.73**
11	C_3H_8/air, φ = 1.5, v_{cf} = 6.2 cm/s, H = 5 mm, **Class 2**, Samples = 4	2173 2203	1544 **1605** 1754	100 **6.21**	2213 2243	1727 **1742** 1751	11 **0.60**	1738 **1747** 1753	7 **0.38**
12	C_2H_4/air, φ = 1.29, v_{cf} = 12.7 cm/s, H = 15 mm, **Class 3**, Samples = 6	2169 2199	1536 **1647** 1747	104 **6.29**	2193 2223	1617 **1685** 1731	51 **3.04**	1698 **1715** 1728	14 **0.80**
13	C_2H_4/air, φ = 1.29, v_{cf} = 12.7 cm/s, H = 15 mm, **Class 1**, Samples = 3	2176 2206	1731 **1741** 1747	9 **0.49**	2197 2227	1727 **1729** 1731	2 **0.13**	1723 **1726** 1728	3 **0.15**
14	C_2H_4/air, φ = 2.5, v_{cf} = 5.84 cm/s, H = 8.5 mm, **Class 2**, Samples = 3	2242 2272	1629 **1644** 1657	14 **0.87**	-	-	-	1622 **1639** 1655	16 **1.00**
15	C_2H_4/air, φ = 2.34, v_{cf} = 6.76 cm/s, H = 15 mm, **Class 1**, Samples = 3	2211 2241	1569 **1569** 1570	0 **0.02**	2260 2290	1554 **1559** 1563	5 **0.29**	1575 **1581** 1584	5 **0.31**
16	C_2H_4/air, φ = 2.34, v_{cf} = 6.76 cm/s, H = 7.5 mm, **Class 3**, Samples = 3	2180 2210	1294 **1430** 1644	187 **13.09**	2252 2282	1621 **1648** 1691	38 **2.28**	1639 **1662** 1688	25 **1.48**

Table 2. Error analysis of the temperatures measured in different flames and found with different interpretation strategies. Data sets have been categorized in class 1, 2 and 3 referring to the quality of the experimental setup. Class 1 data sets only contain measurements performed with nearly optimal experimental conditions. Class 3 data sets contain all measurements performed on a particular flame even with very poor experimental conditions. Class 2 data sets contain all measurements except those made under the worst experimental conditions.

A final determination of the method accuracy is not possible, since the actual flame temperature is not known. Thus, the best possible accuracy determination that can be made is by comparing with results obtained from other methods.

To make measured flame temperatures comparable, the flame conditions must be identical. This is a requirement because the flame temperature depends on the heat loss to the burner and the surroundings. Ideally, the measurement methods to be compared should be applied on the same flame. Since this was not an opportunity, we had to compare with results made in other laboratories and described in the literature.

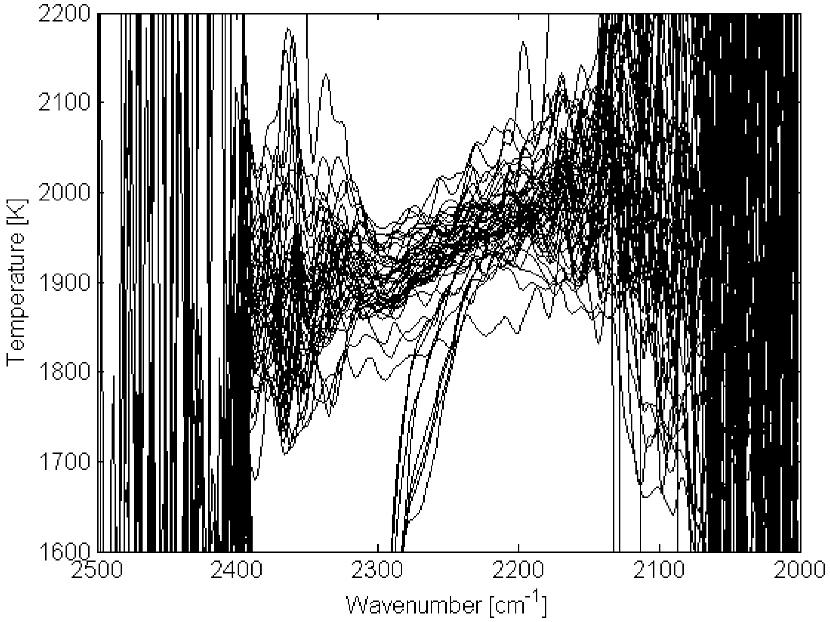

Figure 24. Collection of the measured temperature spectra of the case 1 data set in Table 2.

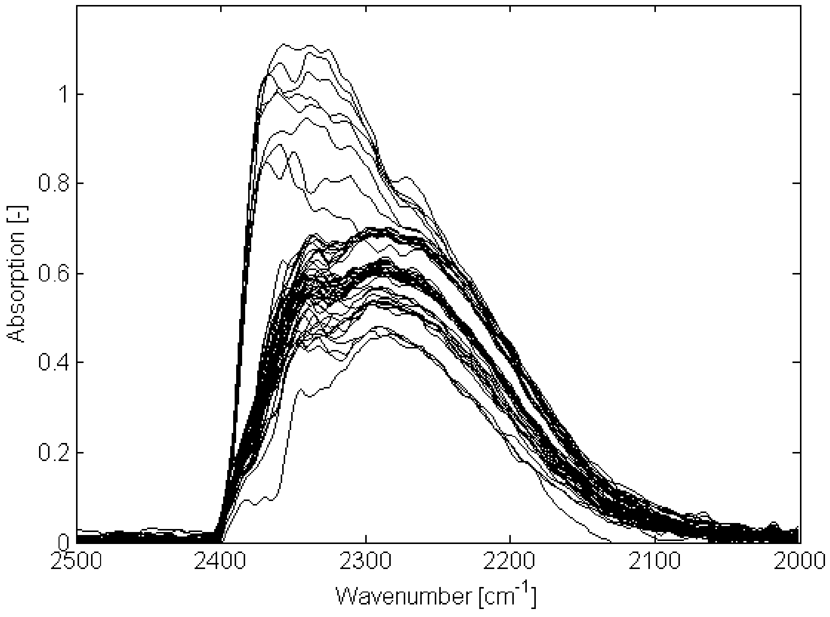

Figure 25. Collection of the measured absorption spectra of the case 1 data set in Table 2.

An accuracy evaluation for many different flames was desirable to discover any limitations in the method. Since temperature measurements on flat flames, particularly sooting flat flames, in the literature are scarse, we had to compare with measurements of flames at slightly different conditions. Especially the stabilization method represents a deviation between our experiments and others. Helium stabilization was used in our measurements while different variations of stabilizer plates were used in some of the others measurements. It was preferable to use helium stabilization during the accuracy evaluation because then the precision was good enough to rely on one single measurement for each flame condition. A previous investigation with our method showed no temperature difference between a helium stabilized stoichiometric flame and the same but unstable flame surrounded by N_2 or air. In the flame periphery this is most likely not the case but the temperature measurement seems to capture the core temperature as desired. Thus, we believe the flame temperature of helium stabilized and unstabilized flames are comparable if it is not measured too far downstream where the horizontal heat losses reach the flame core. An investigation by Zhao [65] with a horizontal probe of 9.5 mm diameter stainless steel tube entered to a flame shows that the upstream temperature only is affected by the probe up to 5 mm away. Thus, we also believe the flame temperature of helium stabilized and plate stabilized flames are comparable if it is not measured too close to the stabilizer plate.

In a thorough work made by Sutton [53], the flame temperatures were measured at different locations in flat propane/air flames with varied equivalence ratios and flow rates. The burner was the same kind of McKenna burner as the one used in our work. The temperature measurements were performed with Rayleigh scattering of laser light. The method had an impressive precision of 0.2 %. Results obtained from Sutton and results from the IR emission absorption method with identical flame conditions are shown in Figure 26 and Figure 27.

The measurements from our work were made at an early stage in the method development, so the experimental conditions were not optimal but acceptable. The fact that the precision was not too good at that time is revealed by reading the temperature at 20 mm in Figure 27 and compare it with the reading in Figure 26 at φ = 1 and 60 SLM of air. This reveals a difference of 32 K which is not good. But by comparing the measurements at φ = 1 and 30 SLM air, φ = 1.5 and 30 SLM air, φ = 1.43 and 60 SLM air in Figure 26 with case 3, 10 and 6 mean values (α = 0.3) in Table 2 the general impression is that the measurements are satisfying.

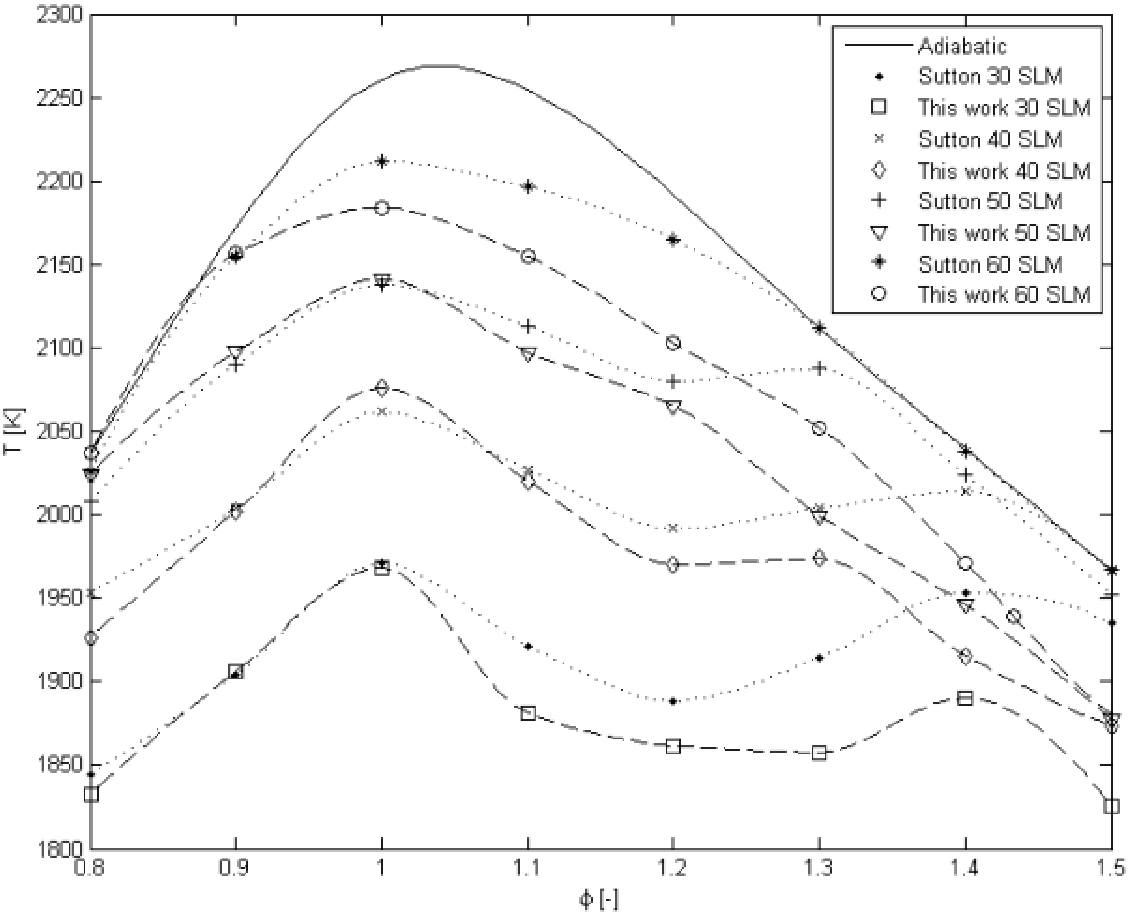

Figure 26. Measured flame temperatures in propane/air flames at 20 mm height with varied equivalence ratios and flow rates. The flow rates in the legends refer to cold flow of air.

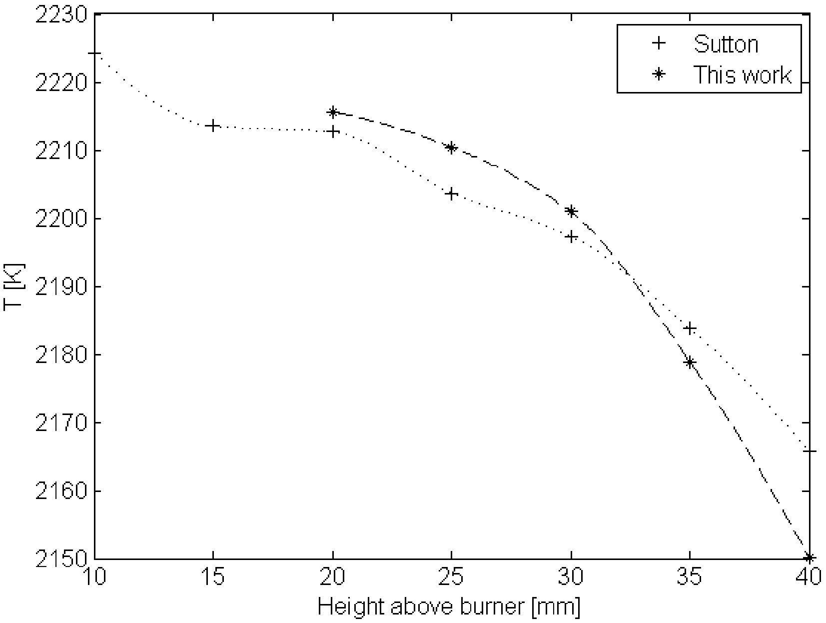

Figure 27. Measured flame temperatures at different heights in a stoichiometric propane/air flame with a flow rate of 60 SLM air.

The results with the IR emission absorption method qualitatively match well with the results from Sutton. Quantitatively they match well for stoichiometric and lean flames, but with increasing equivalence ratios they diverge, with the IR emission absorption method producing the lowest temperature. In order to find a reason for the lower temperatures measured with the IR emission absorption method, a large number of experiments were carried out with equivalence ratios around 1.5 which is seen from case 4, 7 and 10 in Table 2, but no reason was found.

Kaiser [51] also measured the temperatures at different locations in pre-mixed propane/air flames with varying equivalence ratios. Kaiser also used a standard McKenna burner but the temperatures were measured with thermocouples. The correction for radiative losses was validated by repeating some measurements with three different bead diameters, and agreement within +/- 15 K was obtained. Measurements made by Kaiser and measurements made with the IR emission absorption method are shown in Figure 28. There is very good agreement between the two methods. Only at lower flame heights in the rich flame the IR emission absorption method measures lower temperatures than the thermocouple measurements but not to the same extent as in the comparison with the Rayleigh scattering measurements.

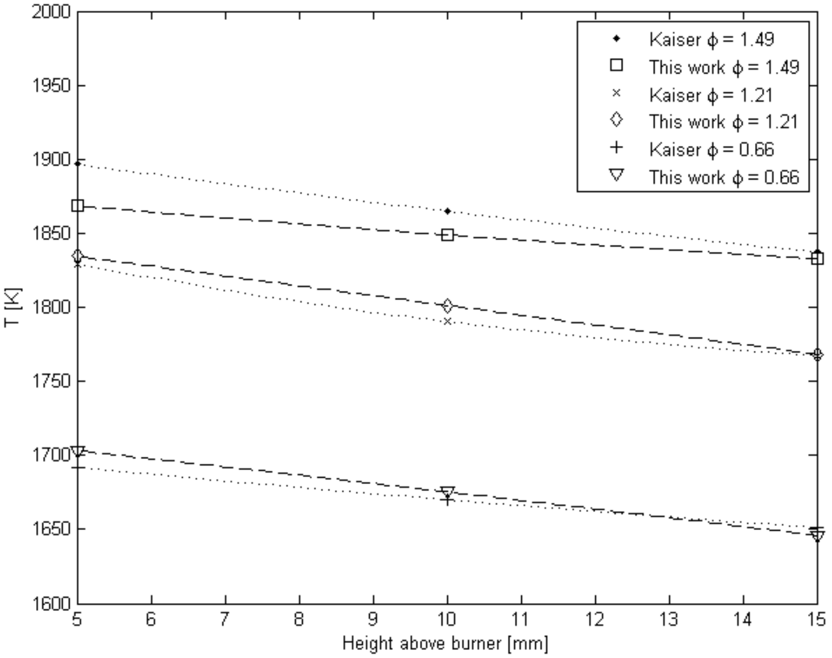

Figure 28. Flame temperatures in pre-mixed propane/air flames measured at different heights with different equivalence ratios. The air flow rate was fixed at 20.5 SLM.

Vestin [54] measured the flame temperature in a pre-mixed ethylene/air flame for a wide range of equivalence ratios at a fixed height of 8.5 mm. The flames were stabilized on a standard McKenna burner and the total flow rate of the cold reactant mixture was kept constant at 10 SLM. The temperatures were measured with dual broadband rotational CARS. The method enables measurement of the temperature in sooting flames as well as non-sooting flames without changing the procedure. Estimated from the error bars in the figure made by Vestin [54], the precision is within +/- 12 K.

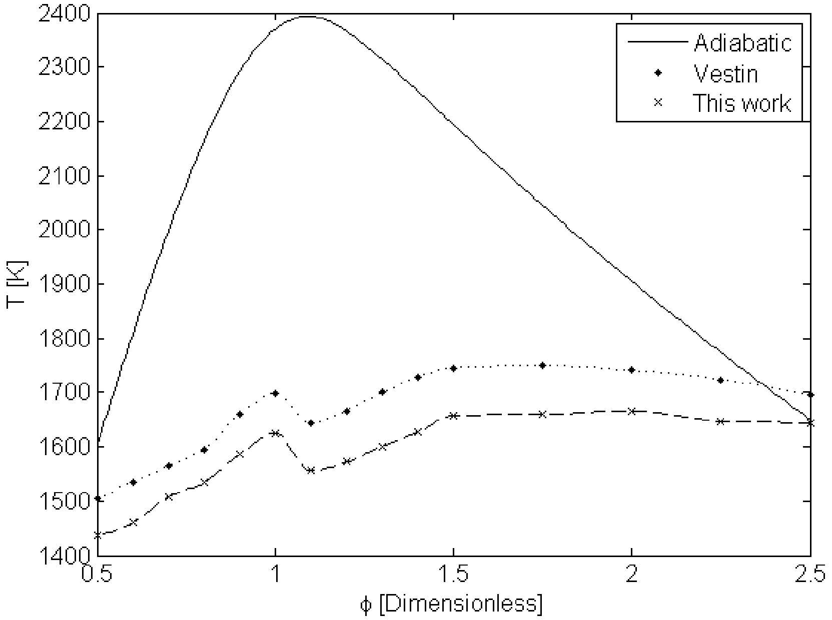

Figure 29. Measured flame temperatures in ethylene/air flames at 8.5 mm height with varied equivalence ratios and fixed total cold flow rate of 10 SLM.

The results from Vestin and the measurements with IR emission absorption of the reproduced flames are shown in Figure 29 together with the adiabatic flame temperatures. Qualitatively the measurements match almost perfectly, but quantitatively they deviate by approximately 80 K with the CARS measurements being the highest. The adiabatic flame temperature is shown together with the measurements to illustrate extent of heat loss to the burner under conditions with flow rates this low. Thus, minor deviations in the burner setup or flow measurements may be responsible for the deviation of the temperatures measured with the two methods. But the adiabatic temperature curve also reveals that the CARS measurement at φ = 2.5 is higher than the adiabatic flame temperature, while IR emission absorption measurement is the same as the adiabatic flame temperature. The latter corresponds well to our experiences with flame blowoff as the equivalence ratio is further increased. The flame temperature may be higher than the adiabatic temperature due to departure from equilibrium with endothermic reactions left partially unreacted. But it is difficult to judge how likely this is to occur. Apart from that, it must also be considered that the true flame is never adiabatic. At least the radiative heat loss to the burner will be present, regardless of the reactant velocity out of the burner.

This discussion may be continued when measurements made by Xu [66] are examined in Figure 30. The temperatures in the sooting flame stabilized on a standard McKenna burner were measured with a multi color method, reported to have an uncertainty of 50 K. The temperature at 7.5 mm height is measured by Xu to be 2100 K, where the IR emission absorption method measures 1639 K. The adiabatic flame temperature is only 1729 K and if CO is removed from the product list in the equilibrium calculation, thus leaving all the excess ethylene unreacted, the adiabatic flame temperature reaches 2070 K.

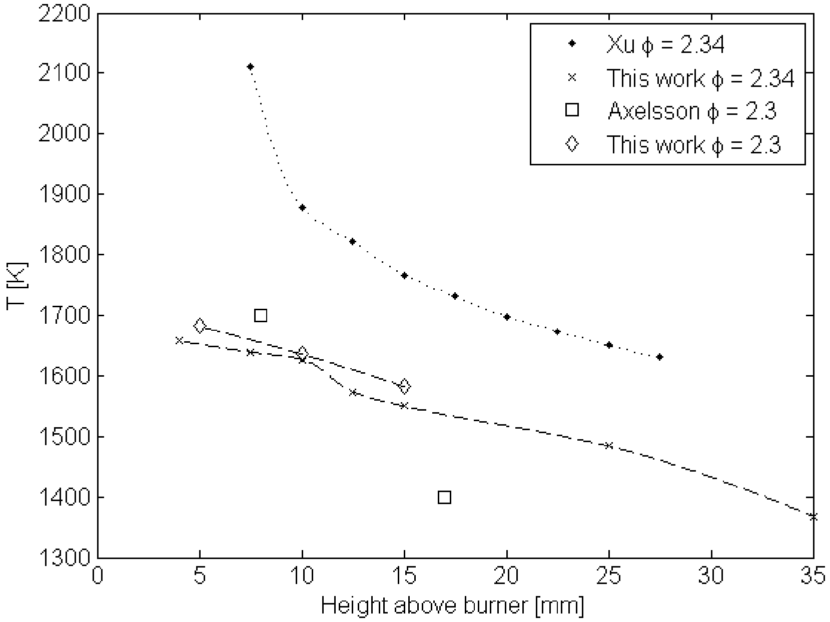

Figure 30. Measured flame temperatures in ethylene/air flames at different heights and fixed equivalence ratios. The total cold flow rate of the φ = 2.34 flame is 11.6 SLM and for the φ = 2.3 flame is 10 SLM.

It seems unlikely that such a deviation from equilibrium may take place at these high temperatures. To further confirm this, measurements made with dual broadband rotational CARS by Axelsson [67] at almost the same flame condition were included in Figure 30, as well as IR emission absorption measurements for at the same flame conditions. The topic of Axelsson's paper [67] was not the temperature measurements and only the endpoint temperatures were reported. A precision of +/- 3 % is reported and a stabilizer plate was located at a height of 21 mm. The latter is likely to be the reason for the low temperature at 17 mm. The temperature at 8 mm is slightly higher than the temperatures obtained with IR emission absorption. Comparing the two measurement series made with IR emission absorption reveals that the φ = 2.34 series was made at an early stage in the method development. The φ = 2.34 measurements should be slightly higher than the φ = 2.3 measurements because of the higher reactant flow rate. Due to the lack of purge tube extensions at heights below 20 mm, these measurements are too low and exhibit scatter. The φ = 2.34 series was made under good experimental conditions.

Measurements with the IR emission absorption method have been compared with thermocouple measurements in a sooting flame (Figure 31) made by Zhao [65]. Qualitatively the measurements agree well, but quantitatively they deviate about 80-150 K with the thermocouple measurements being the lowest.

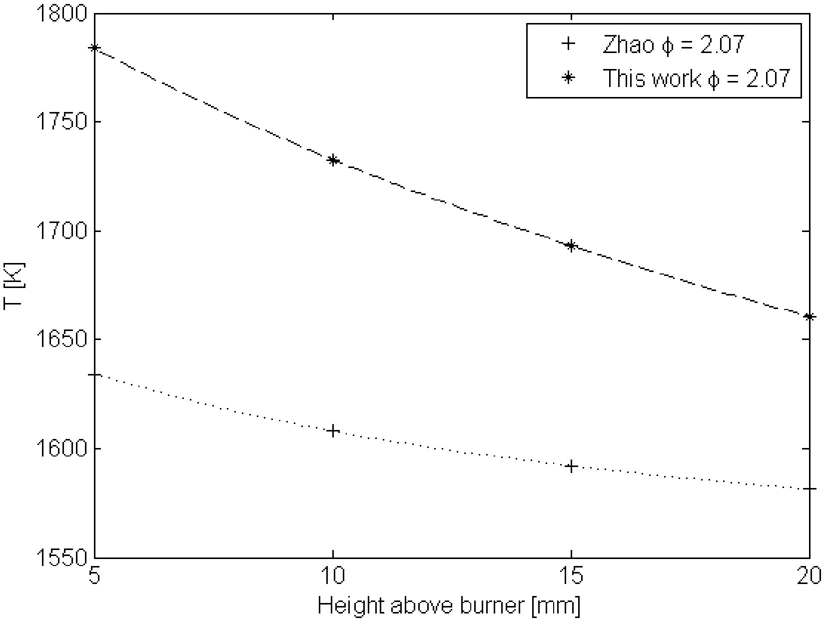

Figure 31. Measured temperatures in a ethylene/air flames at different heights and fixed equivalence ratios. The total cold flow rate of reactants was 14.1 SLM.

Finally, comparison was made with measurements from the Sodium line reversal method made by Minutole [68]. These measurements were made at 6 mm height in ethylene/air flames stabilized on a capillary tube burner with a diameter of 56 mm. The cold flow velocity was 10 cm/s and the equivalence ratio ranged from 1.2 to 2.3. The temperatures were reported to range between 1630 and 1730 K without further specification. To compare the two methods, IR emission absorption measurements were made at φ = 1.23, 1.74 and 2.25 and flame temperatures of 1724, 1830 and 1784 K were obtained respectively. Thus, approximately 100 K lower temperatures were obtained with the sodium line reversal method.

Soot concentration measurements in the flame

A well documented [69, 70] and simple light absorption method was used to measure the soot concentration in terms of soot volume fraction v_f. The experimental setup used for the temperature measurements was modified to measure absorption of visible light by using an Ocean Optics USB4000 VIS-NIR spectrometer, green LED light source, quartz lenses and quartz windows as shown in Figure 32.

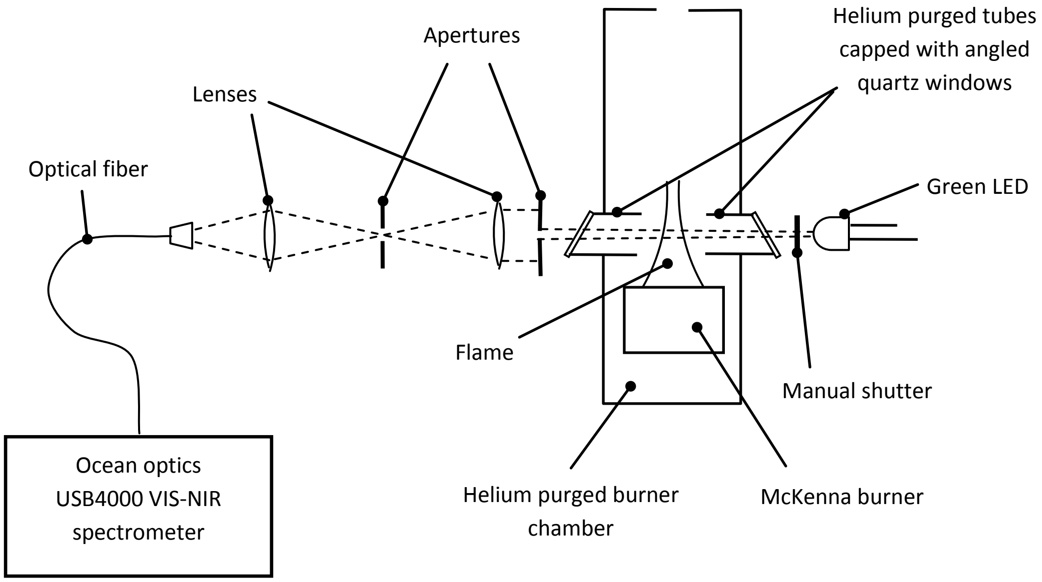

Figure 32. Sketch of the experimental setup and the optical path used for measuring the soot volume

The measuring procedure was basically the same as for the temperature measurements. The derived

transmittance of light in the range of 500-520 nm was used in eq. 8.

$$\frac{I_\lambda}{I_{\lambda 0}} = e_\lambda^{-\frac{K_\lambda(1+\rho_s)f_v L}{\lambda}} \tag{8}$$

With soot particles in the Rayleigh size limit ($\pi D_s/\lambda < 0.3$) scattering to absorption ratio ρ_s may be assumed to be zero. With λ = 500 nm the Rayleigh size limit is D_s = 47 nm. The premature soot in relevant rich premixed flat flames typically contains particles in the range 2-70 nm but with mean diameters smaller than 30 nm [65]. Choi [70] tested the assumption of neglecting scattering by measuring ρ_s in a very rich premixed ethylene flame and found it to be less than 0.08 at λ = 488 nm.

The absorption coefficient K_λ was calculated with eq. 9 and with the complex refraction index $m = 1.57 - 0.56i$ [93].

$$K_\lambda = \frac{36\pi \mathrm{Re}(m_\lambda)\mathrm{Im}(m_\lambda)}{(\mathrm{Re}(m_\lambda)^2 + \mathrm{Im}(m_\lambda)^2 + 2)^2 + 4\mathrm{Re}(m_\lambda)^2\mathrm{Im}(m_\lambda)^2} \qquad 9$$

The absorption path length L was chosen as the distance between the helium purge tubes.

Premixed flat flame modeling

This section describes a methodic development of a CFD model of the premixed flat flame from the experimental work.

Intentionally this work was mainly meant to be focused on the combustion and soot formation processes. But early it became evident that the thermal flow caused by the combustion is a challenge to model in itself. Thus a large part of this section just deals with thermal flow model, but it was necessary to have this validated before the work could continue with the combusting flow model.

Thermal flow model

The thermal flow from a flame is particularly challenging to model because of the widely varied temperatures and gas composition. This causes processes to be important that may be ignored in isothermal and fixed composition models. These processes are:

- Buoyancy effects due to density variations causing the hot gases to rise.
- Conductive, convective and radiative heat transfer.
- Diffusion of gas species due to gradients in the gas composition.
- The conductive, diffusive and viscous properties of gases are temperature dependent and may vary as much as an order of magnitude within the temperature range of flames.
- The high temperature and composition of flame products causes reactions to occur which are not directly related to the combustion reactions. This study shows that the water gas shift reaction has an influence on the thermal flow.

The experiments performed in this work are well suited for validating a thermal flow model because the effects of the thermal flow and the combustion may be separated in both the steady and unsteady case. The fixed position and the uniformity of the flame front just above the flame holder make it reasonable to assume that hot combustion products are coming directly out of the flame holder.

The φ = 2.14 flame from the stability analysis in the experimental work was used as test case for thermal flow modeling. Thus the cold flow out the burner is 3 SLM of C_2H_4 and 20 SLM of air. By assuming chemical equilibrium at the adiabatic flame temperature the hot product gas velocity is 1 m/s at 1829 K with a molar composition of $x_{CO2} = 0.021$, $x_{CO} = 0.194$, $x_{H2O} = 0.065$, $x_{H2} = 0.151$ and the rest is N_2. In the eksperimental work the flame temperature has been measured with the IR emission absorption method to be about 1780 K at 10 mm height above the burner. This confirms that the adiabatic equilibrium assumption is reasonable.

To omit soot radiation a stoichiometric flame (φ = 1) was also used for validation of the radiation models. The cold flow of the experimental flame was 1.4 SLM of C_2H_4 and 20 SLM of air. The flame temperature at this condition was calculated be 1931 K with Chemkin using the USC mechanism [84]. At 1931 K the hot product velocity is 0.81 m/s and the equilibrium composition is x_{CO2} = 0.128, x_{CO} = 0.002, x_{H2O} = 0.13, x_{H2} = 0 and the rest is N_2.

Description of the CFD model

All CFD modeling in this study was made in ANSYS CFX. This software package offers a user friendly integration of geometry, mesh and CFD modeling with all the options needed for thermal and combusting flow modeling. A license was available to perform parallel computing with 8 processors on a cluster to reduce the computation time.

Due to axis-symmetry of the flame it is only necessary to model a cut of the flame chamber (Figure 33). A model of the full flame chamber geometry was made. This requires many mesh points which is maybe not necessary but it facilitates the use of correct boundary conditions. The measures of the geometry are shown in Figure 35 as well as locations of the boundary conditions.

A cut of 4˚ for the geometry model was found appropriate. That choice enables the use of a two dimensional mesh option in CFX with a reasonable mesh quality as result. The influence of different mesh sizes and distributions was investigated on a transient laminar model of the unstable flame. The flame shape and the oscillation frequency was just weakly sensitive to the mesh, and a conservative choice of 38000 nodes was made for the following model development (Figure 34). It would be appropriate to carry out a more methodic mesh sensitivity analysis in the future when the entire model including combustion has been determined. Inflation of five hexahedron layers with a total thickness of 0.6 mm was used on the wall boundaries. The mesh was refined at the large temperature gradient between the hot flame products and the surrounding gas as shown in Figure 34.

The flames investigated in this study are generally considered to be laminar. High turbulence with small eddies, produces brush shaped flames. None of the flames observed in the experimental work have shown presence of high turbulence. But large scale structures are certainly present outside the flame, since they produce the instability that occurs when helium stabilization is not applied.

It was not obvious weather a laminar model would be able to describe these large scale structures or if some turbulence model had to be applied. The laminar model is able describe such structures if just the mesh size is small enough compared to the structure size. A k-ε model is able to account for small eddies with a coarse mesh but has a tendency to dissipate away the large eddies and potentially also large scale structures.

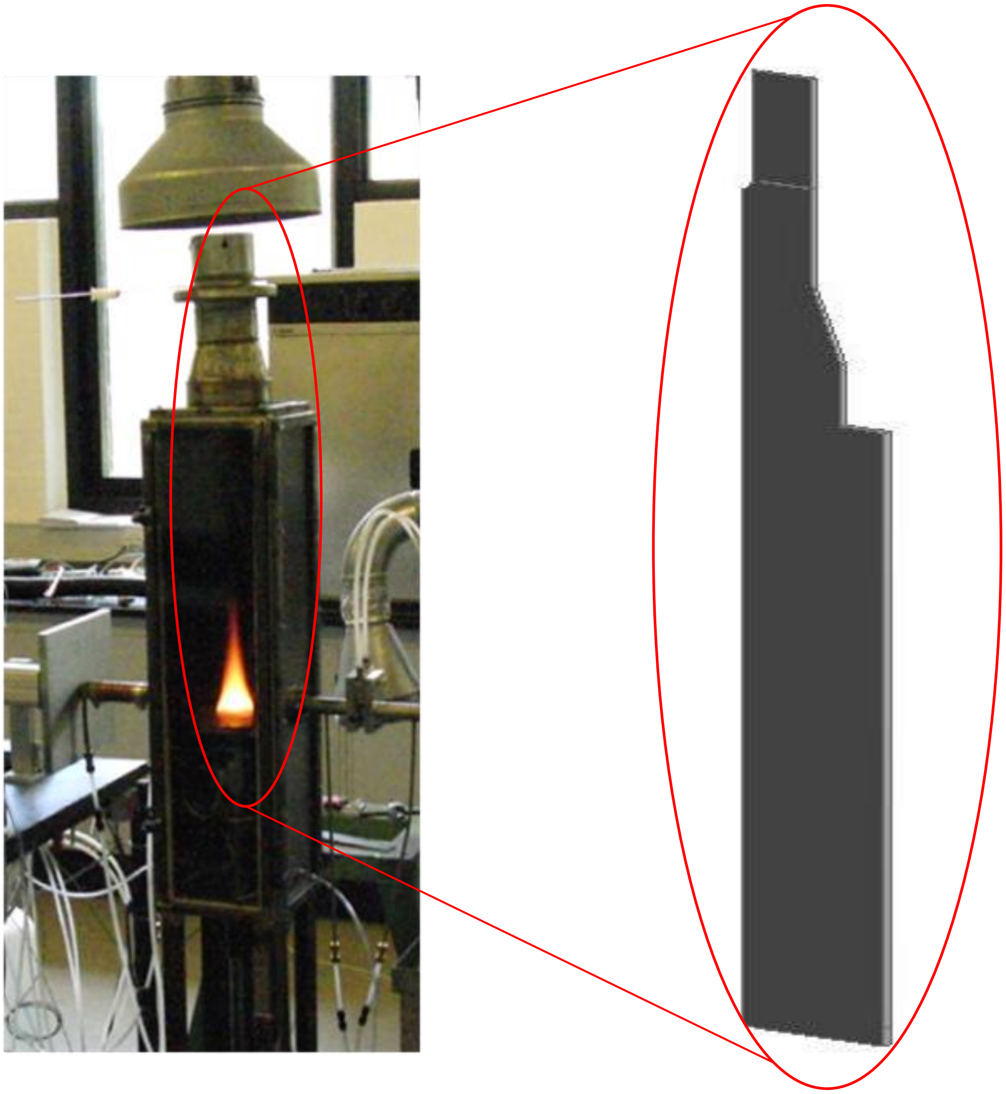

Figure 33. An illustration of the flame chamber and the model of fluid domain.

Three turbulence models were tried on a transient model of the unstable flame; Large Eddy Simulation (LES), Reynolds Stress Model (RSM) and k-ε model. The LES method was the obvious choice to describe the intermediate sized eddies that was potentially present around the flames. But it is also computational demanding and the model would have to 3-dimensional to take advantage of LES method. The RSM method is better to describe the larger sized eddies than the k-ε model, but it is more robust and computational affordable than LES. Results obtained with RSM, k-ε and the laminar model were almost identical but the computational cost of using RSM and k-ε was much higher than the laminar model.

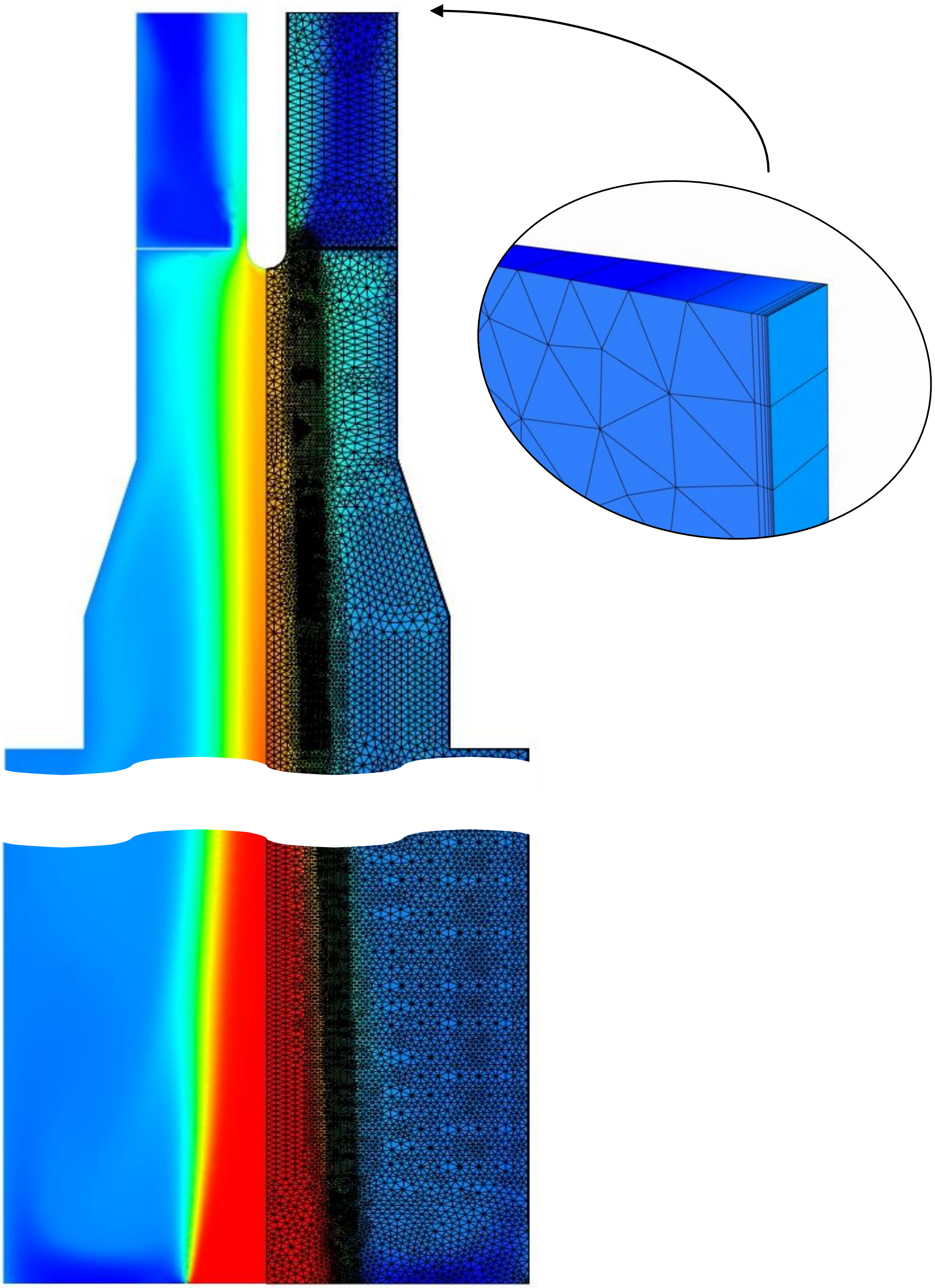

Figure 34. Illustration of the mesh used in the development of the thermal flow model.

The fact that the transient flame computation was insensitive to the use of turbulence models and to the use of a finer mesh, suggests that the large scale structures are resolved adequately by the mesh and the laminar model. Consequently, the laminar model was used for all the following investigations.

The names of the applied boundary conditions (BC) may be found in Figure 35 and the general settings will be described in the following.

Burner BC:

φ = 2.14: An inflow of gas with 1 m/s in the normal direction. The temperature of the gas was 1829 K and the molar composition was x_{CO2} = 0.021, x_{CO} = 0.194, x_{H2O} = 0.065, x_{H2} = 0.151 and the rest N_2.

φ = 1: An inflow of gas with 0.81 m/s in the normal direction. The temperature of the gas was 1931 K and the molar composition was x_{CO2} = 0.128, x_{CO} = 0.002, x_{H2O} = 0.13, x_{H2} = 0 and the rest is N_2.

Co-flow BC: For the modeling of helium stabilized flames an inflow of 0.048 m/s in the normal direction was applied. The gas was pure helium at 300 K. For unstable flames no co-flow was used and a no slip wall at 450 K was applied as boundary condition.

Opening BC: A static absolute pressure of 1 atm was applied. The outside gas was air at 300 K.

Cut BC: Rotational periodicity was used as interface between the two cuts. This allows the gas to rotate around the center axis of the flame.

Wall BC: No slip wall at 450 K was applied. That choice of temperature was experimentally found to be appropriate.

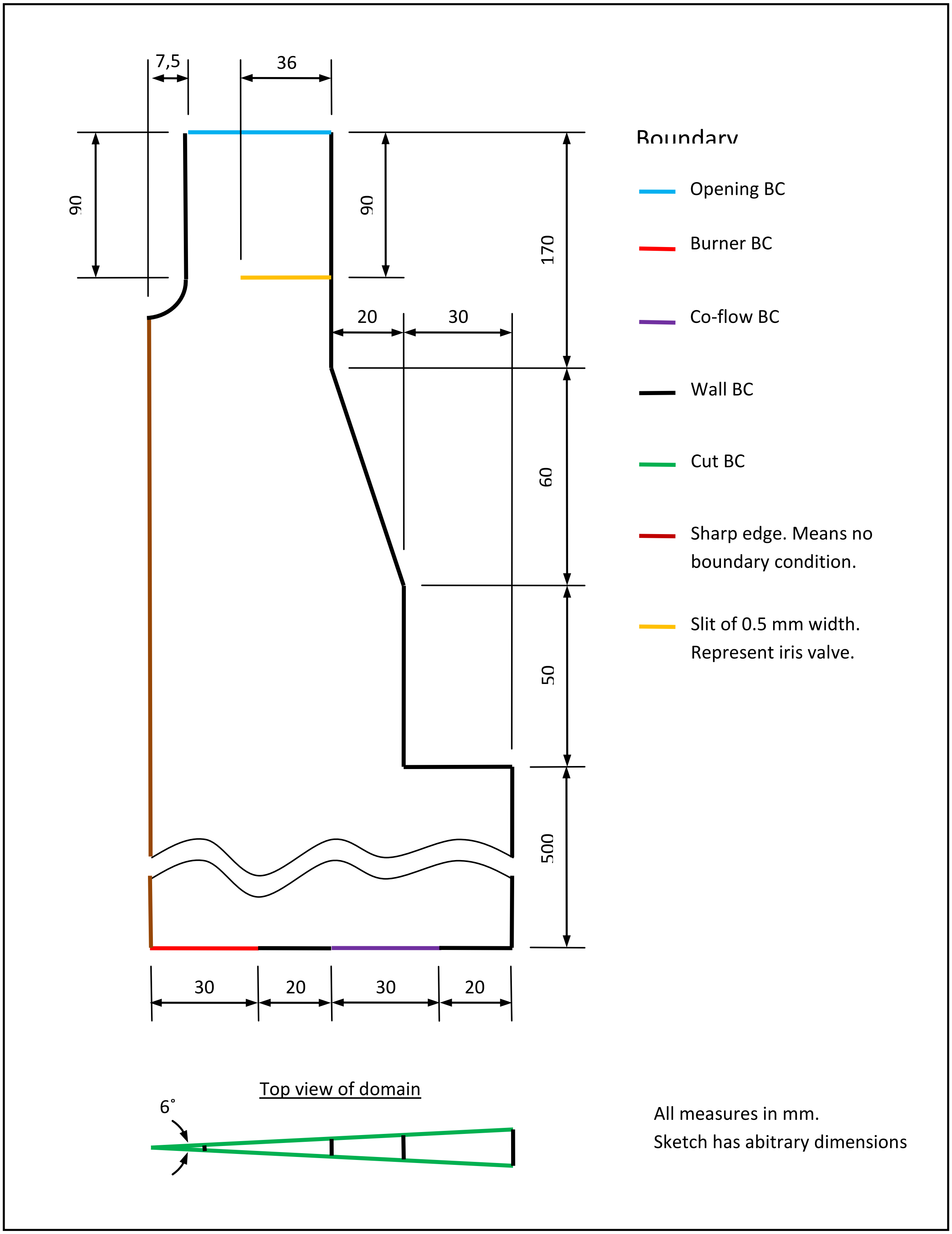

Figure 35. Sketch of the modeled flow domain with illustrations of the boundary conditions (BC).

In the solver settings for the steady model a high resolution advections scheme was used. A fixed number of 1000 iterations were used and the pseudo time step was set adaptively by CFX. The CPU time for a steady run was typically around 8 hours.

In the solver settings for the transient model the high resolution advection scheme for the flow model and a second order backward Euler transient scheme for the time stepping was used. Three coefficient iterations were used for each time step. Higher numbers of coefficient iterations were tried but the results were unchanged. A fixed time step of 1 ms was used resulting in a RMS Courant number around 1.6. This means that the gas in average moves 1.6 times the cell size of the mesh during a time step. A Courant number of 1.6 is quite high but lower time steps did not influence the results. The simulation time for the transient runs was 2 seconds. A previous investigation showed that modeled flame oscillation became systematic after about 1 second and 0.5 second of data was needed to perform a frequency analysis. Thus a simulation time of 2 seconds was a conservative choice. The CPU time for the transient runs was typically around 48 hours.

The initial condition for the steady runs was unmoving helium at 450 K, and for the transient runs it was the result from a steady run with similar setup as the succeeding transient run.

Improvements of the thermal flow CFD model

In this section the stepwise improvements of the thermal flow model is described. Each improvement step has been given a version number with Version 1 being the first version. Both transient results of a flame without helium stabilization and steady runs of a helium stabilized flame are evaluated.

The predicted flame core temperatures and soot volume fractions of the stable flame are compared with measurements. The measurements are made according to the description in the experimental sections. Measurements and some model predictions were made for a non-sooting (φ = 1) as well as sooting (φ = 2.15) flame to enable investigation the influence of radiation by soot.

A visual evaluation of the 2-dimensional flame shape of the sooting flame (ϕ = 2.15) was found to be a simple and sufficient evaluation method at the present development stage. The high equivalence ratio of 2.15 causes soot to be present in the post flame region. Soot is a black body emitter and the light spectrum emitted from soot is almost only dependent on the temperature. The intensity of the spectrum is dependent on the soot concentration and the flame thickness. The observed color of a black body at a certain temperature is defined as the color temperature. Figure 36 shows a flame picture and a standard of the color temperatures.

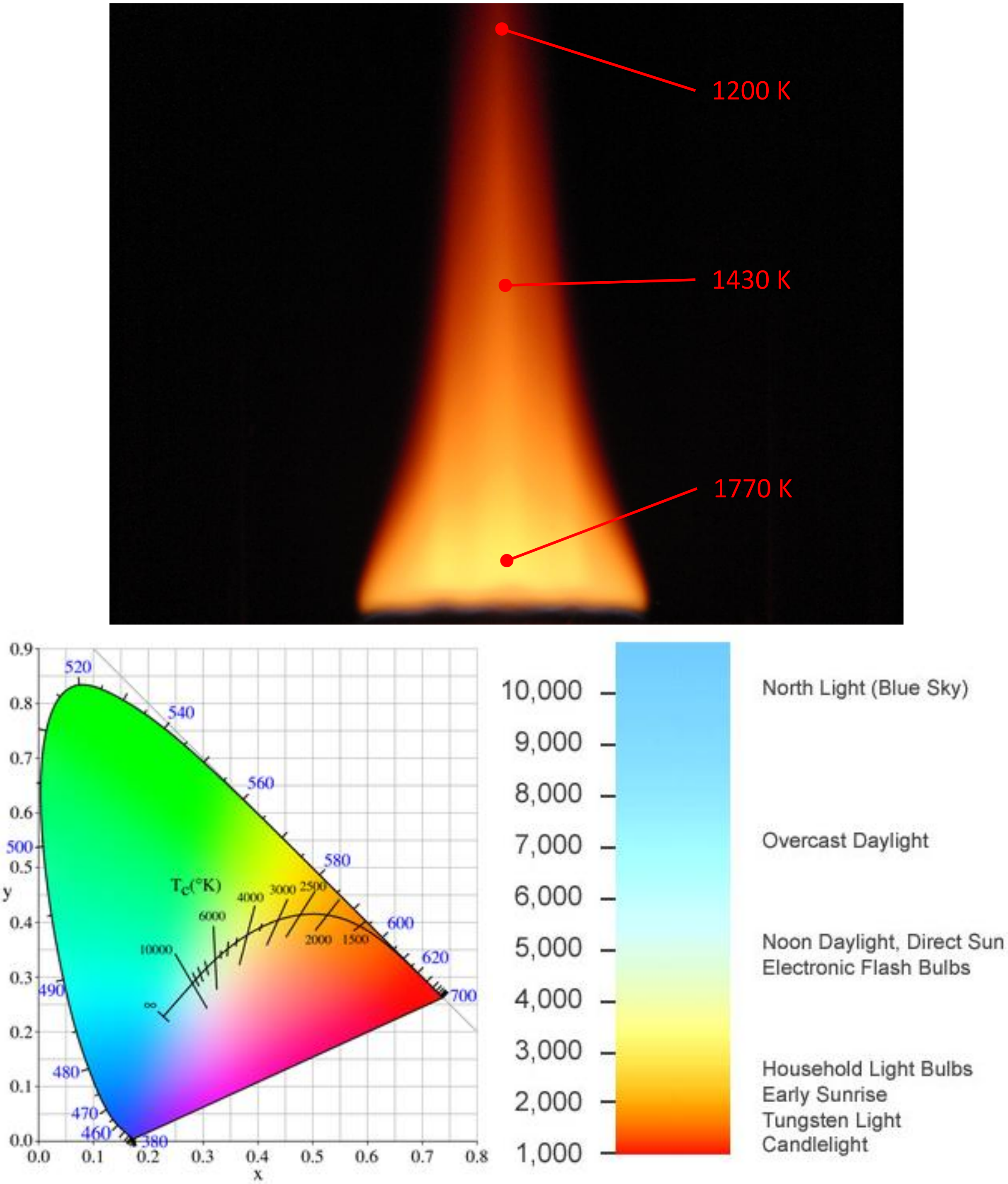

Figure 36. Top: Photo of the Helium stabilized C_2H_4/air flame at ϕ = 2.15. The photo is taken with a camera sensibility just below saturation to avoid distortion of the colors. Some measured temperatures are also shown. Bottom: Two illustrations of color temperature. The CIE 1960 color map on the left is a color standard by the International Commission on Illumination that shows the color temperature interpretation by the eye.

According to the standard is the color at temperature around 2000 K orange and it becomes redder at lower temperatures. At 1000 K the color is deep red and below 1000 K the blackbody emission is not detectable by the eye. Based on this the visible soot seem to have temperatures ranging between 1200 and 1800 which corresponds well with the measurements shown on the flame picture. In the periphery of the visible soot there must be a rather steep temperature/soot concentration descent to explain that visibility suddenly disappears.

Visual observations of these temperature gradients have shown to be a reasonable measure for evaluating the thermal flow model. The temperature plots of both the unstable and the stable flame are collected in appendix A together with pictures of the real flame at identical conditions. The figure captions specify the oscillation frequency of the flame instability for the transient results. The frequency was obtained with fast Fourier transformation in the same way as described in the "Establishment of a stable pre-mixed flat flame" section.

In the following the stepwise progress of the method development will be explained. For each version number the modification of the model, the motivation for the modification and the result of it will be explained

Version 1: This version represents the basic setting of the model as described in the previous section. The default gas property values from the reaction gas library in CFX were used. The default thermal conductivities and the dynamic viscosities of the gases were used. They are independent of temperature and are shown in Table 3. The specific heat, enthalpy and entropy were calculated with NASA SP-273 correlations [71, 72]. No radiation or reaction models were used for this basic setting.

	Thermal conductivity k [W m^{-1} K^{-1}]	Dynamic viscosity μ [W m^{-1} s^{-1}]
CO	0.0251	$16.6 \cdot 10^{-6}$
CO_2	0.0145	$14.9 \cdot 10^{-6}$
H_2	0.1809	$8.8 \cdot 10^{-6}$
H_2O	0.0193	$9.4 \cdot 10^{-6}$
He	0.1415	$18.6 \cdot 10^{-6}$
N_2	0.0259	$17.7 \cdot 10^{-6}$

Table 3. Default constant gas properties in CFX. The CFX documentation refers to [72].

Results from the transient run of the unstable flame are shown in Figure 63 (app A). The model does predict the systematic instability but the oscillation frequency is 9.78 Hz which is too high compared to the measured 6.98 Hz. The shape of the flame also deviates from the physical flame. From the model results it is clear that a vortex is responsible for the flame instability. The vortex develops at the base of the flame. As it grows it also moves up along the flame until it escapes and leave room for a new vortex to be formed. This is repeated over and over again very systematically. But in the case of the model the vortex develops at an earlier stage very close to the burner. This causes the formed vortex to be smaller and faster rotating. It drags hot combustion products around it, resulting in the characteristic wave shape on the flame boundary to be evident at a lower height then it is in reality.

Transient runs of the helium stabilized flame converge to a stable solution. This fully justifies the use of steady state runs for the helium stabilized flame.

The model result from the steady state run for the helium stabilized flame is shown in Figure 51 (app A). The flame products are rising vertically without any heat loss. The flame shape formed by the steep temperature gradients is almost a cylinder instead of a cone, and does not look like the real flame at all.

The lacking heat loss is also evident in Figure 49 (app A) showing the measured and the predicted temperature of the flame core. Hardly any heat loss is predicted by the Version 1 model.

Version 2: Motivated by the low heat transfer in the results of the stabilized flame with the Version 1 model, attention was paid to the constant thermal conductivity. CFX offers the option to use a temperature dependent thermal conductivity by use of the Sutherland correlation. This correlation is derived from gas kinetic theory and is valid within 2-4 % percent for pure gases [73]. To determine the thermal conductivity for gas mixtures the only optional mixing rule in CFX is the ideal gas mixing rule. It is known to be deficient for mixtures of gases with very different properties as in this case. But it is certainly better to use the Sutherland correlations than constant conductivities together with the ideal gas mixing rule.

The Sutherland correlation for the thermal conductivity is shown in equation 10 where *k* is the thermal conductivity and *S* the Southerland constant.

$$\frac{k}{k_0} = \left(\frac{T}{T_0}\right)^{\frac{3}{2}} \frac{T_0 + S}{T + S} \tag{10}$$

The parameters for the relevant gases are shown in Table 4. The thermal conductivity calculated at 1800 K is also shown to enable comparison with the reference conductivity k_0 at valid at the reference temperature T_0. The reference thermal conductivity is almost identical with the default value in CFX shown in Table 3. The comparison shows that for CO_2 and H_2O the thermal conductivity increases tenfold with the temperature increase, and 3-4 times for the other gases.

	Reference thermal conductivity k_0 [W m^{-1} K^{-1}]	Sutherlands constant S [K]	Ref. temperature T_0 [K]	Thermal conductivity at 1800 K k_{1800} [W m^{-1} K^{-1}]
CO	0.0232	180	273	0.0899
CO_2	0.0146	1800	273	0.1423
H_2	0.168	120	273	0.5822
H_2O (gas)	0.0181	2200	300	0.1895
He	0.151	58.65	273	0.4562
N_2	0.0242	150	273	0.0889

Table 4. Parameters for Sutherland correlations of thermal conductivities. The parameters for He was fitted to experimental data ranging from 100 to 600 K [73]. The other parameters are from White [73]. The thermal conductivity at 1800 K calculated with the correlation is also shown.

The effect of increased thermal conductivity is evident in the results from the stabilized flame model (Figure 51 app A). The flame is taking a cone shape and the temperature is more gradually distributed across the flame borders. Also the temperature of the flame core is beginning to decline at large flame heights but it is still far from the measured results (Figure 49 app A).

The modeling result of the unstable flame is almost insensitive to the more correct computation of the thermal conductivity (Figure 64 app A) both with regard to flame shape and oscillation frequency. This was unexpected because the buoyancy driven shear layer instability occurs from the density gradients in the shear layer resulting from the temperature gradients. Since the temperature gradients are less steep with the higher thermal conductivity an effect on the instability was expected. The only effect is that the early formed wave on the flame boundary is slightly more rounded.

Version 3: The development of smaller and faster rotating vortices in the model of the unstable flame motivated to point attention to the viscous properties of the model gases. The option for Sutherland correlated temperature dependency was available in CFX for dynamic viscosities too. The correlation equation for the dynamic viscosity μ is the same as for thermal conductivity (equation 11). Parameters for the relevant gases are shown in Table 5. The dynamic viscosity at 1800 K is 3-8 times the dynamic viscosity at the reference temperature.

$$\frac{\mu}{\mu_0} = \left(\frac{T}{T_0}\right)^{\frac{3}{2}} \frac{T_0 + S}{T + S} \qquad 11$$

The predicted shape of the unstable flame (Figure 65 app A) as well as the oscillation frequency was almost insensible to the temperature dependence of the dynamic viscosity.

The model result of the stabilized flame (Figure 52 app A) as well as core temperature predictions (Figure 49 app A) show that heat transfer is reduced with the increased dynamic viscosity. This is in accordance with fundamental heat transfer theory. With increased viscosity the velocity boundary layer thickness is also increased and the convective heat transport is reduced. The Prandtl number *Pr* is used to describe the heat transport property of a fluid.

	Reference dynamic viscosity μ_0 [N s m^{-2}]	Sutherlands constant S [K]	Ref. temperature T_0 [K]	Dynamic viscosity at 1800 K μ_{1800} [N s m^{-2}]
CO	$1.657\cdot10^{-5}$	136	273	$5.927\cdot10^{-5}$
CO_2	$1.37\cdot10^{-5}$	222	273	$5.678\cdot10^{-5}$
H_2	$8.411\cdot10^{-6}$	97	273	$2.777\cdot10^{-5}$
H_2O (gas)	$1.12\cdot10^{-5}$	1064	350	$8.852\cdot10^{-5}$
He	$1.87\cdot10^{-5}$	79.4	273	$5.936\cdot10^{-5}$
N_2	$1.663\cdot10^{-5}$	107	273	$5.610\cdot10^{-5}$

Table 5. Parameters for Sutherland correlations of the viscosity from White [73]. The viscosity at 1800 K calculated with the correlation is also shown.

$$Pr = \frac{\mu\, C_p}{k} \qquad 12$$

In general a low Prandtl number of a fluid indicates that conductive heat transfer dominates over the convective heat transfer and opposite for high Prandtl numbers [73]. In the present case the Prandtl number was increased but the heat conductive properties unchanged, thus the total heat transfer was reduced.

Version 4: In the case of the stabilized flame, large concentration gradients are present in the fluid domain, and He and H_2 are highly diffusive gases compared to the other gases. Therefore the default transport model based on unity Schmidt number and thus a diffusion coefficient equivalent to the kinematic viscosity of the bulk mixture was suspected to be insufficient in the present case.

The correct way to treat the mass diffusion of different gas species is to apply temperature dependent binary diffusion coefficients for all combinations of gas pairs. In CFX this is not an option and only a single diffusion coefficient may be used for each gas.

Due to these limitations a simplified approach was used. One of the gases always has to be constrained in CFX, which means that no diffusion coefficient or concentration specifications can be applied for that particular gas. This enables CFX to maintain mass balance by adjusting the concentration of the constrained gas. Nitrogen is a natural and often used choice to use as the constrained gas. Due to the constraintness and in general high concentration of N_2 it was also found to be a good choice to use as diffusion reference. Furthermore, N_2 is often used as one of the gases in the binary system when diffusivities have been found experimentally, which makes it easier to find valid binary diffusion coefficients. So the approach was to use binary diffusion coefficient for N_2 with all the other gases (Table 6). CFX has no option for temperature dependent diffusion coefficients D, but a user defined expression may be entered. The power law (equation 13) is a simple but approximate description of the temperature dependence which is often used [75]. Table 6 shows the binary diffusion coefficients and kinematic viscosities at 373.15 and 1800 K found with the described methods. It shows that the Schmidt number equal one or $D = \nu$ actually is a reasonable assumption. They never deviate with more than a factor of two. But the treatment of diffusion for each gas individually, compared to the bulk mixture diffusivity used in previous versions, may still have an effect on the results.

$$\frac{D}{D_0} = \left(\frac{T}{T_0}\right)^{\frac{3}{2}} \tag{13}$$

Equimolar mixture	Binary diffusion coefficient at T_0 = 373.15 K D_0 [m^{-2} s^{-1}]	Kinematic viscosity at 373.15 K ν [m^{-2} s^{-1}]	Binary diffusion coefficient at 1800 K D [m^{-2} s^{-1}]	Kinematic viscosity at 1800 K ν [m^{-2} s^{-1}]
CO -N_2	$3.36\cdot10^{-5}$	$2.33\cdot10^{-5}$	$3.56\cdot10^{-4}$	$3.13\cdot10^{-4}$
CO_2- N_2	$2.53\cdot10^{-5}$	$1.27\cdot10^{-5}$	$2.68\cdot10^{-4}$	$1.91\cdot10^{-4}$
H_2- N_2	$1.162\cdot10^{-4}$	$1.62\cdot10^{-4}$	$1.23\cdot10^{-3}$	$2.05\cdot10^{-3}$
H_2O- N_2	$3.39\cdot10^{-5}$	$2.83\cdot10^{-5}$	$3.59\cdot10^{-4}$	$7.26\cdot10^{-4}$
He- N_2	$1.052\cdot10^{-4}$	$1.78\cdot10^{-4}$	$1.11\cdot10^{-3}$	$2.19\cdot10^{-3}$
O_2 – N_2	$3.07\cdot10^{-5}$	$2.36\cdot10^{-5}$	$3.25\cdot10^{-4}$	$3.19\cdot10^{-4}$

Table 6. Binary diffusion coefficients of the various combustion products in nitrogen at 373.15 K found experimentally [74]. The kinematic viscosities at 373 and 1800 K are calculated with the Southerland correlation. The binary diffusion coefficients at 1800 K are calculated with the power law.

The transient results of the unstable flame (Figure 67 app A) show no effect of the changes to the mass diffusion model. This was expected because the gas concentration is the same everywhere in the fluid domain. If the results were different something would have been wrong with the model.

The results of the helium stabilized flame (Figure 52 app A) show an increase of the thermal boundary layer thickness, but the shape of the flame core is only slightly affected. Figure 49 (app A) shows a slightly higher heat loss from the flame core at large flame heights.

Version 5: The flame predictions from the previous models of the stabilized flame, clearly shows that the heat loss from the flame core is too small.

The oscillation frequencies of the unstable flame were slightly reduced as the thickness of the thermal boundary layer was increased with the model improvements (see captions for Figure 63 to Figure 67 in app A). But the large deviation of the modeled and the measured oscillation frequency indicated that more drastic changes to the model were needed to predict the right frequency.

It is well known that the radiative heat loss from flames is large. Thus extending the model to account for radiative heat transfer was an appropriate step to take at this development stage. For sooting flames the soot radiation is usually considered to dominate over the gas radiation, but since soot was not yet present in this model only a gas radiation model could be employed.

The numerical treatment of radiative heat transfer is different from conductive and convective heat transfer. The physical reason for that is that radiation from one particular source is emitted isotropically as rays. The radiance is reduced as the rays pass through absorbing media but the direction is maintained. This is only true if scattering and refraction may be neglected, which it may in none sooting flames. In sooting flames radiation is scattered by soot which causes complications in many optical measurement techniques. But in modeling of radiative heat transfer the loss of accuracy by neglecting scattering is unimportant compared to the saved computational cost and complexity.

Several numerical methods for solving the radiative transfer exist. A well established method is to use the discrete radiative transfer equation 14 directly by using a limited number of directions and sweep the entire fluid domain in these directions. This method is a good compromise between accuracy and computational cost in combustion models [76] and is available in CFX and thus chosen for this model.

In the discrete radiative transfer equation 14 I is radiance, I_{bb} is black body radiance, λ is wavelength, ε is gas emissivity and k is spatial discretisation step. The first term describes the transmission of the radiance from the previous cell through the present cell. The second term describes the radiation of the present cell.

$$I_{\lambda,k+1} = I_{\lambda,k}(1 - \varepsilon_{g,\lambda,k+1}) + I_{bb,\lambda,k+1}\varepsilon_{g,\lambda,k+1} \quad 14$$

Another challenge in radiation modeling is to describe a simple spectral model. In reality radiative absorption by gases is dependent on wavelength and temperature in a very complicated way. To illustrate this, a spectral radiation model, called HITEMP [77], based on molecular physics was used to calculate the absorption spectra of CO, CO_2 and H_2O at 300 and 1800 K. The obtained absorption spectra are shown in Figure 37 to Figure 39. They show how the absorption magnitude, the shape and the spectral location of the absorption bands are influenced by the temperature. The large changes of the absorption magnitude with temperature are mainly due to the decrease of molecular density, but the changes of shape and spectral location are caused by temperature dependence of the population distribution of the rotational and vibrational energy states and transitions. The combined effect of the temperature change to the absorption spectra and the Planck distributed black body radiation is shown in figures of radiance (Figure 40 to Figure 42). They show that radiance of the cold gases is negligible compared to the hot gases due to the large change of black body radiation magnitude. Thus, the hot gas is a good radiator but a poor absorber compared to the cold gas which absorbs well but radiates very little. This illustrates that radiative heat may well be transferred from hot gas to cold gas. But the transfer is only possible if the emission band of the hot gas is located at the same wave number as the absorption band of the cold gas. To account for that in a CFD model a narrow band spectral model with band widths of around 4 cm^{-1} like HITEMP should be employed to determine the absorption spectra for every cell. Then the discrete transfer equation should be solved for all the spectral bands in all directions separately and coupled together iteratively with the energy conservation equations. This procedure is the most correct way to calculate the radiative heat transfer between gasses but is very computational costly. Thus more approximate models like the wide band models have been developed to reduce the computational cost, but still they are costly. A simpler spectral model called weighted sum of gray gasses (WSGG) has been widely used in CFD modeling of combustion processes. It may be inaccurate as much as 50 % for some cells [76] but it is computationally very efficient. The WSGG model has some foundation in the molecular radiation theory but in general it should be considered as a correlation method based on empirical data. With thorough fitting of the parameters to a specific case the accuracy may be as good as 0.5 % [79].

To investigate the influence of adding a gas radiation model to the present model, the WSGG spectral model together with the discrete heat transfer model in eight directions was found appropriate. A WSGG spectral model was available in the CFX library. This model included CO, CO_2, H_2O, and CH_4 as radiative absorbing gases. It was found very appropriate that CO was included since high concentrations of CO were present in the rich premixed flat flame under investigation. The CH_4 was included in the CFX library model by addition if a gray gas which was only dependent on CH_4 concentration. In the present flame model this additional gray gas was removed since CH_4 was not present. The total emissivity of the gray gasses is calculated with equation 15. The temperature dependence is calculated with equation 16. The model parameters are shown in Table 7. Parameters for products from stoichiometric combustion of methane ($p_{H2O}/p_{CO2} \approx 2$) and higher hydrocarbons ($p_{H2O}/p_{CO2} \approx 1$) are available. Since the flame modeled in this work is very rich, the ratio based on equilibrium is $p_{H2O}/p_{CO2} \approx 3$, thus the parameters for the methane combustion was found to be the best choice.

$$\varepsilon_g = \sum_{i=1}^{4} a_{gi}(T_g)\left[1 - e^{-K_i(p_{H2O}+p_{CO2}+p_{CO})L}\right] \qquad 15$$

$$a_{gi} = b_{1i} + b_{2i}T_g 10^{-5} \qquad 16$$

i	b_{1i} [T^{-1}]	b_{2i} [T^{-1}]	K_i [m^{-1} atm^{-1}]
1	0.364	4.74	0
2	0.266	7.19	0.69
3	0.252	-7.41	7.4
4	0.118	-4.52	80

Table 7. Parameters for the weighted sum of gray gasses model available in the CFX library [79] suitable for combustion products with the concentration ratio p_{H2O}/p_{CO2} = 2.

From the results of the helium stabilized flame model (Figure 54 app A) it is evident that the heat loss from the flame is significantly increased by the radiation model. The tip of the inner hot cone is no longer present and the flame shape is very different from the predictions from the previous versions. The core temperatures of the flame have changed significantly and match the measurements very well for both the stoichiometric and the rich flame (Figure 49 app A). Since the model does not account for radiation from soot it must be considered as incorrect that it predicts the right temperature in the rich flame.

The results of the unstable flame (Figure 68 app A) show that the higher heat loss increases the thickness of the thermal boundary layer. This causes the wave shape formed by the vortex to be more rounded which corresponds better to the images. It was expected that the increase of the thermal boundary layer would reduce the oscillation frequencies but surprisingly the opposite happened. Compared to the previous model version the oscillation frequency increased from 9.7 to 12.1 Hz.

Version 6: The exaggerated heat loss from the rich flame predicted with the previous model version caught attention to the absorption by CO. Since the molar fraction of CO is almost 0.2 in the modeled flame it is important that the absorption by CO is realistic. The WSGG model from the CFX library is the only model that contains CO as absorbing gas. All other WSGG models in the literature only contain H_2O and CO_2. The documentation for the WSGG model in CFX was a report made for a commercial company and would be difficult to get in possession of. But it was realized that the model was an extension of the model by Taylor [79]. Actually the CO partial pressure was just added to eq. 17 from Taylors’ work to become eq. 15 without changing the parameters, even though Taylor performed the parameter fitting for CO_2 and H_2O only. This causes the absorption by CO to have the same weight as the absorption by CO_2 and H_2O. It is obvious from Figure 37 to Figure 39 that this assumption is wrong. The mean absorption by CO_2 found with HITEMP is about an order of magnitude smaller than by CO_2 and H_2O. This is why CO radiation is often neglected in combustion models. But this is also wrong which may be seen in Figure 40 to Figure 42. Even though the absorption by CO is low, the radiance at 1800 K is not negligible. It is about 6 and 40 % of the radiance from CO_2 and H_2O respectively. The reason for the relatively high radiance from CO compared to H_2O is that the spectral location of the absorption band is close to the peak of the black body radiance (3500 cm^{-1} at 1800 K) while many of the H_2O bands are located further away. The absorption by CO_2 is also concentrated close to the black body peak, which explains why radiance from CO_2 dominates the other gases.

The conclusion of this analysis is that exclusion of CO from the radiation model is more correct than having it included in an incorrect way as done in the WSGG from the CFX library. Thus eq. 15 was changed to eq. 17 in this model version.

$$\varepsilon_g = \sum_{i=1}^{4} a_{gi}(T_g)\left[1 - e_i^{-K(p_{H2O}+p_{CO2})L}\right] \qquad 17$$

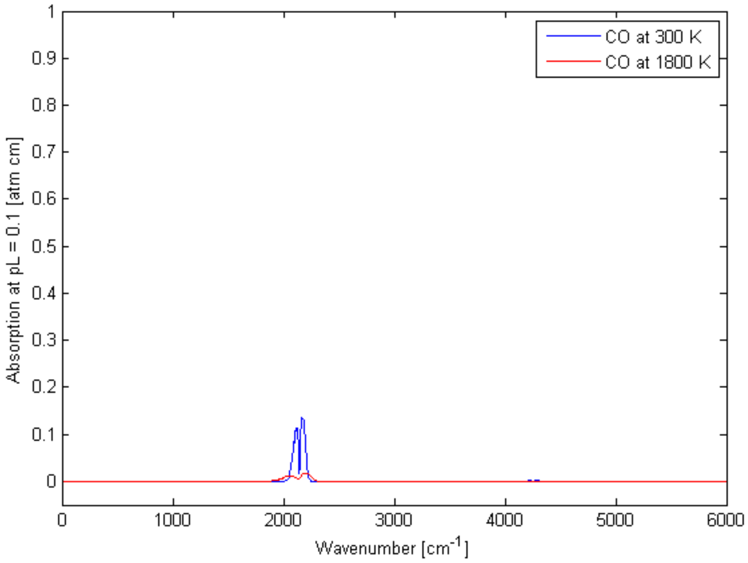

Figure 37. Spectral absorption by CO at 300 and 1800 K calculated with the HITEMP spectral radiation model. The concentration path length used for the calculations was $p_{CO}L = 0.1$ [atm cm]. Mean absorption of the entire spectra at 300 K is $2.3 \cdot 10^{-3}$ and at 1800 K it is $6.1 \cdot 10^{-4}$.

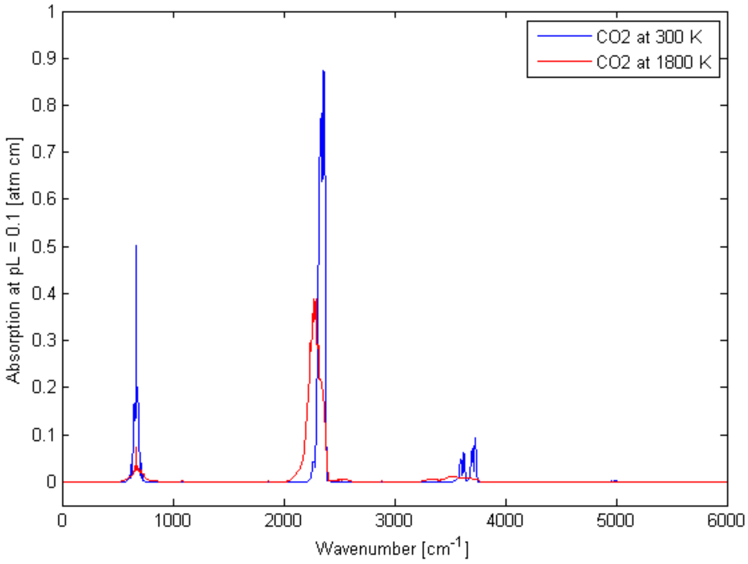

Figure 38. Spectral absorption by CO_2 at 300 and 1800 K calculated with the HITEMP spectral radiation model. The concentration path length used for the calculations was $p_{CO2}L = 0.1$ [atm cm]. Mean absorption of the entire spectra at 300 K is $1.2 \cdot 10^{-2}$ and at 1800 K it is $9.7 \cdot 10^{-3}$.

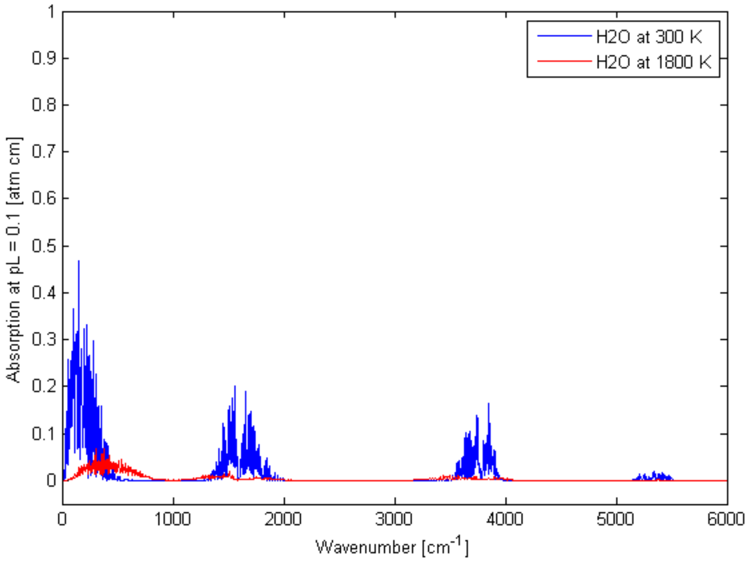

Figure 39. Spectral absorption by H_2O at 300 and 1800 K calculated with the HITEMP spectral radiation model. The concentration path length used for the calculations was $p_{H2O}L = 0.1$ [atm cm]. Mean absorption of the entire spectra at 300 K is $1.5 \cdot 10^{-2}$ and at 1800 K it is $4.1 \cdot 10^{-3}$.

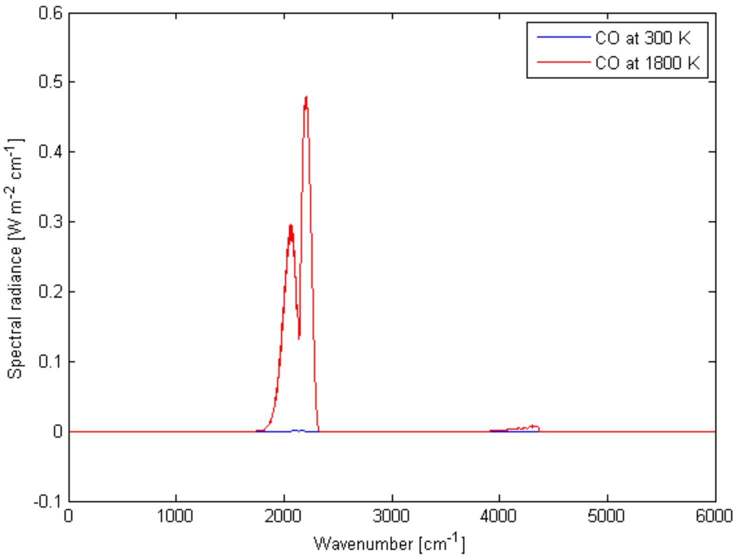

Figure 40. Spectral radiance by CO at 300 and 1800 K calculated with the HITEMP spectral radiation model. The concentration path length used for the calculations was $p_{CO}L$ = 0.1 [atm cm]. Total radiance at 300 K is $5.6 \cdot 10^{-2}$ [W m^{-2} Sr^{-1}] and at 1800 K it is 93.96 [W m^{-2} Sr^{-1}].

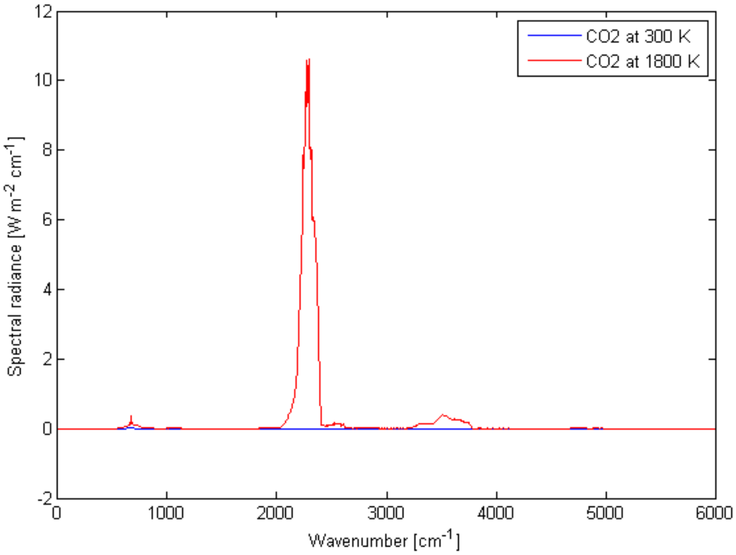

Figure 41. Spectral radiance by CO_2 at 300 and 1800 K calculated with the HITEMP spectral radiation model. The concentration path length used for the calculations was $p_{CO2}L$ = 0.1 [atm cm]. The integrated total radiance at 300 K is 1.93 [W m^{-2} Sr^{-1}] and at 1800 K it is 1521 [W m^{-2} Sr^{-1}].

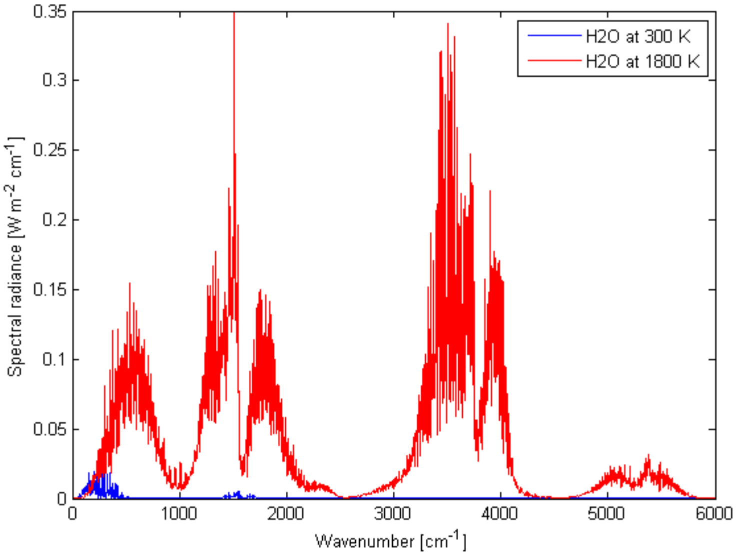

Figure 42. Spectral radiance by H_2O at 300 and 1800 K calculated with the HITEMP spectral radiation model. The concentration path length used for the calculations was $p_{H2O}L$ = 0.1 [atm cm]. The integrated total radiance at 300 K is 3.25 [W m^{-2} Sr^{-1}] and at 1800 K it is 240.43 [W m^{-2} Sr^{-1}].

The results of the helium stabilized flame (Figure 54 app A) show that the heat loss from the flame has been reduced significantly by the exclusion of CO as a radiating gas. But the heat loss is much larger than the Version 4 model without the radiation model (Figure 52 app A). The core temperatures of the flame still correspond very well to measurements of the stoichiometric flame (Figure 49 app A). For the rich flame the temperatures are now too high as they should since radiation from soot has not yet been accounted for.

The results of the unstable flame (Figure 69 app A) do look more like the images of the real flame. There is a hot triangle shaped core at the flame top just before it gets separated from the base flame and the thermal boundary layer seem smooth as on the pictures. The oscillation frequency is reduced to 10.2 Hz but still far from the measured 7 Hz.

Version 7: The investigation of the radiation contribution from the individual gases, brought attention to the importance of knowing the gas concentrations of CO_2, CO and H_2O in the entire fluid domain. The concentrations of these product gases are not just determined by the combustion process. The water gas shift reaction WGS (eq. 18) is known to equilibrate the concentrations of these gases relatively fast at temperatures above 1400 K. Thus as temperatures of the combustion products decreases the equilibrium shifts toward right in eq. 18. This leads to an increase of the radiative heat transport due to the higher CO_2 concentration. For certain this has an effect on the flame temperature in reality. Also with the first employed radiation model (version 5) where all three absorbing gases were included and equally weighed this would have an effect but it would be opposite than in reality because the total concentration of the absorbing gases is reduced. When this spectral model was used first in version 5 and showed too much heat loss, the reason was believed to be the lack of describing the WGS reaction. So in this version the effect of allowing the WGS reaction to occur was investigated. The WGS reaction is not considered as a combustion reaction and thus not included in the combusting flow section.

A WGS reaction is available in the CFX reaction library. But it did not have any effect on the composition at all. An investigation of the cited paper revealed that it was developed for catalyzed steam reforming and not combustion products. A search in the literature showed that reaction schemes of 15 or more reactions are often used to describe the WGS reaction and one step reactions were difficult to find. The use of large reaction schemes implies a larger number of gas components to be treated in the flow model and would increase the computation time significantly. Thus the search for a one step WGS reaction went on until the work from Graven and Long was found [80].

Derived from experiments with CO and H_2O in a reactor vessel at 1200 K they found the forward reaction rate in eq. 19. Since the WGS reaction will adjust to equilibrium relatively fast, it is important to apply equilibrium based reverse reaction rate. Automatic calculation of the reverse reaction rate is an option in CFX but it caused some stability problems in this work. The CFX support center explained that an error in the code cause 2D models to crash when equilibrium reverse rates are used. Thus a reverse reaction rate was fitted to the equilibrium constant. The fitting was performed with GasEq [62] at the temperatures 1500, 2000 and 2500 K leading to the reaction rate coefficient in eq. 20. The relation between equilibrium theory and reaction theory is based on reaction orders equivalent to the stoichiometric coefficients. If reaction rates with stoichiometric orders are divided by $CO^{0.5}$ in both reaction directions the orders of the forward reaction rate become as suggested by Graven (eq. 19), the backward reaction orders become as equation (eq. 20) and the equilibrium condition is still valid.

This WGS reaction had a large effect on the concentrations of the absorbing gases and this reduced the radiative heat loss by the Version 5 radiation model (with CO included) as expected, but not enough to make the flame look like the real flame. In conjunction with the Version 6 model no effect was expected since the total concentration of CO_2 and H_2O in equation 17 always is the same independent of the WGS reaction. Thus it was a surprise that the WGS actually had an influence on the heat loss as may be seen on the flame shape in Figure 55 (app A) while the core temperature is almost unchanged (Figure 49 app A). The forward WGS reaction is slightly exothermal so this was also not the reason for the loss leading to about 100 K lower temperature at some locations in the flame.

$$CO + H_2O \leftrightarrow CO_2 + H_2 \qquad 18$$

$$R_{f18} = 1.58 \cdot 10^{14} e^{\frac{33870}{\mathrm{K}}} [CO]^{0.5} [H_2O] \quad \left[\frac{\mathrm{mol}}{\mathrm{cm^3\ s}}\right] \qquad 19$$

$$R_{b18} = 1.23 \cdot 10^{19}\, T^{-1.02}\, e^{\frac{39046}{\mathrm{K}}}\, [CO_2]\, [H_2]\, [CO]^{-0.5} \quad \left[\frac{\mathrm{mol}}{\mathrm{cm^3\ s}}\right] \qquad 20$$

The explanation for the higher heat loss as equilibrium of eq. 18 shifts to the right may be found in the in the higher concentration of H_2. The diffusion of H_2 is about 5 times higher than for H_2O (Table 6) and the mole specific heat capacity of H_2O is only a little higher than for H_2. Thus when WGS is applied, more hot H_2 is produced which diffuses out of the flame and brings energy along with it.

In the solution of the stabilized flame found with the Version 7 model (Figure 55 app A) the flame shape is slightly approaching the shape of the real flame. The flame contour is less convex than without the WGS reaction and flame tip is better maintained.

In the solutions of the unstable flame (Figure 71 app A) the temperature is also reduced in the connection string just before the flame breaks up (2nd image from the right). This corresponds well with fainting of this string on the photo of the real flame. The oscillation frequency is almost unchanged at 10.3 Hz.

Version 8: The gas radiation model used in Version 6 predicted the core temperature of the stoichiometric well. It was developed by Taylor [79] who later developed another WSGG radiation model to include radiation from soot [81]. The present work gave a great opportunity to test this model since the soot concentration as well as temperatures is known from measurements. To do this the Magnusson soot model in CFX was applied but the formation and oxidation mechanisms turned off. Soot could then simply be added to the combustion products coming out of the burner without additional complexity from soot reactions. In this test the soot concentration was set to $4 \cdot 10^{-4}$ [kg/m^3] which corresponds well to the measured concentrations (Figure 45 app A) with a soot density of 2000 [kg/m^3]. The gas and soot radiation model by Taylor [81] is described with eq. 21-25. The gas concentrations are not used in the calculations of the emissivity only the soot concentration is. With the parameters in Table 8 the model applies for combustion products with the concentration ratio $p_{H2O}/p_{CO2} = 2$ and a soot concentration $C_s \leq 5 \cdot 10^{-4}$ [kg/m^3].

$$\varepsilon = \sum_{i=1}^{3} a_i(T)\left[1 - e^{-K_i L}\right] \qquad 21$$

$$a_i = b_{1i} + b_{2i} T 10^{-4}, \quad \text{i = 1, 2} \qquad 22$$

$$a_3 = 1 - (a_1 + b_2) \qquad 23$$

$$K_i = q_{1i} + q_{2i} C_s, \quad i = 1 \qquad 24$$

$$K_i = e^{q_{1i} + q_{2i} C_s}, \quad \text{i = 2, 3} \qquad 25$$

i	b_{1i} [-]	b_{2i} [T^{-1}]	q_{1i} [-]	q_{2i} [m^3 kg^{-1}]
1	0.7564	-2.182	0.09	500
2	0.0799	2.809	-0.233	672.04
3	-	-	2.452	692.61

Table 8. Parameters for a weighted sum of gray gasses model including emission from soot [81]. The parameters are suitable for combustion products with the concentration ratio p_{H2O}/p_{CO2} = 2 and a soot concentration $C_s \leq 0.0005$ [kg/m^3].

The predictions of the core temperature in the helium stabilized flames (Figure 49 app A) show that the heat loss has increased for the sooting flame (φ = 2.15) as it should and the temperature values are really close to the measurements. For the nonsooting flame (φ = 1) the heat loss has also increased even though no soot is present in the calculations, but the predictions are still reasonably close to the measurements.

The flame shape predictions during the transient unstable runs have really changed. The shape now seems too smooth compared to the real flame, but it is hard to judge because the changes in soot concentrations have to be considered to determine the luminousity of the flame.

Version 9: This and the next versions should not be considered as improvements to the model but as experiments made to understand what the oscillation frequency depends on. Since all the previous changes to thermal flow model had negative or negligible influence on the frequency, some drastically changes had to be made to change the oscillation frequency.

The Version 7 model predicts the upper half flame shapes very well for both the stabilized and unstable flame. But the lower half is bulging out on the real flame which it does not in the model predictions. This bulge is caused by the combustion process, leading to gas expansion and acceleration, and its presence may be reason for the change in frequency. A combustion model should be employed to predict this bulge shape correctly. This version is an attempt to reproduce this bulge without a combustion model to investigate whether it is reason for the low oscillation frequency. It is done by applying a velocity profile on the flow inlet (burner outlet). The velocity *v* in the normal direction *y* is 1 m/s as before but in the parallel direction *x*, the velocity *u* is calculated as $u = 0.03/x$ where *x* is in meters. Thus in the center of the inlet, the flow direction is normal to the inlet but in the periphery it is 45˚ to the normal direction pointing away from the flame center.

This unphysical boundary condition on the inlet also produces a very unphysical looking flame as may be seen in Figure 56 (app A) showing the temperature prediction of the stabilized flame.

The prediction of the unstable flame (Figure 73 app A) also looks very different from the real flame but a bulge is produced by applying this velocity profile and most importantly the oscillation frequency is reduced to 7.5 Hz.

Version 10: This version is an experiment similar to the previous but with a converging inlet flow. Thus u = -0.03/x was applied, resulting in a peripherically flow direction 45˚ to the normal direction but pointing toward the flame center.

The predicted results of the stabilized flame (Figure 57 app A) and the unstable flame (Figure 75 app A) also look unphysical but in a different way as with the diverging inlet flow. The important observation is that the oscillation frequency now is 17.1 Hz.

Combusting flow model

The experiments with the version 9 and 10 model showed that the angle of the flame exterior had a large influence on the oscillation frequency. The gas expansion caused by combustion is responsible for the diverging flow out of the burner. Thus, at this stage of development it was appropriate to extend the model with a combustion reaction.

The numerical challenge of solving the combustion equations caused some necessary changes to be made to the model to improve convergence. The Mesh size was refined in the combustion region to have a length scale of maximum 0.15 mm. This increased the number of nodes from 38000 to 69000. Further refinement has been tried but did not affect the results. The first order accurate upwind advection scheme was used and expert parameters “stiff chemistry” and “energy in mcf beta” were enabled based on recommendations from ANSYS-CFX support and had positive effect on convergence.

When a flame lift was obtained some transient effects occurred even with the helium stabilized flame. The steady state solver could not suppress these effects satisfyingly and the transient solver with 7 inner iterations per time step was used in all calculations involving combustion. The transient effect was a continuous rearrangement of the flame front. This phenomenon has also been seen in other flame experiments than the one reproduced here, so it is not necessarily unphysical. Further investigation is needed to understand this and most likely is it necessary to expand the model to three dimensions to reproduce the flame front.

The burner BC (Figure 35) was changed to reproduce the condition made by the water cooled porous burner disk. The boundary was set to be a no slip wall with constant temperature at 300 K. A source delivering reactants at 300 K was applied to the first cell layer above the burner wall.

It is very tricky to get the combustion started. The un-burnt reactants easily slip through the fine mesh if flame front has not been established yet. Then it usually ignites in the coarse mesh causing the solver to crash. A robust 3-step procedure was developed to avoid this to happen. The procedure is to start with an adiabatic wall as burner BC and deliver reactants at 1200 K from the source. Then reduce the reactant temperature to 300 K. Then change the burner BC to constant temperature at 300 K.

The CFD results presented in this work was achieved with what is generally considered as tight convergence (RMS residuals < 10^{-4}).

Version 11: Westbrook [82] has developed simple 1-step, 2-step and quasi-global reaction equations for combustion of several fuels including ethylene. In the quasi global approach a single forward reaction equation is used to describe the ethylene oxidation and a scheme of 21 forward reaction equations with equilibrium backward reaction rates was used to describe the CO-H_2-O_2 system. The 2-step model (eq. 26-30 with R = $1.986 \cdot 10^{-3}$ [kcal/(K mol)]) was chosen as the starting point for modeling the combustion reactions.

$$C_2H_4 + 2O_2 \rightarrow 2CO + 2H_2O \qquad 26$$

$$k_{f26} = 2.4 \cdot 10^{12} e^{-30/RT} [C_2H_4]^{0.1} [O_2]^{1.65} \quad \left[\frac{\mathrm{mol}}{\mathrm{cm^3\ s}}\right] \qquad 27$$

$$CO + 0.5\ O_2 \leftrightarrow CO_2 \qquad 28$$

$$k_{f28} = 3.98 \cdot 10^{14} e^{-40/RT} [CO][H_2O]^{0.5} [O_2]^{0.25} \quad \left[\frac{\mathrm{mol}}{\mathrm{cm^3\ s}}\right] \qquad 29$$

$$k_{b28} = 5 \cdot 10^{8} e^{-40/RT} [CO_2] \quad \left[\frac{\mathrm{mol}}{\mathrm{cm^3\ s}}\right] \qquad 30$$

The WGS reaction introduced in Version 7 is to slow to have influence on the combustion and was used together with the combustion reactions.

The results of the stabilized flame are shown in Figure 58 (app A). The flame temperature is 200 K higher than the adiabatic flame temperature of 1830 K for C2H4 at φ = 2.14. Furthermore, the model does not predict the flame lift that is observed on the photos (Figure 56, left in app. A).

The results of the unstable flame (Figure 76 in appendix A) show that the oscillation frequency has decreased to 8.37 Hz with the combustion model. Thus the outward directed flow in the corner of the burner outlet seen in Figure 43 seems to have great influence on the oscillation frequency. It is caused by the gas expansion which is determined by the combustion reaction.

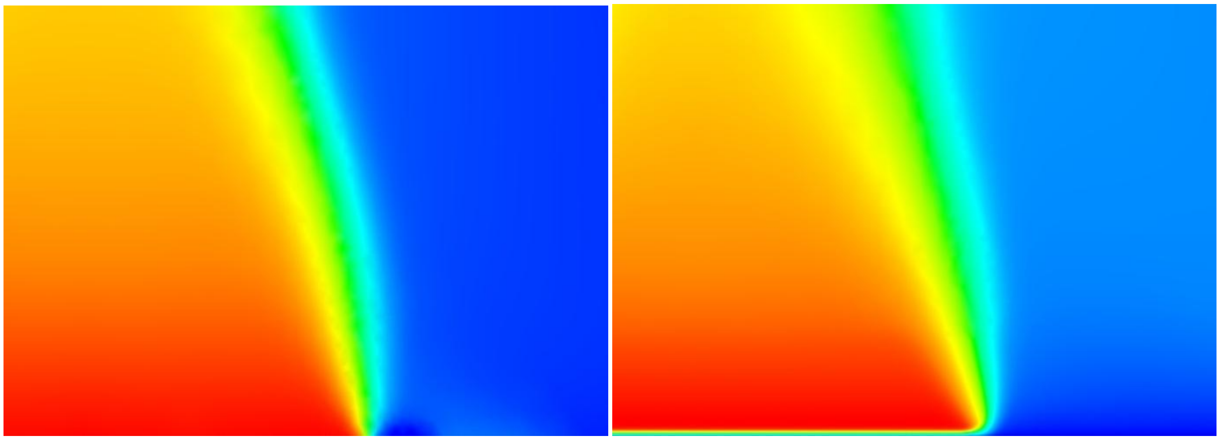

Figure 43. Close up of the temperatures in the flame corner predicted without and with combustion model, Version 8 (left) and Version 11 (right) respectively.

The flame shape of the unstable flame seen in Figure 76 in app A, seem to smooth compared to the pictures, but they are not really comparable since the flame temperature is too high.

Version 12: Since the 2-step reaction model in Version 11 did not provide satisfying results many considerations were done for the next improvement of the model.

The model is not showing a flame lift because the flame speed predicted by the 2-step reaction is too high. It could be lowered by reducing the pre-exponential factor in eq. 27, but this would also increase the temperature further because less heat would be lost to the burner surface.

The predicted temperature is too high because no H_2 is produced from the stoichiometric equations (eq. 26 and 28). The adiabatic flame temperature calculated in GasEq [62] with and without H_2 in the product list is 2016 and 1830 K respectively.

In the process of choosing the next step to improve the model it was decided to test the 1 and 2-step reactions by Westbrook in Chemkin against some of the most validated full chemistry reaction schemes. Temperature measurements at varied equivalence ratios used for validation of the thermometry method (Figure 29) were chosen as test case. The Gri-Mech 3.0 [83] and the USC-Mech 2.0 [84] full chemistry reaction schemes were chosen as bench marks. Gri-Mech 3.0 contains 325 elementary reactions and 53 species, including ethylene but has only been optimized for methane, ethane and propane. USC-Mech 2.0 contains 784 elementary reactions and 111 species and has been optimized for a large number of fuels including ethylene. The Chemkin premixed laminar burner stabilized flame model was used for all the calculations. The low reaction order of C_2H_4 in the 1 and 2-step reactions is causing problems in Chemkin when the equivalence ratio is low. The reason for this is that the reaction rate stays high even though the C_2H_4

concentration approaches zero, causing products to go out of bounds. The successful calculations with the four reaction mechanisms together with measurements are shown in Figure 44. The comparisons show that the GRI mechanism predicts the temperature very well with $\varphi < 1.5$ but not at higher equivalence ratios. The USC mechanism show almost the same tendency but at approximately 100 K higher temperatures. The 1 and 2-step reactions are both qualitatively and quantitatively incorrect.

Based on this investigation there is no reason to believe that any available reaction mechanism would be able to describe the flame correctly under a wide range of conditions. Fitting of a relatively simple reaction model to measurements from flame conditions in the range of interests seem to be the best choice, particularly for the use in CFD where computational cost is an issue.

Extensive fitting of some reaction model to make it valid for different flame conditions was outside the scope of this project. However, the experimental setup would be well suited for it.

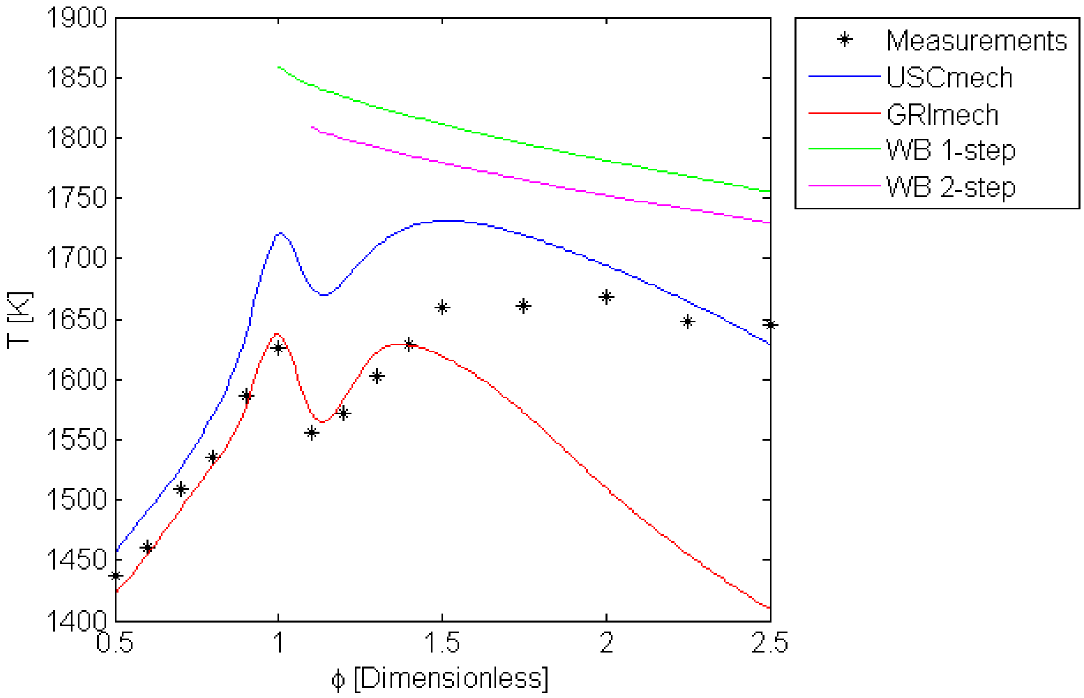

Figure 44. Comparison of calculated and measured flame temperatures. The temperatures are at 8.5 mm height in ethylene/air flames with varied equivalence ratios and fixed total cold flow rate of 10 SLM.

To get on with the improvement of the CFD model a very simple reaction model was developed specifically for the present case. Based on chemical equilibrium found with

GasEq [62] a stoichiometric equation (eq. 31) was derived that would ensure equilibrium product composition at φ = 2.15.

$$C_2H_4 + 1.3999\ O_2\ \rightarrow\ 1.8018\ CO + 0.1982\ CO_2 + 1.3985\ H_2 + 0.6015\ H_2O \qquad 31$$

$$k_{f31} = 6.35 \cdot 10^{12} e^{-30/RT} [C_2H_4]^{0.1} [O_2]^{1.65} \quad \left[\frac{\mathrm{mol}}{\mathrm{cm^3\ s}}\right] \qquad 32$$

The reaction orders and activation energy were taken from Westbrooks 1 and 2-step reactions and the pre exponential factor was fitted to achieve the proper flame lift. Different reaction orders and activation energies have been tried only with slight changes to the flame thickness as result, but the general shape of the flame was unchanged if the pre exponential factor had been refitted to produce the same flame lift.

With the fitted 1-step reaction the flame lift correspond well to the observed height of the blue bands from CH radiation (Figure 47). Even a cellular structure of the flame front is present in the predicted flame similar to the real flame. However, the exact shape of the flame front has not been possible to determine because it never stabilizes to a fixed location, even though the solution for each time step has converged very tightly. It is probably necessary to expand the model to 3D to get the complete picture of how the model predicts the shape of the flame front.

The results of the stabilized flame are shown in Figure 58 in appendix A. Now the bottom part of the flame compares well with the real flame. It bulges out very similar to the real flame but it fails narrow in enough at higher levels. This is also seen in the plot of the core temperature (Figure 49 in app A). The temperature drops off too fast compared to the measurements. The large difference in core temperatures between results from Version 8 and 12 with latter being the lowest is a surprise. The temperature and gas composition are identical at 10 mm height, the same thermal radiation model is used but Version 8 contain soot, thus Version 8 model should have the highest heat loss. The reason for this is that the version 12 flame has a larger cross section area due to the gas expansion. It reduces the gas velocity and allows more time for loss of heat.

The results of the unstable flame (Figure 77) show that the flame lift has reduced the oscillation frequency to 7.57 Hz which is really close to the measured 6.98 Hz. But the flame shape seems to smooth with too low temperature gradients.

Version 13: CFX contain a simple semi empirical soot model called Magnussen soot model. It has been demonstrated to perform reasonably well in diffusion flames [85] as well as turbulent flames [86]. Soot is treated as spheres of one size and is formed in two steps (eq. 33-35 and Table 9).

$$M_s = A\rho_s \frac{\pi d^3}{6} \quad \left[\frac{\mathrm{kg}}{\mathrm{mol}}\right] \tag{33}$$

$$\frac{\partial[\mathrm{nuclei}]_f}{\partial t} = a_0 f_c \rho Y_f e^{-\frac{T_{A,0}}{T}} + (f-g)[\mathrm{nuclei}] - g_0[\mathrm{soot}][\mathrm{nuclei}] \quad \left[\frac{\mathrm{mol}}{\mathrm{m^3 s}}\right] \tag{34}$$

$$\frac{\partial[\mathrm{soot}]_f}{\partial t} = (a - b[\mathrm{soot}])[\mathrm{nuclei}] \quad \left[\frac{\mathrm{mol}}{\mathrm{m^3 s}}\right] \tag{35}$$

$$\frac{\partial[\mathrm{nuclei}]_{ox}}{\partial t} = \frac{[\mathrm{nuclei}]}{[\mathrm{fuel}]}\frac{d[\mathrm{fuel}]}{dt} \quad \left[\frac{\mathrm{mol}}{\mathrm{m^3 s}}\right] \tag{36}$$

$$\frac{\partial[\mathrm{soot}]_{ox}}{\partial t} = \frac{[\mathrm{soot}]}{[\mathrm{fuel}]}\frac{d[\mathrm{fuel}]}{dt} \quad \left[\frac{\mathrm{mol}}{\mathrm{m^3 s}}\right] \tag{37}$$

Symbol	Description	Value	Units
M_s	Molar mass of soot		[kg/mol]
A	Avogadro's number	$6.02214199 \cdot 10^{23}$	[part/mol]
ρ_s	Soot density	2000	[kg/m^3]
d	Soot particle diameter	$17.85 \cdot 10^{-9}$	[m]
a_0	Model parameter	$2.24 \cdot 10^{-9}$	[mol/kg/s]
f_c	Carbon mass fraction of fuel (C_2H_4)	24/28	[kg/kg]
ρ	Gas density		[kg/m^3]
Y_f	Fuel mass fraction		[kg/kg]
$T_{A,0}$	Model parameter	90000	[K]
T	Gas temperature		[K]
(f-g)	Model parameter	100	[1/s]
g_0	Model parameter	$6.02 \cdot 10^{8}$	[m^3/mol/s]
a	Model parameter	$1 \cdot 10^{5}$	[1/s]
b	Model parameter	$4.82 \cdot 10^{10}$	[m^3/mol/s]

Table 9. Symbols used in the Magnusson soot model. The model parameters are developed by Tesner [85] and are based on measurements in acetylene diffusion flames.

The first step determines the formation rate of “radical nuclei” which is a sort of soot precursor. The second step determines the formation of soot based upon the presence of radical nuclei. The oxidation rate of radical nuclei and soot is assumed equal to the fuel oxidation rate but scaled with the concentration ratio (eq. 36 and 37).

The results of the stabilized flame are shown in Figure 60 in appendix A. The flame shape is almost identical with the previous one without soot. The upper part of the flame is narrowing in slightly more, indicating a larger heat loss. This may also be seen in Figure 49 in app A of the flame core temperature. The core temperature is dropping off more but the additional heat loss caused by the soot radiation is smaller than expected. Particularly since the soot concentration predicted by the soot model is an order of magnitude too high (Figure 48). This is not very surprising because the model parameters has been calibrated with measurements in acetylene flames [85] and acetylene is a very sooting fuel.

Version 14: The Magnussen soot model was developed on the basis of measurements in diffusion flames were soot oxidation is significant in the post flame region due to the excess of oxygen. The flame in this work is premixed and the combustion products are completely shielded from oxygen in the burner chamber. It seems unlikely that any oxidation should occur under these conditions. The assumption of neglecting the soot oxidation in the present case seems better than using the very simplified soot oxidation approach from the standard Magnussen model (eq. 36-37).

In this version the soot oxidation reactions were turned off to investigate the effect of them. Figure 48 shows that the soot volume fractions were increased by this, but not much. The small effect of the soot oxidation reactions may be caused by simultaneous formation and oxidation of the radical nuclei in the flame front where some oxygen is still present. It is not possible to conclude if some soot oxidation of this kind should be expected or not, and it was decided to continue without soot oxidation.

The results of the stabilized flame are shown in Figure 60 in app A. The results are very similar to the previous version. Though, the heat loss is slightly larger which is evident in Figure 49 in app A of the core temperature.

Version 15: Fitting of the soot model parameters was performed to achieve the measured soot volume fractions. The best result was obtained with the parameters: a_0 = $3.32 \cdot 10^{14}$ mol/(kg s), $T_{A,0}$ = 83000 K and $1.63 \cdot 10^{10}$ m^3/(mol s).

To enable comparison between measurements and model predictions the average of 5 soot volume fractions was used. They were taken at points evenly distributed between the symmetry axis and a radius of 37.5 mm where the opening of the optical purge tube was located in the measurements. The individual and the average soot volume fractions are shown in Figure 45, together with the measurements.

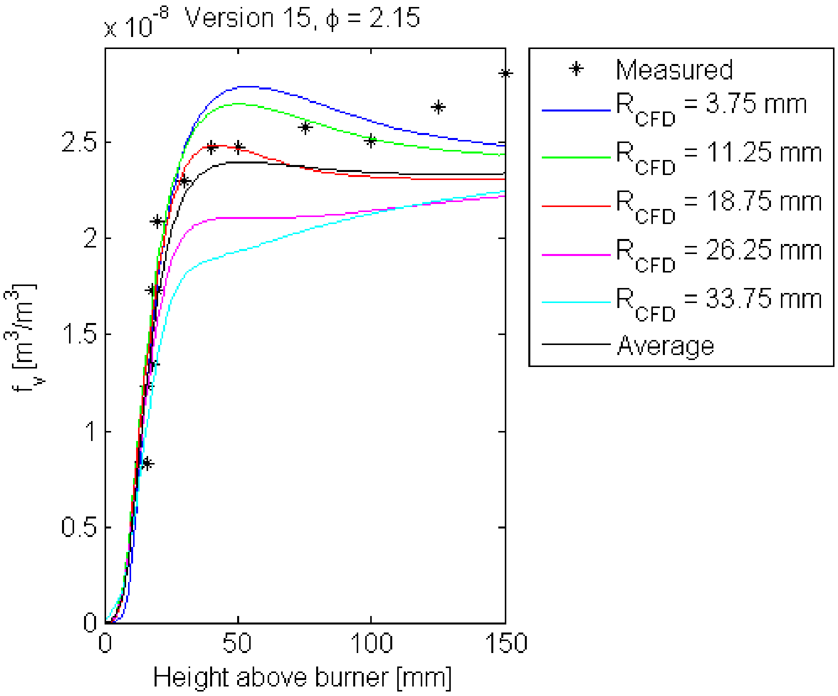

Figure 45. Graph of measured soot volume fractions *f_v* versus CFD model results. *f_v* is the average of *$f_{v,x}$* at 10 equidistant locations along the distance L = 75 mm which was optical path used in the measurements but due to symmetry only five radial locations are needed. *f_v* at these locations are shown as well as the average values are shown.

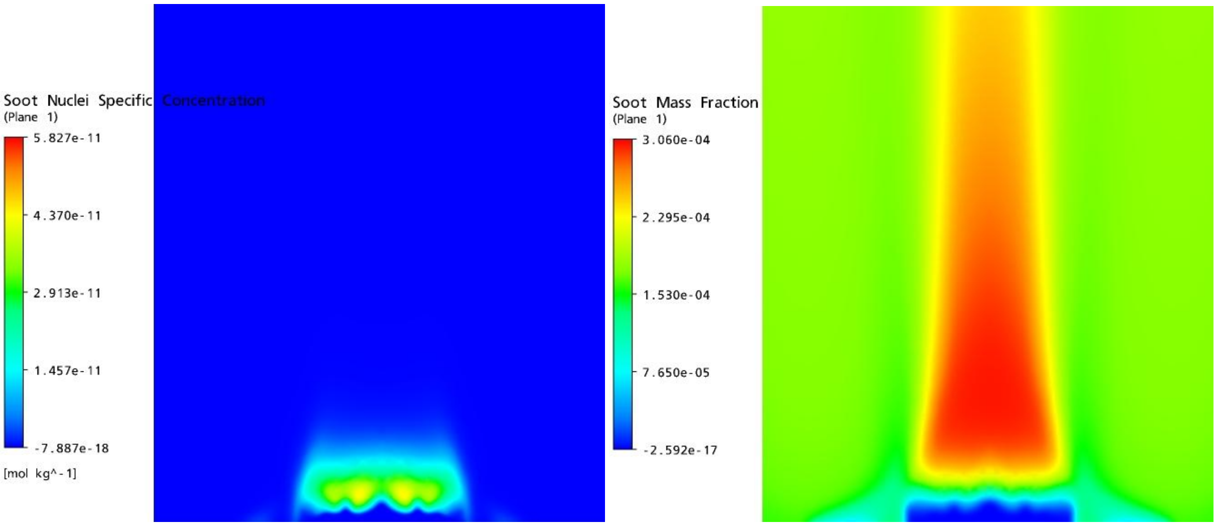

Figure 46. CFD predictions of the radical nuclei concentration and soot mass fractions achieved with Version 15.

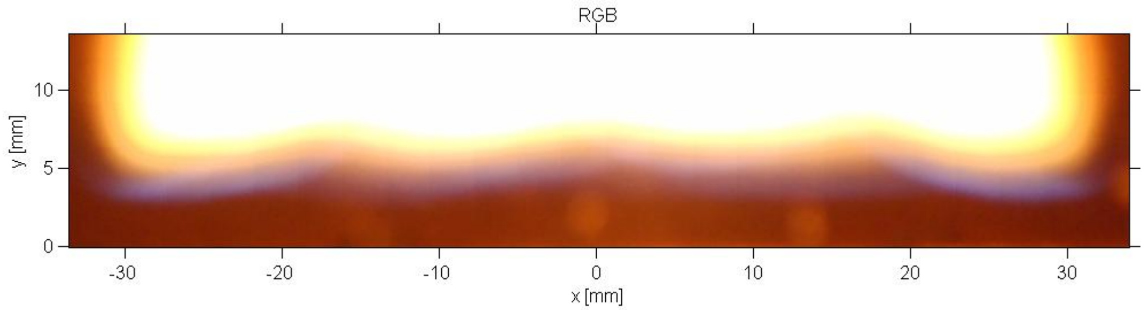

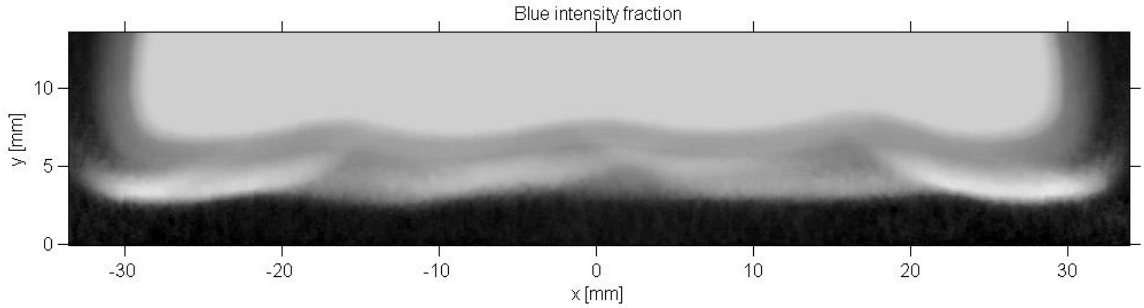

CFD Temperatures and streamlines

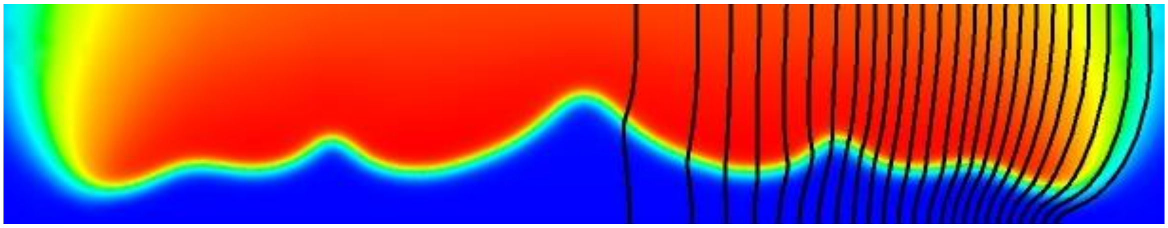

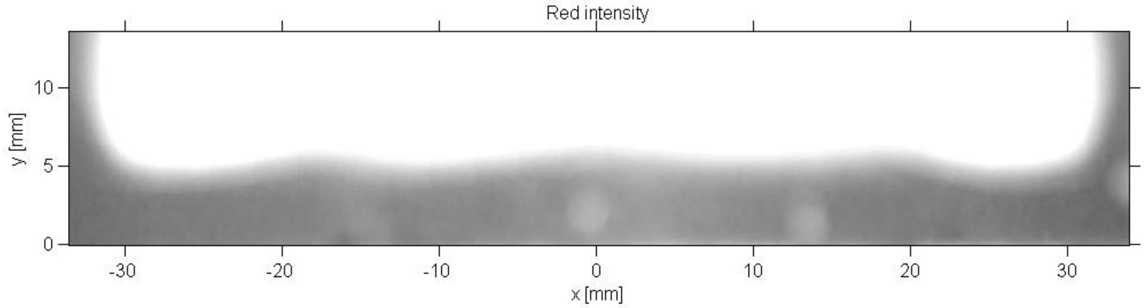

CFD soot mass fractions and streamlines

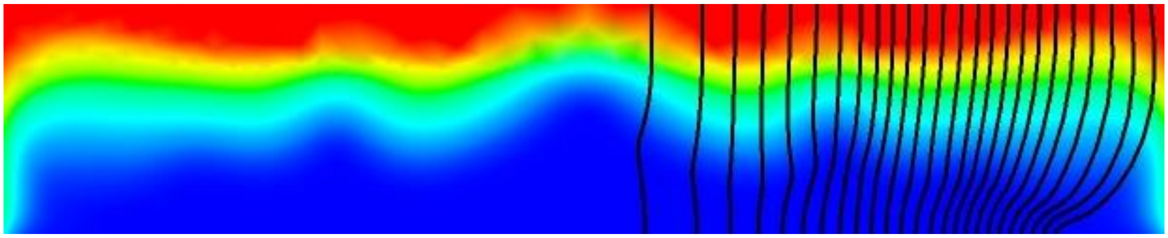

Figure 47. Comparison between model predictions and photos of the flame front. The RGB picture is not manipulated, while the gray intensity of the second photo scales with the fraction of blue signal to the total signal. This enhances the visibility of the blue bands were the flame front is located. The gray scale photo of the red intensity enhances and isolates the soot luminosity, and shows were both soot and high temperatures are present.

The CFD model predicts the measured soot volume fractions well (average vs. measured in Figure 45) and the visual impression of the model prediction is also good (Figure 46 and Figure 47). Since the model parameters have been fitted to make the model suit for these measurements it does not prove that the soot model is valid at other flame conditions.

The results of the stabilized flame are shown in Figure 61 in app A. The results are very similar to the two previous versions. Though, the heat loss is smaller which is evident in Figure 49 in app A of the core temperature. The core temperature is almost identical with the result from Version 12 without soot. It seems likely that too much of the emissivity of soot is covered by the non concentration dependent terms in the absorption coefficients (eq. 24, 25). Because the soot concentration is temperature dependent an error of that kind would influence the temperature dependence of the emissivity.

The results of the unstable flame (Figure 79) are very similar to Version 12 without soot but the temperature gradients are larger causing the oscillating flame to look less smooth and wilder, which is closer to the shape of the real flame. The oscillation frequency is basically unchanged (7.53 Hz) and close to the measured frequency (6.98 Hz).

Conclusion

Early in this PhD project it was realized that experiments had to be performed to gain understanding of the mechanisms in a premixed flame and to be able to validate models. It was chosen to build an experimental setup with a commercial flat flame burner of the McKenna type. The burner was located in a long chamber flushed with inert gas to omit a diffusion flame when rich mixtures were used. This setup offers some of the features of plug flow reactor experiments, but at true flame temperatures and with better optical access. The most important feature is that the flame is quasi one dimensional and laminar, which enables modeling in Chemkin with full chemical reaction schemes. Ethylene was primarily used as fuel due to a carbon to hydrogen ratio similar to diesel. The flames with rich mixtures of ethylene and air were believed to be close enough to those of the CI combustion engine that experience could be carried over.

Unfortunately a pre-mixed flat flame exhibit severe instability in the flow of the flame products. Thus much effort was spent on dealing with this instability to establish a steady flame. The post flame instability of a $\phi = 2.14$ pre-mixed ethylene/air flame was investigated. The oscillation frequency of a premixed flame this large has not been reported before and was found to be 7 Hz in this work.

A nonintrusive method, also not reported before, has been demonstrated to stabilize premixed flat flames and is called helium stabilization. The basic of method is to ensure nearly equal gas densities inside and outside the flame by diluting the surrounding gas with helium, and thus minimize destabilizing buoyancy effects. The method has demonstrated to be effective for many different flame configurations. Only at one particular configuration, a new post flame instability phenomena at 105 Hz was discovered on high speed captures, and is believed to be a rotating kind of instability related to the combustion process and not the fluid dynamics.

Some preliminary studies of radiant emissions from helium stabilized ethylene/air and methane/oxygen flames have been performed. The steadiness and good optical access to the flame enables photographing with a high light sensibility. This has for first time made it possible to show that nano particles below the sooting threshold ($C/O_C = 0.62$ for C_2H_4/air and $C/O_C = 0.46$ for CH_4/O_2) are weakly luminous almost down the C/O ratio where they become detectable with LII and UV arbsorption ($C/O = 0.48$ for C_2H_4/air and $C/O = 0.35$ for CH_4/O_2).

It has also been shown that highly lifted flames may be completely stabilized if a stoichiometric H_2 shielding flame is combined with the helium stabilization. This may yield important information about the pre combustion zone in future work due to the good access for line of sight optical measurements.

Another big challenge in the project was to determine the temperature of the sooting flame accurately. A thermometry method specifically for pre-mixed flat flames, based on IR emission and absorption, measured with a commercial FT-IR spectrometer was developed. Means were developed to minimize the concentration of cold combustion products in the IR path outside the flame. Methods to interpret the derived temperature spectra were developed and tested.

Comprehensive investigations of the precision and accuracy of the method was performed separately. The precision was determined on the basis of a large number of measurements with a broad variation of flame conditions and conditions of the experimental setup. The investigation shows that an important strength of the method is its reliability with respect to variations in the experimental setup. Even with non-optimized installation and operation of the method, the average line of sight temperatures with a precision of +/- 2 % may easily be achieved. With a thorough installation and operation the method determines the temperature of the flame core to within +/- 1 %, in spite of the line of sight principle. Cyclic deviations of +/- 3 K of the black body temperature were the limitation for further improvements to the precision in this work.

A final determination of the method accuracy could not be realized since the true temperature was unknown. But temperature measurements with different thermometry techniques known from the literature were reproduced and compared. Some of these methods were valid only for a limited range of flame conditions. Thus, the consistency of the most established flame thermometry techniques was evaluated, using the IR emission absorption method as a link. To the authors' knowledge this kind of investigation has not been reported before.

With the IR emission absorption method as reference the investigation shows:

- Excellent agreement with the laser light Rayleigh scattering method for $\varphi \leq 1$. As φ increases toward 1.5 the laser light Rayleigh scattering method shows higher temperature, eventually with about 80 K deviation.
- Excellent agreement with thermocouple measurements for $\varphi \leq 1.5$. Except for measurements located close to the reaction zone with $\varphi = 1.5$, where the thermocouple measurements are about 30 K higher.

Qualitative agreement with thermocouple measurements in sooting flames, but the temperatures are 80 to 150 K lower when measured with the thermocouple.

- Excellent qualitative agreement with dual broadband rotational CARS over the entire range of equivalence ratios, but the temperatures are about 80 K higher measured with CARS.
- For $1.2 < \varphi < 2.3$ temperatures measured with sodium line reversal are about 100 K lower.
- Measurements for $\varphi = 2.3$ with the multi color method show about 150 K higher temperatures. Except for measurements located close to the reaction zone where the measurements are about 400 K higher.

An optical method was used to measure the soot content in terms of soot volume fraction. The measurement was based on absorption of light with wavelength between 500 and 520 nm.

Finally a CFD model of the pre-mixed flat flame was developed. The commercial CFD software CFX 11.0 was used. Three cases of ethylene/air flames well known from the experimental work, was used for the model validation. Two cases were helium stabilized flames with φ = 1 and 2.14. The third case was an unstable flame with φ = 2.14. The unstable case was used to test whether a transient model would be able to predict the frequency and shape of the unstable sooting flame. The stable cases were easier to treat both experimentally and numerically, and were used for more detailed validation.

The model was developed stepwise from the simplest possible starting point. The first part of the development was made on a model of thermal fluid flow only. The model was incrementally extended with; temperature dependent thermal conductivity, temperature dependent viscosity, temperature dependent mass diffusion, thermal gas radiation, water gas shift reaction and soot radiation. In the second part combustion was introduced. A simple reaction model well known from the literature did not predict the features of the real flame, thus another simple reaction was developed specifically for this purpose. A simple soot formation model developed for acetylene diffusion flames was validated against the soot measurements. The model parameters were fitted to predict the measured soot volume fractions in the pre-mixed ethylene flame. The provided results offer insight to the sensitive of the predictions to the model variations.

The general conclusion is that the experimental setup used in this work is ideal for validation of combustion, soot formation and radiation models in cases of pre-mixed laminar flames. The models tested in this work are simple semi empirical models that are computational affordable and easy to implement in most CFD software's. In spite of the rough simplification they build upon, they perform quite well.

In the attempts to create a predictive CFD based design tool for internal combustion engines and other combustion devises, it is the author's recommendation to improve and/or extend the simple models. While the use of complex but physically more correct models would not necessarily provide much more correct results without fitting, but for certain be more computational challenging and costly. It is the impression of the author that the most important task in achieving predictive models is the validation with experiments.

References

1. P. F. Flynn, R. P. Durrett, G. L. Hunter, A. Z. Loye, O. C. Akinyemi, J. E. Dec, C. K. Westbrook, SAE Technical Paper Series 1999-01-0509 (1999)
2. S. C. Sorensen, Engine Principles and Vehicles, Technical University of Denmark (2008).
3. M. S. Skjøth-Rasmussen, Modeling of Soot Formation in Autothermal Reforming, Technical University of Denmark (2003).
4. C. Eckbreth, Laser Diagnostics for Combustion Temperature and Species, 2nd ed., Gordon and Breach Science Publishers, Amsterdam, NL, 1996, p. 182 and 198.
5. C.S. McEnally, U.O. Koylu, L.D. Pfefferle and D.E. Rosner, Combust. Flame 109 (1997), pp. 701–720.
6. L.W. Kostiuk and R.K. Cheng, Exp. Fluids 18 (1994) 59–68.
7. L.W. Kostiuk, R.K. Cheng, Combust. Flame 103 (1995) 27–40.
8. D.S. Chamberlin, A. Rose, Proc. Combust. Inst. 1-2 (1948) 27-32.
9. P.-E. Bengtsson and M. Alden. Combust. Flame 80 (1990) 322–328.
10. B. Axelsson, R. Collin and P.-E. Bengtsson, Appl. Opt. 39 (21) (2000) 3683–3690
11. F. Migliorini, S. De Iuliis, F. Cignoli, G. Zizak, Combust. Flame 153 (2008) 384–393.
12. I. Kimura, Proc. Combust. Inst. 10 (1965) 1295–1300.
13. T.-Y. Toong, R.F. Salant, J.M. Stopford and G.Y. Anderson, Proc. Combust. Inst. 10 (1965) 1301-1313.
14. A.J. Grant and J.M. Jones, Combust. Flame 25 (1975) 153–160.
15. J. Buckmaster and N. Peters, Proc. Combust. Inst. 21 (1986) 1829–1836.
16. L.D. Chen and W.M. Roquemore. Combust. Flame 66 (1986) 81–86
17. L.-D. Chen, J.P. Seaba, W.M. Roquemore and L.P. Goss, Proc. Combust. Inst. 22 (1988) 677–684.
18. L.-D. Chen, V. Vilimpoc, L.P. Goss, R.W. Davis, E.F. Moore and W.M. Roquemore, Proc. Combust. Inst. 24 (1992) 303-310.
19. R. W. Davis, E. F. Moore, L.-D. Chen, W. M. Roquemore, V. Vilimpoc, and L. P. Goss, Theoret. Comput. Fluid Dynamics 6 (2-3) (1994) 113-123.
20. V.R. Katta, L.P. Goss and W.M. Roquemore, AIAA J. 32 (1994) 84–94.
21. V.R. Katta, L.P. Goss and W.M. Roquemore, Combust. Flame 96 (1994) 60-74.
22. J.L. Ellzey and E.S. Oran, Proc. Combust. Inst. 23 (1991) 1635–1640.
23. J. Kim, K.N. Kim, S.H. Won, O. Fujita, J. Takahashi, S.H. Chung, Combust. Flame 145 (2006) 181-193.
24. S.H. Won, S.H. Chung, M.S. Cha and B.J. Lee, Proc. Combust. Inst. 28 (2000) 2093–2099.

25. A.J. Lock, A.M. Briones, X. Qin, S.K. Aggarwal, I.K. Puri and U. Hegde, Combust. Flame 143 (2005) 159–173.
26. R. Azzoni, S. Ratti, I.K. Puri and S.K. Aggarwal, Phys. Fluids 11 (1999) 3449–3464.
27. Z. Shu, B. Krass, C. Choi, S.K. Aggarwal, V. Katta and I.K. Puri, Proc. Combust. Inst. 27 (1998) 625–632.
28. V.R. Katta and W.M. Roquemore. Combust. Flame 102 (1995) 21–40.
29. T. Fujii, Int. J. Heat Mass Transfer 6 (1963) 597–606.
30. L. Pera and B. Gebhart, J. Heat Mass Transfer 14 (1971) 975–984.
31. T. Yuan, D. Durox and E. Villermaux, Exp. Fluids 17 (5) (1994) 337-349.
32. F. Xu, P.B. Sunderland and G.M. Faeth, Combust. Flame 108 (1997) 471–493.
33. B.S. Haynes, H. Jander and H.Gg. Wagner, Proc. Combust. Inst. 17 (1979) 1365–1374.
34. H. Mätzing and H.Gg. Wagner, Proc. Combust. Inst. 21 (1988) 1047–1055.
35. H. Böhm, D. Hesse, H. Jander, B. Lüers, J. Pietscher, H.Gg. Wagner and M. Weiss, Proc. Combust. Inst. 22 (1989) 403–411.
36. J.H. Kent and H.G. Wagner, Combust. Flame 47 (1982) 53–65.
37. C.R. Shaddix, T.C. Williams, L.G. Blevins and R.W. Schefer, Proc. Combust. Inst. 30 (2005) 1501–1508.
38. S. Prucker, W. Meier and W. Stricker, Rev. Sci. Instrum. 65 (1994) 2908–2911.
39. http://flatflame.com/
40. K. Remenyi, Akademiai Kiado, Combustion Stability, Budapest, Hungary, 1980, p. 75.
41. W. Lee, J.G. Lee and D.A. Santavicca, JSME Int. J. series B, 48 (2) (2005) 305-309.
42. A. G. Gaydon, The Spectroscopy of Flames, 2. Ed, Chapman and Hall, London, Uk, 1974, p. 107 and 358.
43. D.B. Olson, J.C. Pickens and R.J. Gill, Combust. Flame 62 (1985) 43–60.
44. P. Minutolo, G. Gambi and A. D'Alessio, Proc. Combust. Inst. 27 (1998) 1461–1469.
45. A.C. Barone, A. D’Alessio and A. D’Anna, Combust. Flame 132 (2003) 181–187.
46. P. Minutolo, A. D'Anna and A. D'Alessio, Combust. Flame 152 (2008) 287-292.
47. D. Cecere, A. Bruno, P. Minutolo and A. D'Alessio, Synth. Met. 139 (2003) 653–656.
48. http://www.schneideroptics.com/info/handbook/pdf/B+WHandbook_Full.pdf
49. A. D’Alessio, G. Gambi, P. Minutolo, S. Russo and A. D’Anna, Proc. Combust. Inst. 25 (1994) 645–651.
50. C. Buchta, A. D'Alessio, A. D'Anna, G. Gambi, P. Minutolo and S. Russo, Planet. Space Sci. 43 (1995) 1227–1232.

51. E.W. Kaiser, K. Marko, D. Klick, L. Rimai, C. Wang, B. Shirinzadeh and D. Zhou, Combust. Sci. Technol. 50 (1986), p. 163-183.
52. A.G. Gaydon, H.G. Wolfhard, Flames: Their Structure, Radiation, Temperature, 3 ed., Chapman & Hall, London (1970) p. 229, 251 and 285.
53. G. Sutton, A. Levick, G. Edwards and D. Greenhalgh, Combust. Flame 147 (2006) p. 39–48.
54. F. Vestin, M. Afzelius, C. Brackmann and P.-E. Bengtsson, Proc. Combust. Inst. 30 (2005) p. 1673–1680.
55. R.H. Tourin, Spectroscopic gas temperature measurement. Elsevier, Amsterdam (1966) p. 25, 29 and 85.
56. P. R. Solomon, P. E. Best, R. M. Carangelo, J. R. Markham, P. L. Chien, R. J. Santoro, H. G. Semerjian, Proc. Combust. Inst. 21 (1986) p. 1763-1771.
57. P.E. Best, P.L. Chien, R.M. Carangelo, P.R. Solomon, M. Danchak and I. Ilovici, Combust. Flame 85 (1991) p. 309-314.
58. A. Ivarsson, Stabilization of pre-mixed flat flame, Combust. Flame, Submitted for review, Attached to this paper.
59. S. Prucker, W. Meier and W. Stricker, Rev. Sci. Instrum. 65 (1994) p. 2908–2911.
60. www.flatflame.com
61. P. R. Griffiths, J. A. de Haseth, Fourier Transform Infrared Spectrometry, Wiley, New York (1986) p. 33.
62. www.gaseq.co.uk
63. S. Silverman, J. Opt. Soc. Am. 39 (1949) p. 275.
64. D. F. Marran, J. E. Cosgrove, J. Neira, J. R. Markham, R. R. Strange and R. S. Rutka, Proc. SPIE 4201 (2001) p. 118-127.
65. B. Zhao, Z. Yang, J. Wang, M.V. Johnston and H. Wang, Aerosol Sci. Technol. 37 (2003) p. 611–620.
66. F. Xu, P.B. Sunderland and G.M. Faeth, Combust. Flame 108 (1997) p. 471–493.
67. B. Axelsson, R. Collin and P.-E. Bengtsson, Appl. Opt. 39 (21) (2000) p. 3683–3690.
68. P. Minutolo, G. Gambi and A. D'Alessio, Proc. Combust. Inst. 27 (1998) p. 1461–1469.
69. Gothaniya G., Lee, S.-Y.. Menon, A.V., Iyer, S.,. Linevsky, M.J., Santoro, R.J., Litzinger, T.A., “A study on the effect of experimental setup configuration on soot formation in a laminar premixed ethylene-air flame”,in Combustion Generated Fine Carbonaceous Particles, Karlsruhe University Press, in press.
70. M.Y. Choi, A. Hamins, G.W. Mulholland and T. Kashiwagi, Combust. Flame 99 (1994) pp. 174–186.

71. S. Gordon, B. J. McBride, Computer Program for Calculation of Complex Chemical Equilibrium Compositions, Rocket Performance, Incident and Reflected Shocks and Chapman-Jouguet Detonations, NASA Report SP-273 (1971)
72. R. J. Kee, F. M. Rupley and J. A. Miller, Chemkin-II: A Fortran Chemical kinetics Package for the Analysis of Gas-Phase Chemical Kinetics, Sandia National Laboratories Report, SAND89-8009 (1991).
73. F. M. White, Viscous Fluid Flow, 3th Edition, McGraw-Hill, New York (2006).
74. D. R. Lide, ed., CRC Handbook of Chemistry and Physics, 89th Edition, CRC Press/Taylor and Francis, Boca Raton, FL, (Internet Version 2009).
75. S. R. Turns, An Introduction to Combustion, 2th Edition, McGraw-Hill, New York (2000).
76. P.J. Coelho, Journal of Quantitative Spectroscopy & Radiative Transfer 74 (2002) p. 307–328.
77. http://www.spectralcalc.com
78. H. C. Hottel and A. F. Sarofim, Radiative Transfer, McGraw-Hill, New York (1967).
79. P. B. Taylor and P. J. Foster, Int. J. Heat Mass Transfer 17 (1974) p. 1591-1605.
80. W. M. Graven and F. J. Long, J. Am. Chem. Soc., 76 (10) (1954) p. 2602-2607.
81. P. B. Taylor and P. J. Foster, Int. J. Heat Mass Transfer 18 (1975) p. 1331-1332.
82. C.K. Westbrook and F.L. Dryer, Combust. Sci. Technol. 27 (1-2) (1981), pp. 31–43.
83. http://www.me.berkeley.edu/gri-mech/releases.html
84. http://ame-www.usc.edu/research/combustion/combustionkinetics/research.html
85. P. A. Tesner, T. D. Snegirova and V. G. Knorre, Combust. Flame 17 (1971) pp. 253-260.
86. B.F. Magnussen and B.H. Hjertager, Proc. Combust. Inst. 16 (1977) pp. 719–729.

Appendix A: Flame gallery

Version number:	Description:
1	Basic model with constant gas properties, without radiation and reactions
2	Ver. 1 + temperature dependent thermal conductivity
3	Ver. 2 + temperature dependent viscosity
4	Ver. 3 + temperature dependent gas diffusivity
5	Ver. 4 + thermal radiation model for CO, CO_2 and H_2O
6	Ver. 4 + thermal radiation model for CO_2 and H_2O
7	Ver. 6 + water gas shift reaction
8	Ver. 4 + water gas shift reaction + thermal radiation model for CO_2, H_2O and soot. The soot concentration coming out of the burner for φ = 2.15 is 4e-4 kg/m^3 and 0 kg/m^3 for φ = 1
9	Ver. 7 + 45˚ diverging flow out of the burner
10	Ver. 7 + 45˚ converging flow out of the burner
11	Ver. 8 without any soot + WB 2-step combustion reaction
12	Ver. 8 without any soot + fitted 1-step combustion reaction
13	Ver. 8 + fitted 1-step combustion reaction + Magnusson soot model with default parameters
14	Ver. 13 with deactivated soot oxidation
15	Ver. 14 with fitted soot model parameters

Table 10. Overview of the incremential changes made to the CFD model.

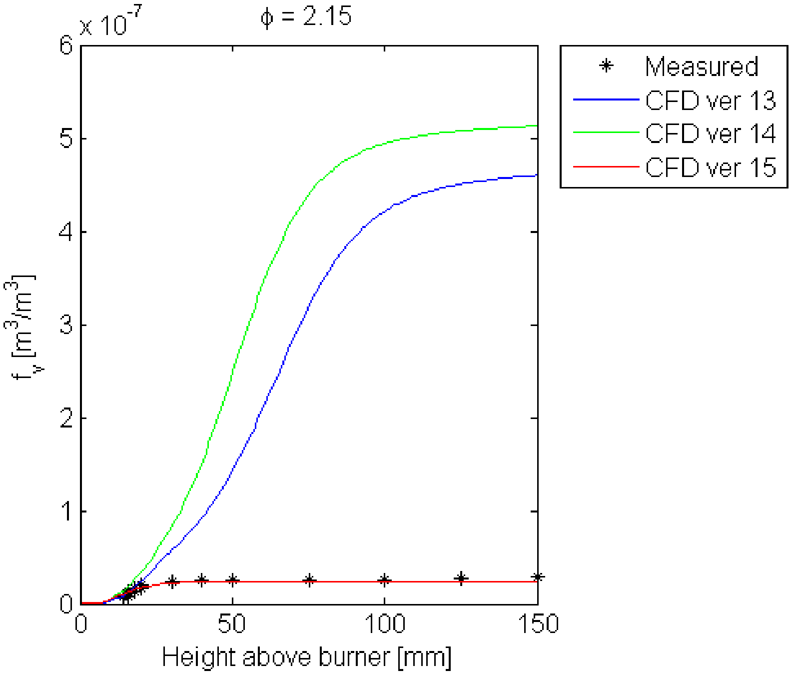

Figure 48. Graph of measured soot volume fractions f_v versus CFD model results. f_v from CFD is taken as the average of $f_{v,x}$ at 10 equidistant locations along the distance L = 75 mm which was optical path used in the measurements (see also Figure 45).

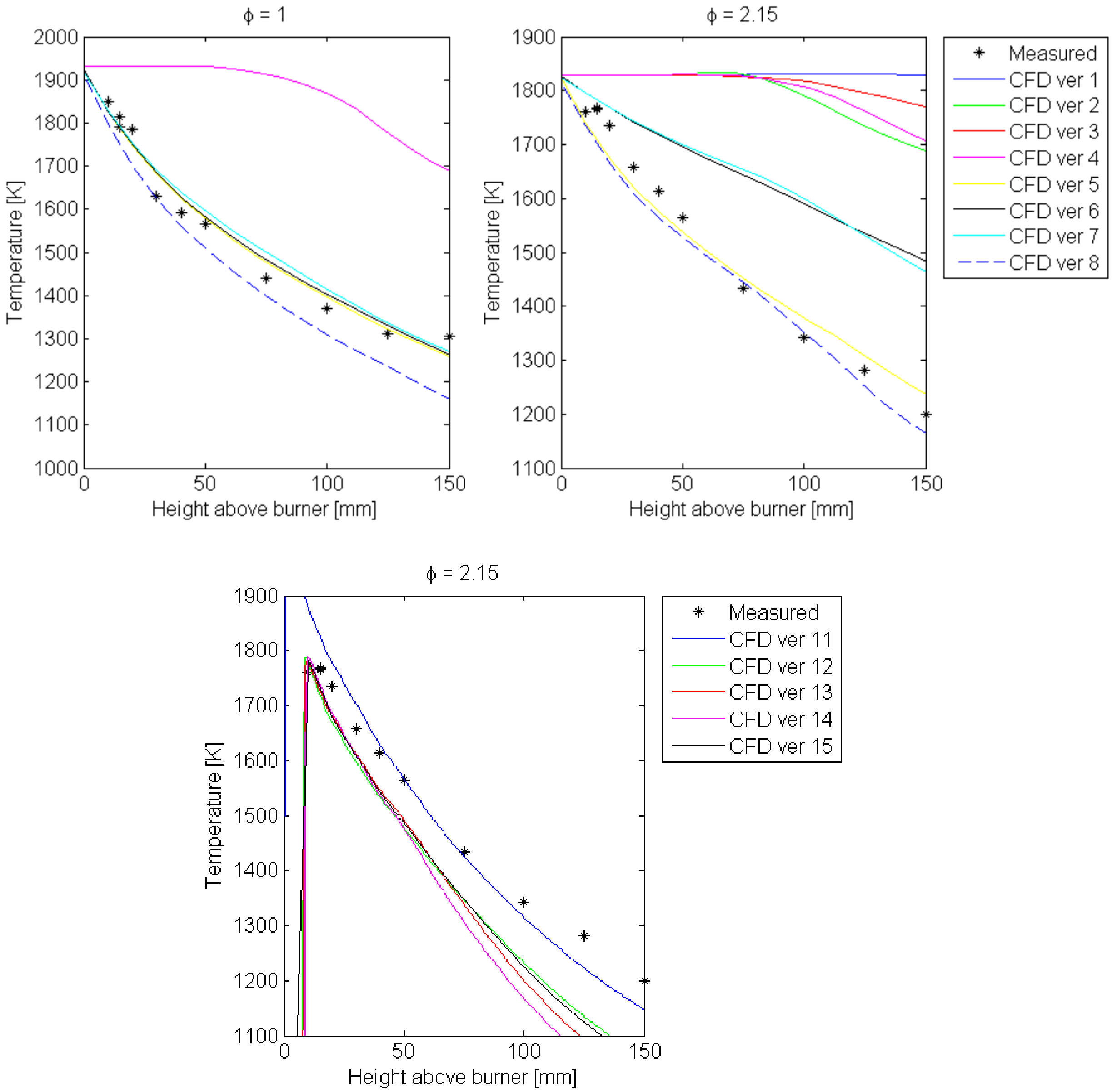

Figure 49. Graphs of the flame core temperature measured in the Helium stabilized flame at different heights. Also shown are predictions from the different CFD models.

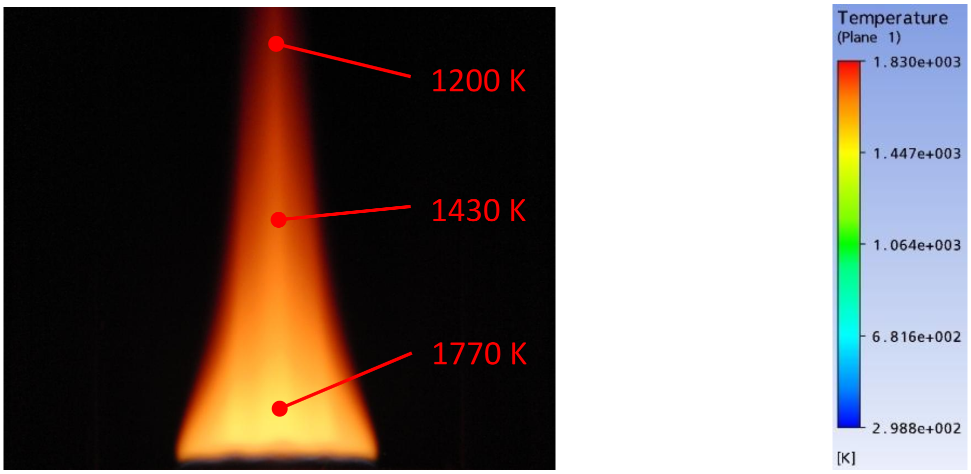

Figure 50. Left: Picture of the helium stabilized flame used for the model validation (Figure 50, Figure 53, Figure 56 and Figure 59 are identical). Right: Color bar showing the temperature color map for the CFD results shown below.

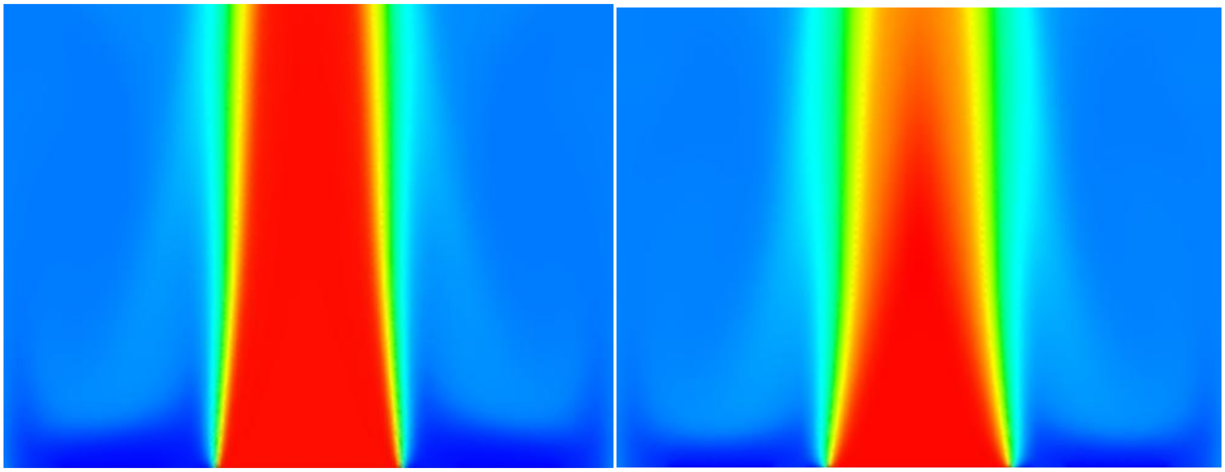

Figure 51. Temperature plots of the stabilized flame calculated with Version 1 (left) and Version 2 (right) models.

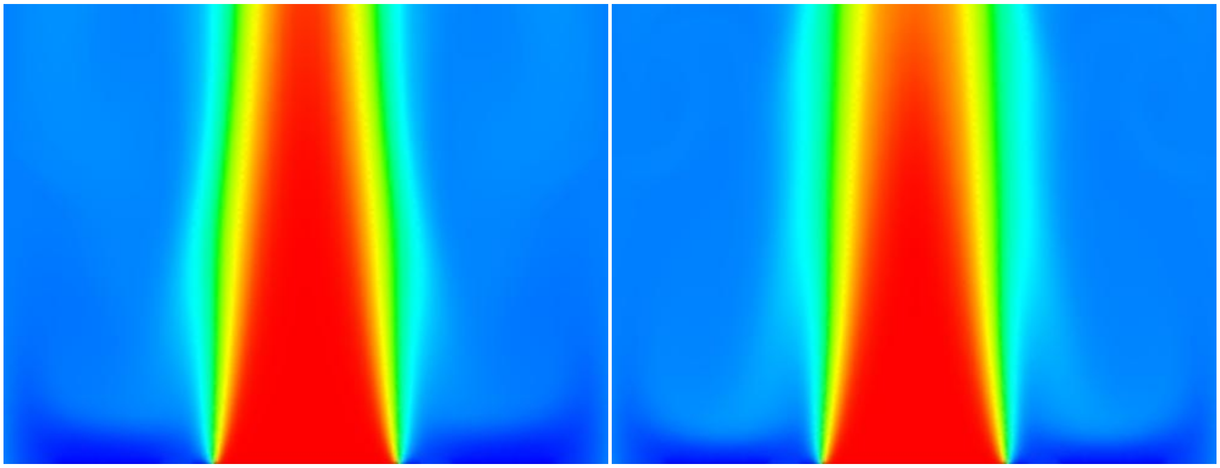

Figure 52. Temperature plots of the stabilized flame calculated with Version 2 (left) and Version 3 (right) models.

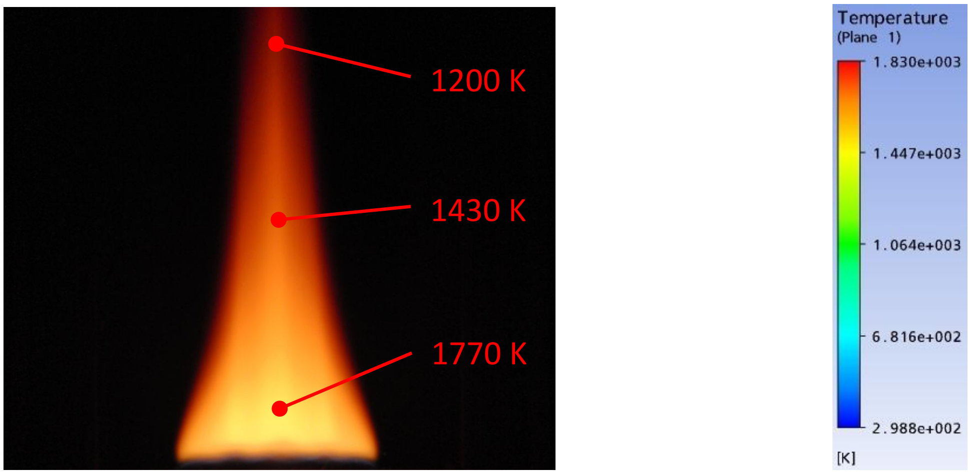

Figure 53. Left: Picture of the helium stabilized flame used for the model validation (Figure 50, Figure 53, Figure 56 and Figure 59 are identical). Right: Color bar showing the temperature color map for the CFD results shown below.

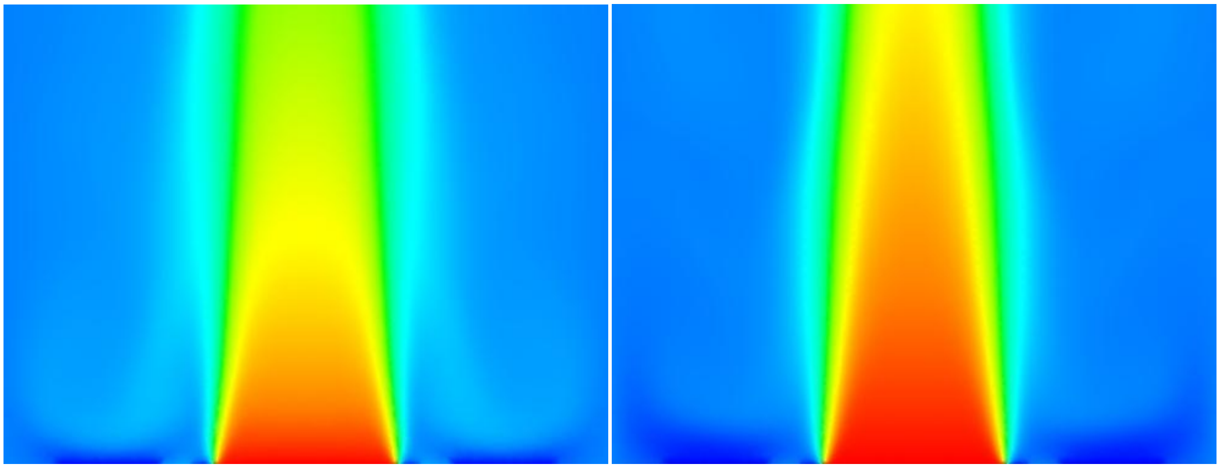

Figure 54. Temperature plots of the stabilized flame calculated with Version 5 (left) and Version 6 (right) models.

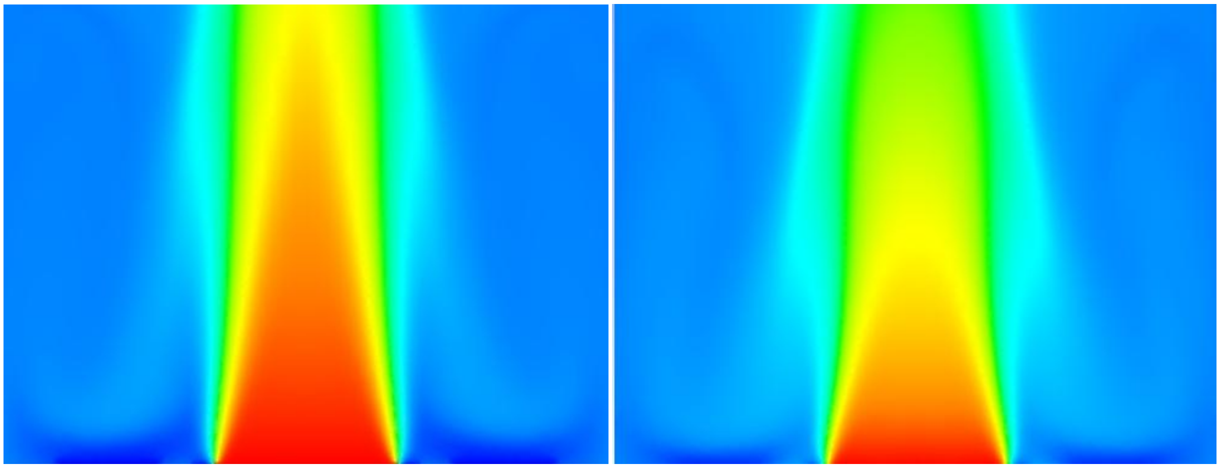

Figure 55. Temperature plots of the stabilized flame calculated with Version 7 (left) and Version 8 (right) models.

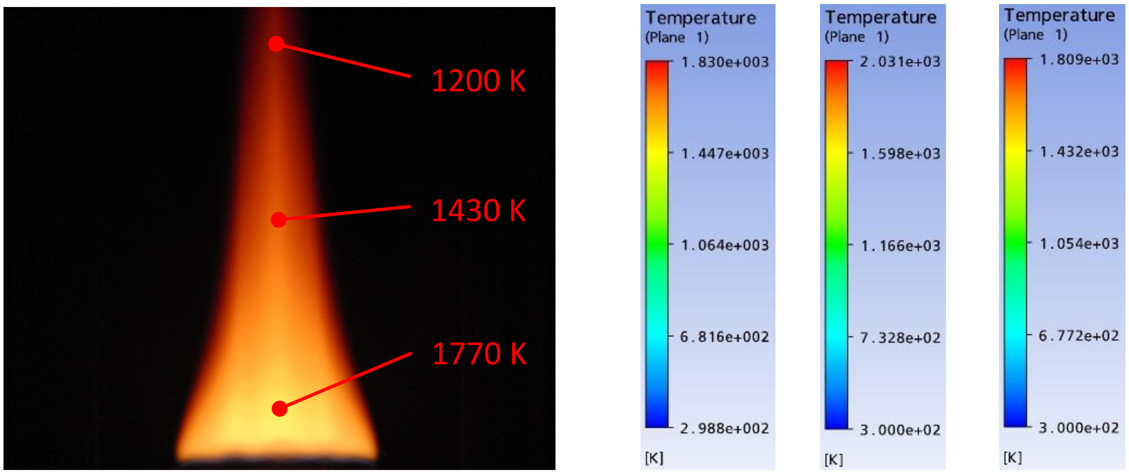

Figure 56. Left: Picture of the helium stabilized flame used for the model validation (Figure 50, Figure 53, Figure 56 and Figure 59 are identical). Right: Color bars showing the temperature color map for the CFD results shown below. Left color bar apply to Version 9 and 10, the middle color to Version 11 and the right color bar to Version 12.

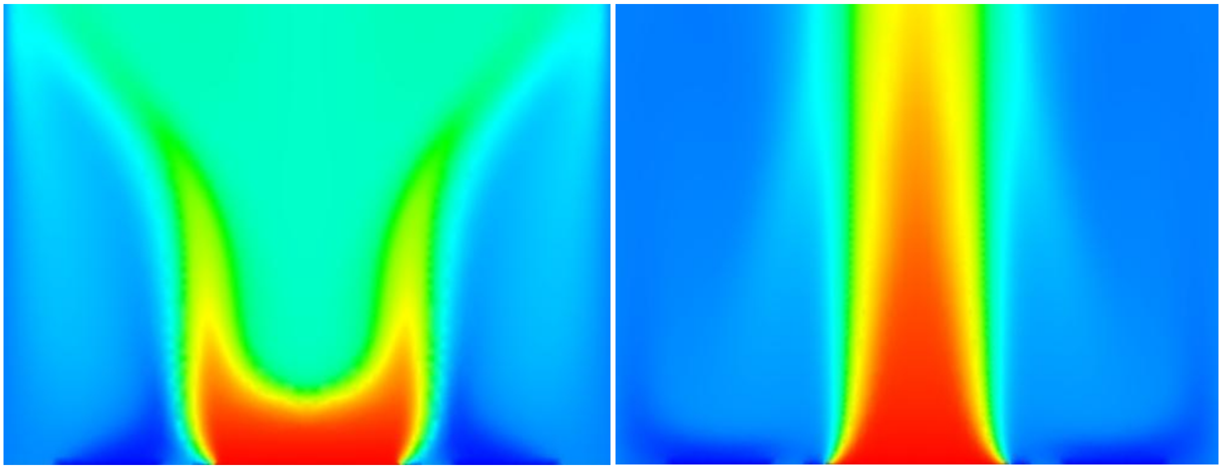

Figure 57. Temperature plots of the stabilized flame calculated with Version 9 (left) and Version 10 (right).

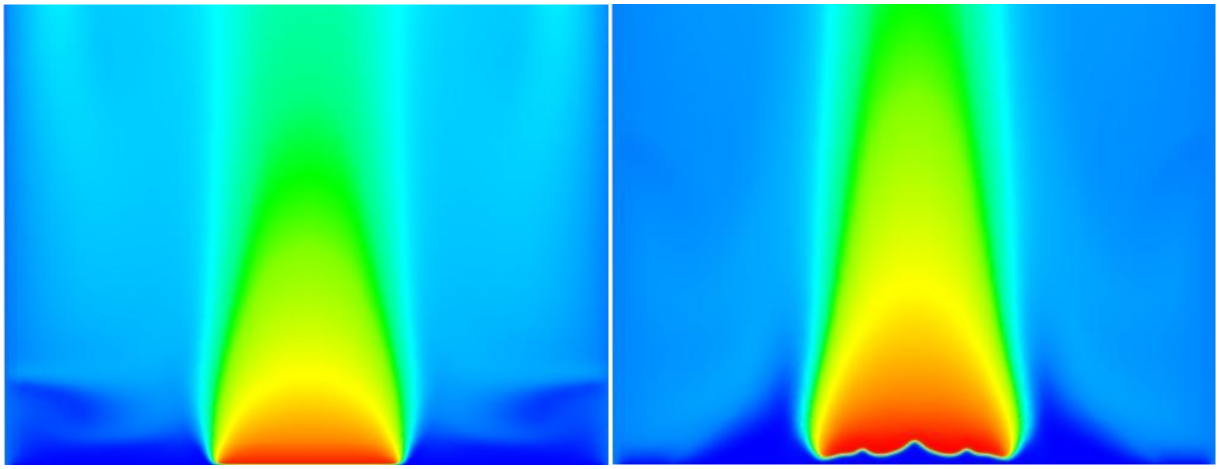

Figure 58. Temperature plots of the stabilized flame calculated with Version 11 (left) and Version 12 (right).

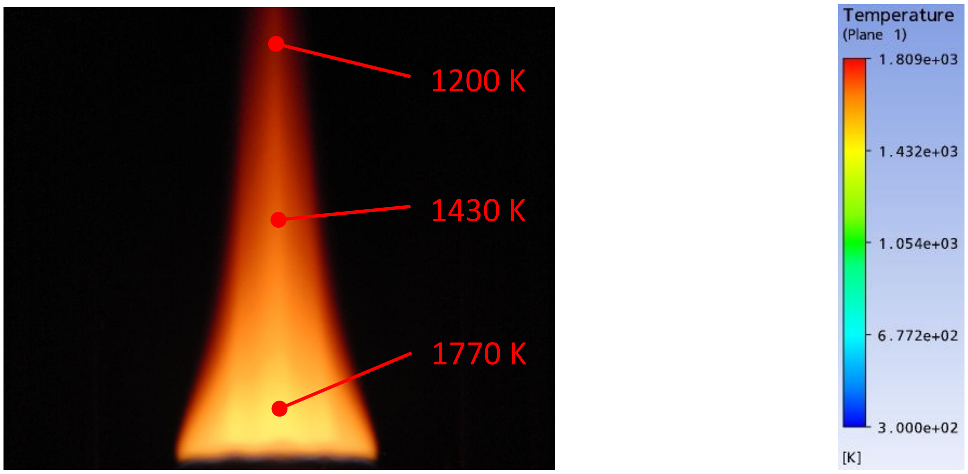

Figure 59. Left: Picture of the helium stabilized flame used for the model validation (Figure 50, Figure 53, Figure 56 and Figure 59 are identical). Right: Color bar showing the temperature color map for the CFD results shown below.

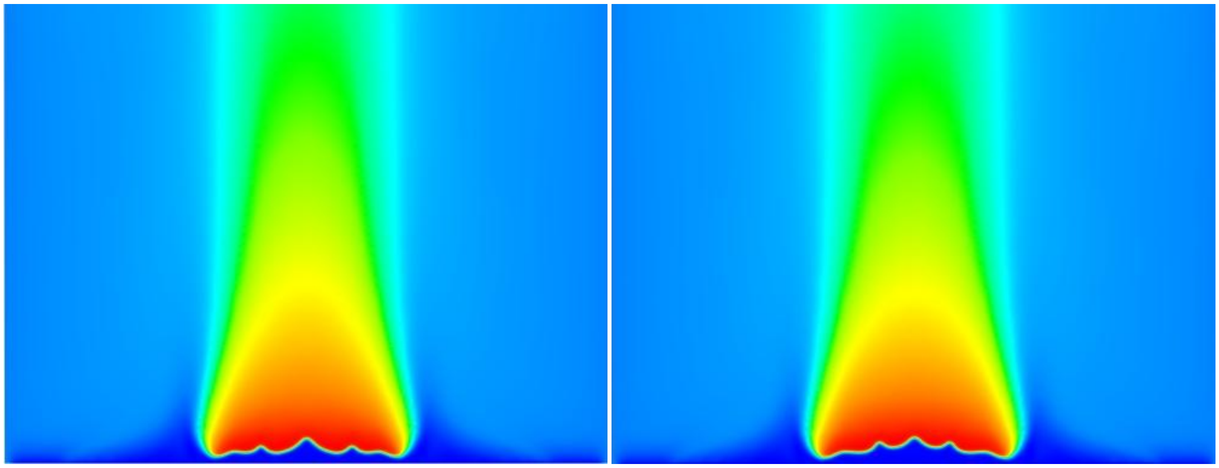

Figure 60. Temperature plots of the stabilized flame calculated with Version 13 (left) and Version 14 (right) models.

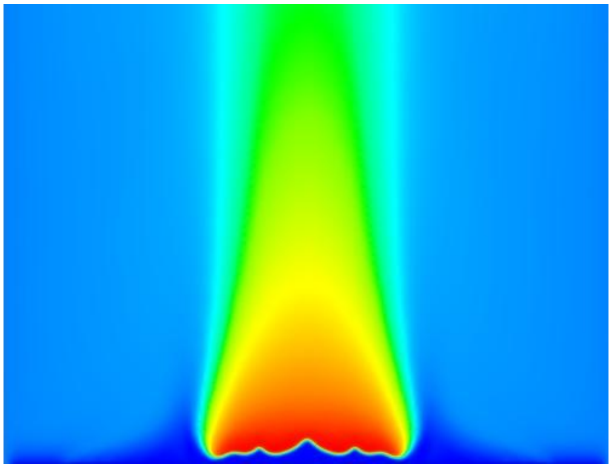

Figure 61. Temperature plot of the stabilized flame calculated with Version 15 model.

Figure 62. High Speed captures of one oscillation period of the instability of the unstabilized target flame (Figure 62, Figure 66, Figure 70, Figure 74 and Figure 78 are identical). The time duration between each frame is 20.5 ms and the oscillation frequency is 6.98 Hz.

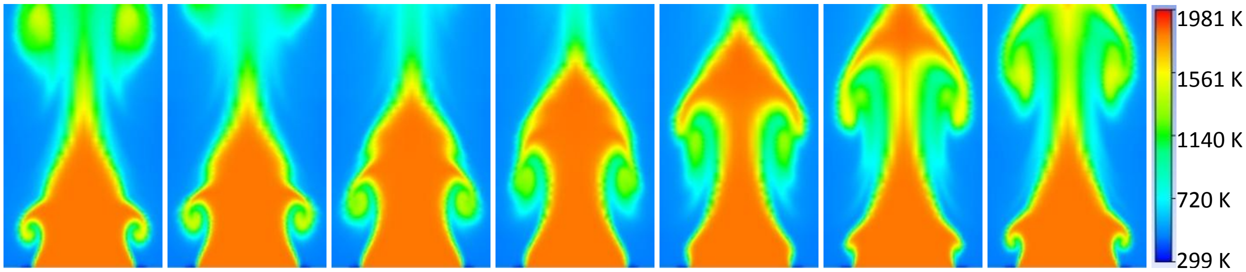

Figure 63. Temperature plots of the unstable flame calculated with Version 1 model. The temperature just above the inlet is 1829 K. The time duration between each frame is 14.6 ms and the oscillation frequency is 9.78 Hz.

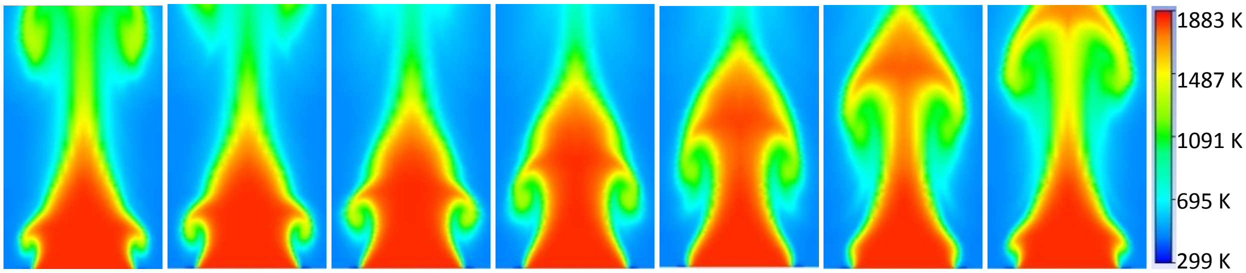

Figure 64. Temperature plots of the unstable flame calculated with Version 2 model. The temperature just above the inlet is 1829 K. The time duration between each frame is 14.6 ms and the oscillation frequency is 9.76 Hz.

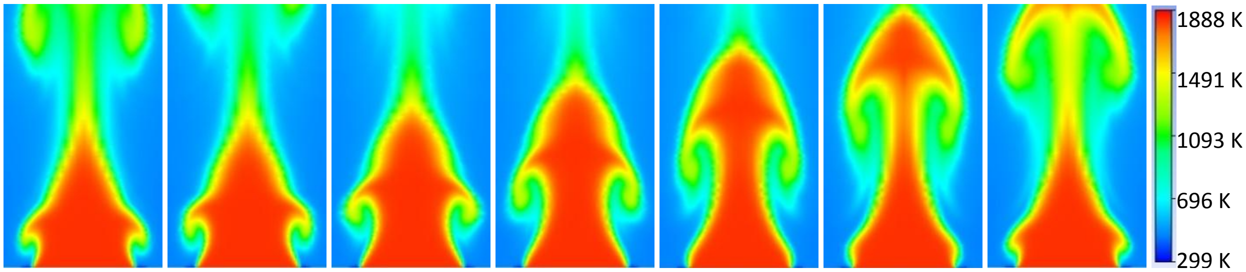

Figure 65. Temperature plots of the unstable flame calculated with Version 3 model. The temperature just above the inlet is 1829 K. The time duration between each frame is 14.7 ms and the oscillation frequency is 9.69 Hz.

Figure 66. High Speed captures of one oscillation period of the instability of the unstabilized target flame (Figure 62, Figure 66, Figure 70, Figure 74 and Figure 78 are identical). The time duration between each frame is 20.5 ms and the oscillation frequency is 6.98 Hz.

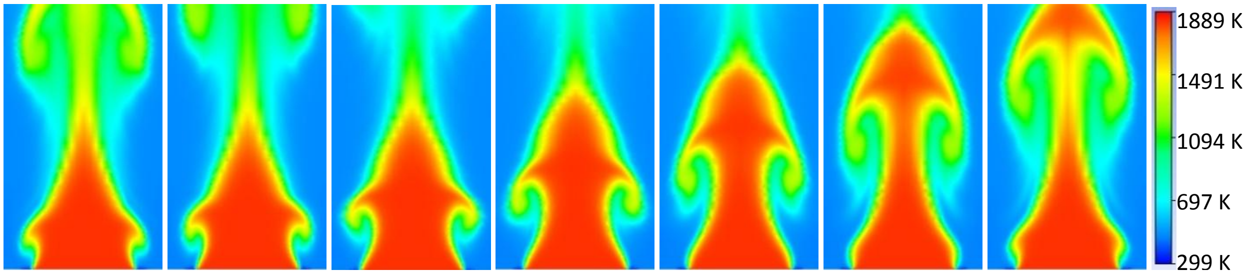

Figure 67. Temperature plots of the unstable flame calculated with Version 4 model. The temperature just above the inlet is 1829 K. The time duration between each frame is 14.8 ms and the oscillation frequency is 9.67 Hz.

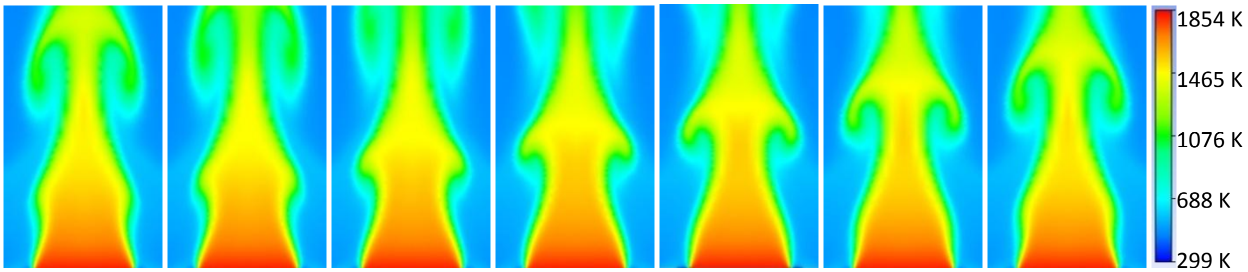

Figure 68. Temperature plots of the unstable flame calculated with Version 5 model. The temperature just above the inlet is 1829 K. The time duration between each frame is 11.9 ms and the oscillation frequency is 12.05 Hz.

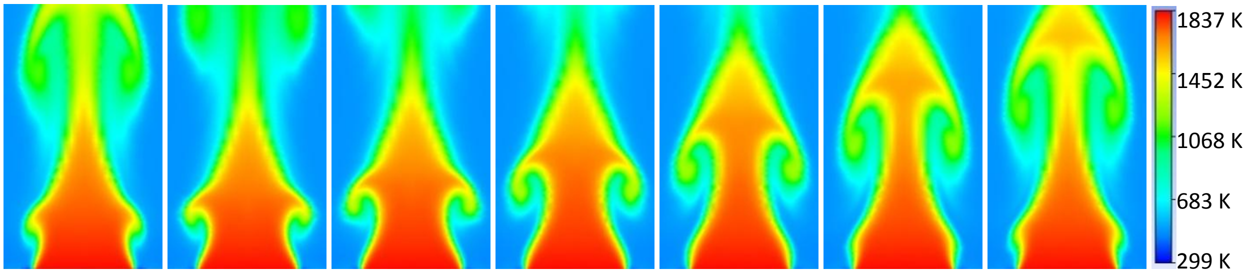

Figure 69. Temperature plots of the unstable flame calculated with Version 6 model. The temperature just above the inlet is 1829 K. The time duration between each frame is 14.0 ms and the oscillation frequency is 10.24 Hz

Figure 70. High Speed captures of one oscillation period of the instability of the unstabilized target flame (Figure 62, Figure 66, Figure 70, Figure 74 and Figure 78 are identical). The time duration between each frame is 20.5 ms and the oscillation frequency is 6.98 Hz.

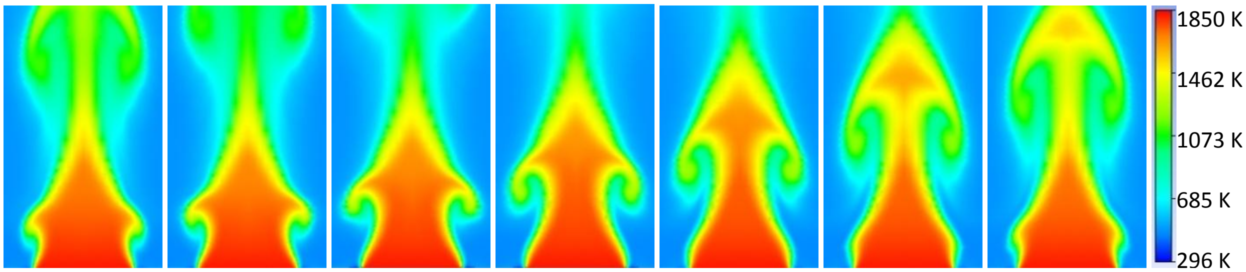

Figure 71. Temperature plots of the unstable flame calculated with Version 7 model. The temperature just above the inlet is 1829 K. The time duration between each frame is 13.9 ms and the oscillation frequency is 10.30 Hz.

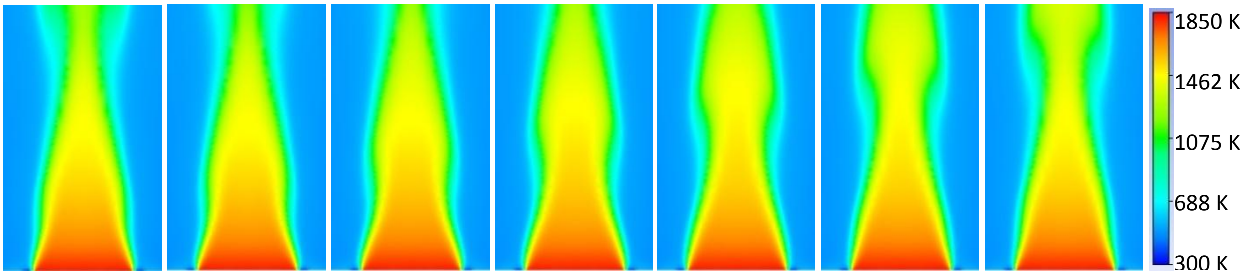

Figure 72. Temperature plots of the unstable flame calculated with Version 8 model. The temperature just above the inlet is 1829 K. The time duration between each frame is 13.9 ms and the oscillation frequency is 11.5147 Hz.

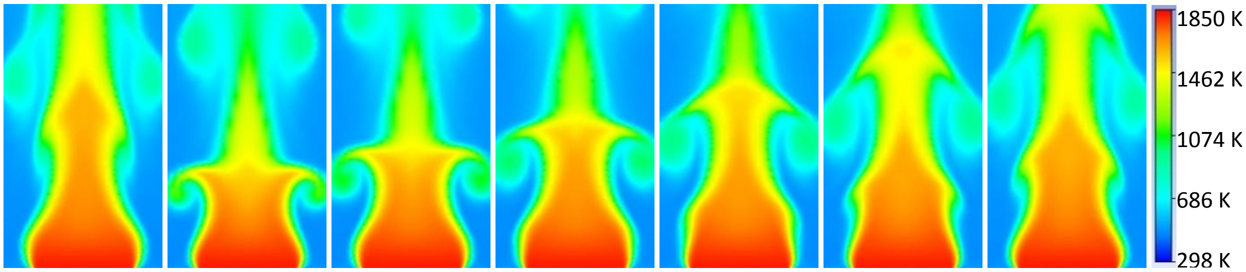

Figure 73. Temperature plots of the unstable flame calculated with Version 9 model. The temperature just above the inlet is 1829 K. The time duration between each frame is 19.1 ms and the oscillation frequency is 7.46 Hz.

Figure 74. High Speed captures of one oscillation period of the instability of the unstabilized target flame (Figure 62, Figure 66, Figure 70, Figure 74 and Figure 78 are identical). The time duration between each frame is 20.5 ms and the oscillation frequency is 6.98 Hz.

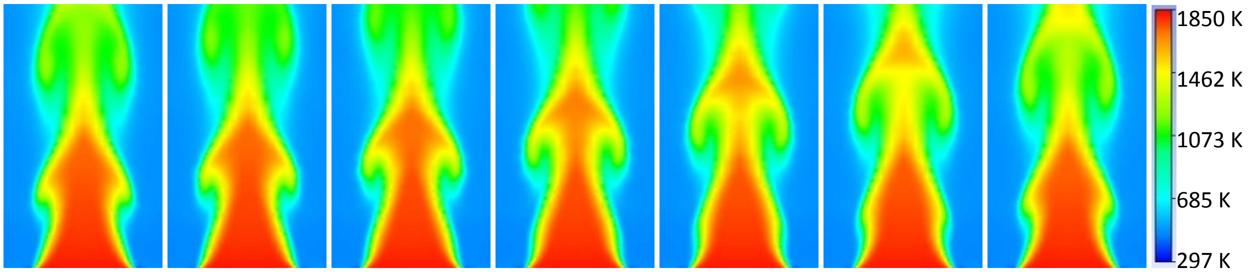

Figure 75. Temperature plots of the unstable flame calculated with Version 10 model. The temperature just above the inlet is 1829 K. The time duration between each frame is 8.4 ms and the oscillation frequency is 17.07 Hz.

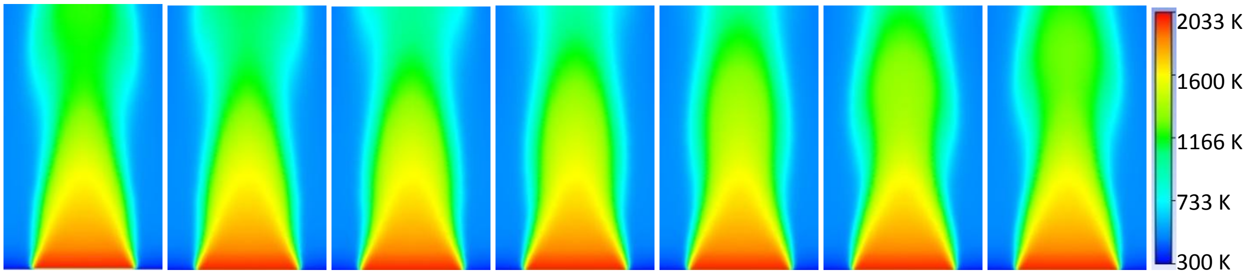

Figure 76. Temperature plots of the unstable flame calculated with Version 11 model. The temperature just above the inlet is 1987 K. The time duration between each frame is 17.1 ms and the oscillation frequency is 8.37 Hz.

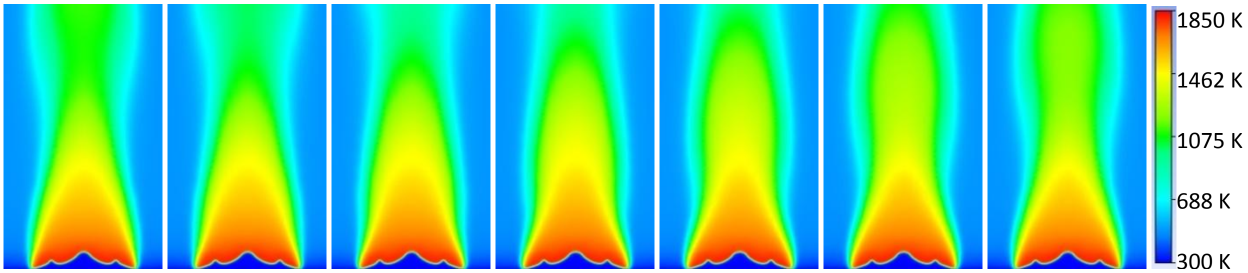

Figure 77. Temperature plots of the unstable flame calculated with Version 12 model. The temperature just above the flame front is 1808 K. The time duration between each frame is 18.9 ms and the oscillation frequency is 7.57 Hz.

Figure 78. High Speed captures of one oscillation period of the instability of the unstabilized target flame (Figure 62, Figure 66, Figure 70, Figure 74 and Figure 78 are identical). The time duration between each frame is 20.5 ms and the oscillation frequency is 6.98 Hz.

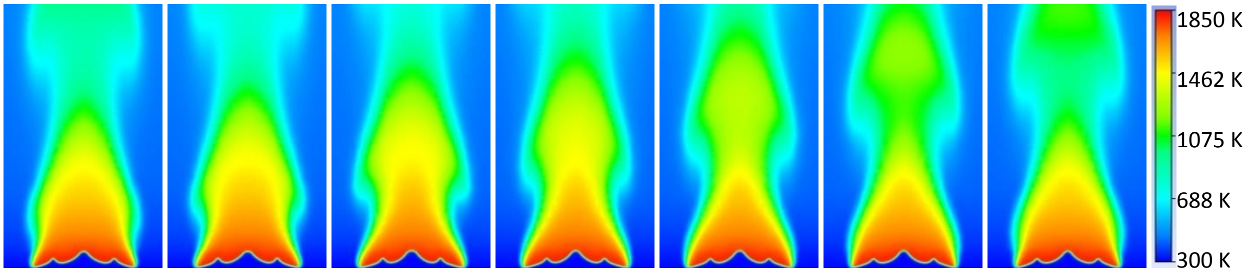

Figure 79. Temperature plots of the unstable flame calculated with Version 15 model. The temperature just above the flame front is 1808 K. The time duration between each frame is 19.0 ms and the oscillation frequency is 7.53 Hz.

Appendix B: Stabilization of a premixed flat flame - Abstract

Stabilization of a premixed flat flame

Anders Ivarsson* and Jesper Schramm

Department of Mechanical Engineering, Technical University of Denmark, Lyngby, Denmark

Full length paper submitted to Combustion & Flames in October 2008

Abstract

The post flame instability, also known as flame flicker, of a flat premixed ethylene/air flame has been under experimental investigation. A nonintrusive method has been developed to stabilize premixed flat flames, which we call helium stabilization. The method is to ensure almost equal gas densities inside and outside the flame by diluting the surrounding gas with helium. This newly stabilized flame offers some features, which are important in combustion research. The flame is very uniform and may be highly lifted, thus perfectly suited for optical line by sight diagnostics in both pre and post combustion regions. The work also includes some preliminary studies of radiant emissions from helium stabilized ethylene/air and methane/oxygen flames. It is demonstrated that soot nano particles below the sooting threshold actually are weakly luminous.

*Corresponding author:
Address: Nils Koppels Alle 403, 1th floor, 2800, Lyngby, Denmark
Telephone: +45 45 25 42 30
Fax: +45 45 88 43 25
E-mail: ai@mek.dtu.dk

Appendix C: IR thermometry of premixed flat flames - Abstract

IR thermometry of premixed flat flames

Anders Ivarsson* Sønnik Clausen** and Jesper Schramm

Department of Mechanical Engineering, Technical University of Denmark, Lyngby, Denmark
** Risø National Laboratory for Sustainable Energy, Technical University of Denmark, Roskilde, Denmark

Full length paper submitted to Combustion & Flames in January 2009

Abstract

A thermometry method based on IR emission and absorption by CO_2 between 2100 and 2400 cm^{-1} was developed specifically for pre-mixed flat flames. Detection was performed with a commercial FT-IR spectrometer.

An investigation of the method's precision and accuracy was performed separately. The investigation shows that an important strength of the method is its reliability with regard to variations in the experimental setup. Even with non-optimized installation and operation of the method, the average line of sight temperature determination to a precision of +/- 2 % may be achieved. With a thorough installation and operation the method detects the temperature of the flame core within +/- 1 %, in spite of the line of sight principle.

Temperature measurements from the literature performed with different thermometry techniques were reproduced and compared. Some of the methods from literature were valid only for a limited range of flame conditions. Thus the consistency of the most established flame thermometry techniques was evaluated, with the IR emission absorption method used as link.

*Corresponding author:
Address: Nils Koppels Alle 403, 1st floor, 2800, Lyngby, Denmark
Telephone: +45 45 25 42 30
Fax: +45 45 88 43 25
E-mail: ai@mek.dtu.dk